EXPERIMENTAL STUDY OF HOLLOW FRP SECTIONS UNDER BENDING FOR USE AS BRIDGE DECKING

by

Eric Tynski

Submitted in partial fulfilment of the requirements
for the degree of Master of Applied Science

at

Dalhousie University
Halifax, Nova Scotia
December 2020

TABLE OF CONTENTS

LIST OF TABLES

LIST OF FIGURES

ABSTRACT

In this thesis, the behaviour of square hollow structural sections made of glass fiber reinforced polymers (GFRP) under four-point bending both independently and in composite with concrete was investigated. The end goal of the research was to determine if the systems tested could be viable for use as bridge decking. Hollow specimens of three different lengths, 1 m, 2 m, and 3 m were originally tested and deemed too flexible to be used in a bridge decking system. The main portion of testing was conducted on 18 FRP specimens with concrete slabs of different thicknesses cast overtop. Three slab thicknesses were used: 35 mm, 55 mm, and 75 mm to simulate three different cases of neutral axis location. Half of the slabs were bonded to the FRP by first applying a layer of epoxy paste to the top face of the FRP and covering it with small aggregate before casting the concrete. The other half had bolts drilled into the specimens at 100 mm intervals along the specimen before concrete was poured. It was found that the addition of concrete decreased overall strength, as it governed failure over the FRP in all slab specimens tested. The concrete gave an increase in stiffness between 62 and 78% for the epoxy and aggregate bonded specimens, and an increase between 54 and 79% for bolt bonded specimens. Two analytical models were created to predict the load-deflection behaviour of the specimens. A linear-elastic model was developed and successfully predicted hollow specimen behaviour. A non-linear model was used to predict behaviour of slab specimens assuming full composite action. It could predict a range of loads and deflections the test data fell into, as specimens acted only partly in composite. Modelling partial composite action was not in the scope of this project. Overall, the epoxy and aggregate bonded specimens are the most promising for use as bridge decking, but more research is needed to confirm this.

LIST OF ABBREVIATIONS AND SYMBOLS USED

Abbreviations

ASCE	American Society of Civil Engineers
ASTM	American Society for Testing and Materials
BGM	Brooming Along the Gauge Length
CFRP	Carbon Fiber Reinforced Polymer
CIRC	Canada's Information Resource Centre
Co.	Company
CPF	Composite Percentage Factor
CSA	Canadians Standards Association
CV	Coefficient of Variation
CW	Crosswise
FEM	Finite Element Methods
FRP	Fiber Reinforced Polymer
FS	Filled Section
GFRP	Glass fiber reinforced polymer
HS	Hollow Section
ILW	Ignition Weight Loss
LP	Lateral Potentiometer
Ltd.	Limited
SG	Strain Gauge
SIP	Stay-in-place
SSA	Slab Section – Epoxy and Aggregate Bond
SSB	Slab Section – Bolted Bond
SSC	Slab Section – Commercially Available Concrete Adhesive Bond

Symbols

A	Cross-sectional Area
a	Distance from Support to Loading Point
A_w	Cross-sectional Area of the Web
B	Base Width
b	Cross-Sectional Width
b_{TR}	Transformed Cross-Sectional Width
c	Neutral Axis Depth
d	Distance between Strain Gauges
D	Flexural Rigidity
E	Young's Modulus of Elasticity
f_c	Concrete Stress
f'_c	Concrete Compressive Strength
F_{sbs}	Short Beam Strength
G	Shear Modulus
h	Cross-Sectional Height
H	Total Specimen Height
I	Moment of Inertia
I_{TR}	Transformed Moment of Inertia
K	Beam Stiffness
k	Shear Coefficient
L	Length
M	Bending Moment
n	Transformation Factor
P	Applied Load
P_n	Nominal Strength
P_u	Ultimate Load due to Punching Shear
Q	First Moment of Area
t	Wall Thickness

t_{TR}	Transformed Wall Thickness
V	Shear Force
W	Weight
x	Shear Span
Δ	Deflection
ε	Strain
ε_c	Concrete Strain
ε_f	FRP Strain
σ	Flexural Stress
ΣF	Sum of Forces
τ	Shear Stress
τ_{BOND}	Bond Strength
ψ	Curvature
ω_{eff}	Effective Reinforcement Index

ACKNOWLEDGEMENT

The author acknowledges the financial support of Dalhousie University throughout this research. The author would like to thank the lab technicians Brian Kennedy, Jesse Keane, and especially Jordan Maerz, without whom this project would not have been possible. Support from Dr. Pedram Sadeghian and the students in the CRSCI lab group is greatly appreciated.

CHAPTER 1 INTRODUCTION

1.1 MOTIVATION

As of 2019, 35% of highway bridges in Canada were at least 50 years old. Around 10% of publicly owned highway bridges were assessed to be in poor condition. The amount of bridges in poor condition Canada-wide has increased from 3% to 11% since 2016 (CIRC 2019). In the United States, as of 2017, almost 40% of bridges are at least 50 years old and 9% were deemed structurally deficient (ASCE 2017). Further, as a comparison, the World Economic Forum's Global Competitiveness Report ranked the United States 17th in the world for quality of road infrastructure, Canada ranked 30th (Schwab 2019). Suffice to say that Canada has a problem with aging and deteriorating bridges, one that will only be worsened by the effects of more severe extreme weather events brought on by climate change. In a 2019 survey, 80% of participating municipalities in Ontario reported that climate change and related events have had an impact on road and bridge infrastructure in the past decade, 9% classified the impact as extensive (Gunson and Murphy 2019).

As a result of the aging and deteriorating bridge infrastructure it is likely that there will be an increase in both new construction and rehabilitation projects of that nature in Canada over the coming decades. With climate change considered it is also likely that these projects will be trending toward using more resilient and sustainable building methods and materials, which must be done while optimizing life cycle costs. It has been estimated that upwards of one half of costs associated with bridge rehabilitation projects are allotted to the decking (Lounis 2007). It would seem beneficial to construct a durable bridge deck that could reduce the amount of maintenance required, lowering total life cycle costs.

Bridge decking has traditionally been made from materials such as concrete or wood. While structurally adequate, these materials can face degradation over time depending on traffic volume and environmental conditions. One particularly harsh condition for steel reinforced concrete is corrosion caused by de-icing salts. This presents a problem, especially in Canada, as de-icing salts can be required for up to six months at a time in some areas. The corrosion and subsequent degradation of reinforced slabs comes with increased need for service and replacement, which can become very expensive. An alternative that provides more durability and subsequently requires less maintenance is to use fiber reinforced polymer (FRP) composites in bridge decking.

FRP composites are becoming a more commonly used alternative to steel and concrete in construction applications. FRPs are corrosion resistant and have a high strength-to-weight ratio, making for an ideal alternative to use in bridge decking. (Nelson et al. 2014).

1.2 OBJECTIVES

Given the need for improved corrosion resistance in bridge decking, the main goal of this research is to assess the viability of a bridge decking system constructed from commercially available FRP components, in this case, square-hollow tubes.

Based on the project goal, the objectives of this research are:

- To assess the structural behaviour of a pultruded hollow FRP section subjected to bending.
- To evaluate the performance of components of a conceptual bridge decking system made of pultruded hollow FRP sections independently and in composite with concrete.

- To create an analytical model that can predict the behaviour of the bridge decking system.

1.3 RESEARCH SCOPE

To achieve the objectives outlined above, structural FRP sections were tested under four-point bending, having varying lengths and load spacings. Once bending behaviour was characterized, tests were done to find the most effective way to use the structural sections as a bridge decking component. Three main configurations were tested: hollow beams, beams filled with concrete, and beams with a concrete slab cast overtop using various bonding mechanisms on the FRP-concrete interface. The systems with the highest stiffness were then tested rigorously and results were used to verify analytical models created to predict the bending response of the decking system.

1.4 THESIS LAYOUT

The general layout of this thesis consists of an introduction to how FRP has been implemented as a bridge decking material in a literature review, an in-depth explanation of the experimental program, a discussion of the results obtained, an overview of the analytical modelling completed, ending with conclusions and recommendations for future research. The literature review, Chapter 2, will investigate reasons why FRP is an ideal alternative to traditional reinforced concrete for bridge decking, and ways it has been implemented previously. There will be a focus on how FRP has been used in composite with other structural materials such as concrete. Chapter 3 explains the experimental program for the research undertaken, with attention given to how the FRP material was studied and characterized. Included in this chapter are test matrices, as well as explanations

of specimen fabrication, instrumentation, and test setup. It will conclude with a presentation and discussion of the bending test results. In Chapter 4, the analytical model created to predict the bending response of the bridge decking system will be discussed in detail. Finally, conclusions will be presented along with recommendations for future research in Chapter 5.

CHAPTER 2 LITERATURE REVIEW – FIBER REINFORCED POLYMERS AND ITS USE IN BRIDGE DECKING

2.1 FIBER REINFORCED POLYMERS – AN OVERVIEW

Fiber reinforced polymers (FRPs) are heterogeneous composite materials made up of two basic parts: reinforcing fibers and a polymer based resin matrix (Bank 2006a), a basic example of an FRP cross-section is shown in Figure 2-1. In general, the fibers give the material its strength while the matrix that encases them gives the FRP its shape. For structural purposes, the most common fiber types used are glass and carbon, although both natural (flax, hemp) and synthetic fibers (aramid, polyethylene) have been tested as well (Benmokrane et al. 2007). Matrices are made from polymeric resins, the most common being epoxy, polyester, and vinylester (Bank 2006a). Each material can be broken down into more subcategories (such as E-glass fibers, S-glass fibers, etc.) with slightly different mechanical properties, but all FRPs act similarly. They behave very elastically and generally outperform traditional building materials like steel and concrete in metrics such as corrosion resistance, wear resistance, and strength-to-weight ratio (Bakis et al. 2002). FRPs can also be chemically altered to be more beneficial depending on use, such as flame retardance, puncture resistance, and anti-biofouling properties (Keller 2002; Rajak et al. 2019).

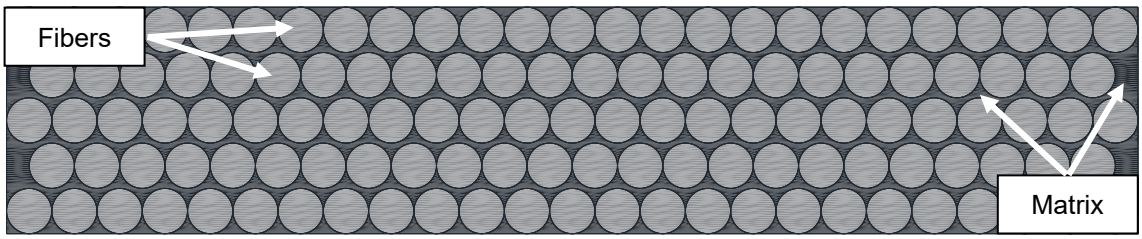

Figure 2-1 Cross-Section of typical FRP composite

There are a variety of ways to manufacture FRPs. The most common for structural engineering purposes is pultrusion (Bakis et al. 2002). In the pultrusion process, dry fibers are pulled from a roll along an assembly line, the finished product is a completed FRP composite. The fibers are pre-woven to create the desired orientation for the composite being made (unidirectional, biaxially stitched, etc.). The process begins when the dry fibers are pulled through a resin bath, becoming saturated and forming a viscous liquid composite. From there, the shapeless composite is guided through a, heated die that forms it into a desired shape and allows it to cure. After exiting the die, the now solid composite is pulled to the end of the assembly line where it can be cut into a specified length (Bank 2006a). A picture showing steps of the process can be seen in Figure 2-2.

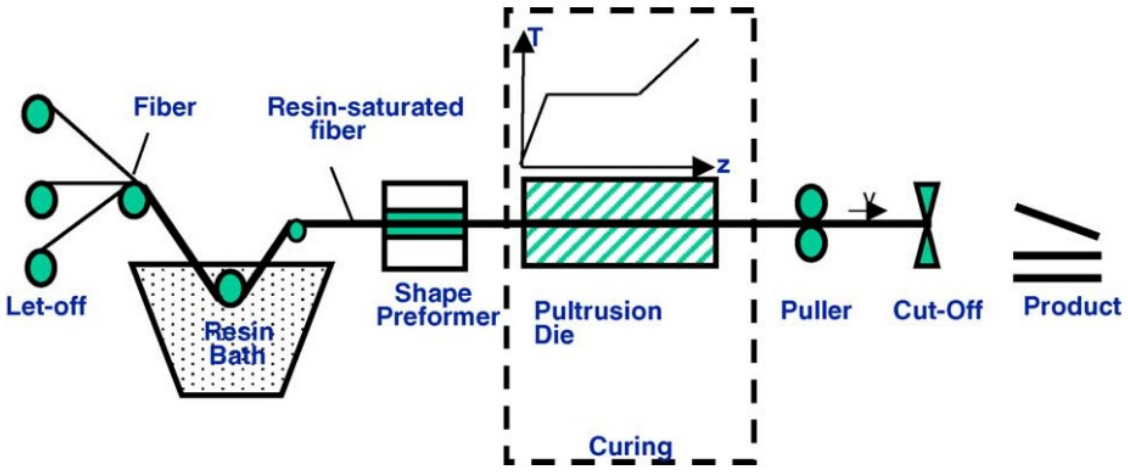

Figure 2-2 Schematic of the pultrusion process (Acquah et al. 2006)

Another FRP manufacturing method used for some structural components is hand layup. Rather than being automated, hand layup is a manual process in which layers of fibers are placed into a form and are impregnated with a liquid resin. The resin then cures creating a solid FRP composite. This method is often used for flatter structural components, an example being the face sheets of sandwich panels. Advantages to hand-layup over

pultrusion include less equipment being needed for the process and having no heat required to cure the product. A disadvantage is that because of the manual component, hand-layup products cannot be produced as quickly or efficiently as pultruded products (Rajak et al. 2019).

Pultruded FRP composites have many characteristics and properties that make them beneficial for structural purposes. As mentioned, they have a high strength to weight ratio compared to traditional materials (Bakis et al. 2002; Bank 2006a). FRPs are overall quite durable, having good resistance to corrosion and wear. These properties are useful under adverse conditions such as freeze-thaw cycles, harsh weather, and those encountered on offshore structures (Bank 2006a; Boles et al. 2015; Daniel and Ishai 2006). FRP composites in general have linear elastic behaviour at lower strains, which makes them resistant to cyclic loading and fatigue conditions, like those in highway structures (Bank 2006a).

Although pultruded FRP composites have many advantageous qualities, there are also limitations to be considered. Due to the linear elastic behaviour of the material, failure tends to be brittle and sudden, often no signs of progressive failure can be noticed visually. The brittle failure usually also takes away any structural integrity the FRP composite once had, which is less desirable than a ductile failure like that of structural steel (Daniel and Ishai 2006; Keller 2002). In GFRP, failure loads have shown to decrease under prolonged exposure to adverse conditions. While some studies have shown that cyclic loading to have little effect on structural FRP (Cheng and Karbhari 2006; Dieter 2002), prolonged exposure to this type of loading can cause strength degradation, especially in GFRP (Andersons and Korsgaard 1999; Benmokrane et al. 2007; Wu et al. 2014). GFRP composites are also susceptible to creep rupture which is brought on by sustained loading, but also affected by

temperature and exposure to alkaline environments (Benmokrane et al. 2007). Although in general FRP composites are resistant to corrosion, persistent exposure to both acidic and alkaline conditions haven been shown to be detrimental to GFRP (Benmokrane et al. 2007). Concerning temperature, when FRP is subjected to high heat, its structural properties can break down and in some cases the composite itself will even ignite. Many resins used to make up the matrix component of FRP will melt at 150 °C and can combust or evaporate at 400 °C (Lau et al. 2016). The limitations above have led to service factors on FRP materials in Canadian design standards, with GFRP having the most extreme service reduction compared to other synthetic fibers (like carbon), in some cases being limited to 25% of its strength capacity (Benmokrane et al. 2007; CSA Group 2019).

Another major factor as to why FRP composites are not more commonly used is the cost compared to traditional materials. The initial material cost of FRP can be more than double that of structural steel or reinforced concrete and if additives are used to give the FRP additional beneficial properties (like fire resistance) the cost can be further increased (Bakis et al. 2002; Bank 2006b; Ehlen 1999; Nelson et al. 2014). Some costs throughout the life cycle of structural FRP composites can be less than that of traditional materials because of its composition and weight. Notably, quicker installation times and the possibility of less maintenance being needed can lead to reduced labour costs compared to traditional materials. This often does not offset the initial costs enough for FRP to be used over concrete and steel as a structural material, however (Bank 2006a)

2.2 FRP AS BRIDGE DECKING

FRPs started to gain popularity for use in bridge construction in the 1980s as a durable, corrosion resistant material for highway infrastructure. Pedestrian bridges were the first

type of bridge to start using FRP as a primary material. The high strength-to-weight ratio compared to steel and concrete paired with the fact that FRP bridges require little maintenance made it an ideal material for short-span bridges that could be erected quickly (Keller 2002). As of 2005 there were over 300 all-FRP pedestrian bridges in the United States (Bank 2006b). In the late 1980s, research on the use of FRP composites for highway bridge decking started to pick up, with all-FRP decks being explored at first (Bank 2006b). While all-FRP decking is still common, other decking systems have been researched and implemented as well. Examples include sandwich panel decks with foam cores, using FRP stay-in-place (SIP) formwork as decking, and hybrid decks comprised of FRP and materials like wood or steel (Nelson et al. 2014). FRP bridges decking has been used in both new construction and rehabilitation projects (Bank 2006b; Nelson et al. 2014), an example of the latter can be seen in Figure 2-3.

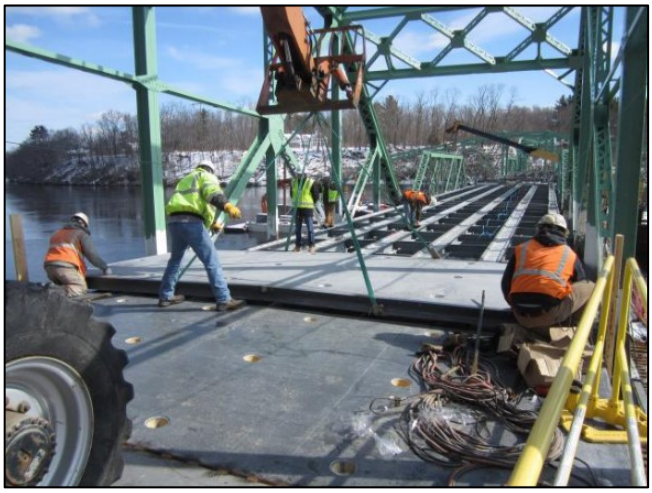

Figure 2-3 Picture of all-FRP panels being installed for a re-decking project (Loff 2015)

FRP is generally more durable than these traditional materials in areas where adverse weather conditions are more common (like in winter conditions where de-icing salts are necessary). This durability along with its corrosion resistant properties can allow for FRP

decks to need less maintenance than traditional reinforced concrete decking, which can lead to savings on labour and maintenance costs (Bakis et al. 2002; Bank 2006b; Nelson et al. 2014), although initial costs of FRP decks are still higher than that of reinforced concrete (Bank 2006a). FRP also has a low material weight which provides many benefits of its own. It is generally easier to transport and have its components constructed on-site compared to traditional materials. It can also reduce the overall dead load of a structure, helpful for rehabilitation projects and moveable bridges (Bakis et al. 2002; Composite Advantage 2008; Keller 2002).

2.2.1 All-FRP Bridge Decking

All-FRP bridge deck components (profiles) are typically structured like sandwich panels, having vertical components patterned between two face sheets, rather than a core material. FRP decks are usually pultruded, allowing them to come in various arrangements that can take the form of basically any geometric shape. Some are manufactured as one solid piece while others are built up modularly and bonded with adhesive (Bakis et al. 2002; Bank 2006b; Keller 2002; Williams et al. 2001). All-FRP bridge decks can be used in the same applications as a typical slab-on-girder deck would, with installation being similar: sections are transported to the site, placed on girders or other supports, and bonded or grouted together. Highway bridge decks are generally coated with a wearing surface for added durability (Bank 2006b). An image of a typical FRP deck profile is shown in Figure 2-4.

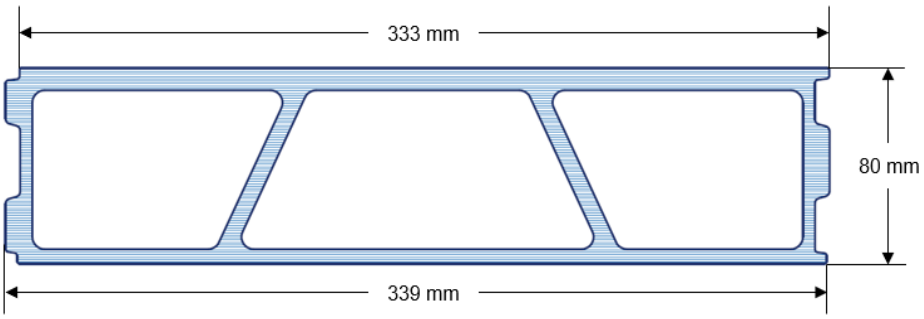

Figure 2-4 Cross-section of an FRP bridge deck profile (Fiberline 2017)

2.2.1.1 Beneficial FRP Properties for Decking

One advantage that FRP decking has over traditional materials is its variability. There are many different FRP properties that can be altered during manufacturing to enhance its performance in certain applications. A comprehensive study was done by Ascione et al. (2016) outlining FRP properties that improved performance as a structural material (Ascione et al. 2016).

One of the most crucial features to FRP bridge decking is having good durability. Bridge decks are subjected to many adverse conditions including cyclic loading (leading to fatigue) and environmental factors such as exposure to acidic or alkaline substances. When making an FRP composite, choosing materials can balance durability and strength is important (Ascione et al. 2016; Bank 2006b). During the manufacturing process, changes to the amount of air entrapped in the matrix (void content) and curing time can lead to a longer-lasting material. As mentioned above, resin additives can be used to design an FRP composite resistant to detrimental conditions such as fire, humidity, and biofouling (Ascione et al. 2016; Rajak et al. 2019). Fiber type is also important as some fiber types like glass or carbon are more stable with temperature changes than other synthetic fibers, like aramid. Even changing fiber colour can be considered for temperature control. Having

the advantage of optimizing these properties is a key reason why FRP is a useful material for structural purposes and especially bridge decking (Ascione et al. 2016).

Another variable feature FRP profiles have is their geometry. Not unlike steel, having a variety of profile shapes to choose from can give FRP an advantage under different loading conditions. Bridge decking must resist bending and shear forces, and there are cases for which FRP profiles may be subjected to axial or torsional forces as well. Like steel, profile thickness can have an impact on bending and shear resistance. Increased flange thickness helps to resist bending and shear forces, while increased web thickness can also improve transverse shear resistance (Ascione et al. 2016). The main factor impacting transverse shear resistance, however, is profile geometry (Yanes-Armas et al. 2015). Depending on loading conditions, varying the profile geometry may not only help to satisfy ultimate limit states but optimize them as well. Being able to design the cross-sectional geometry of an FRP profile based on loading conditions aids in creating more structurally efficient building materials and in turn can allow for cost savings (Ascione et al. 2016; Ehlen 1999).

FRP properties and geometry can also be varied to help with serviceability issues. Resin additives (specifically graphene) has been shown to help decrease vibration levels in FRP decking panels (Rajak et al. 2019). As well, geometry and FRP material properties can have an impact on creep resistance in FRP panels (Ascione et al. 2012).

2.2.1.2 Experimental Testing of All-FRP Decking

With so much variability in what shape FRP decks can take, experimental tests may seem subjective. Looking at trends in the results of experimental testing can show how useful FRP profiles and built-up sections can be as bridge decking systems. Experimental results

are useful in assessing the performance of a system under real-life conditions. This section will briefly examine three different examples of FRP decking profiles and structures tested with the goal of being used for new construction.

Kumar et al. (2003) conducted a fatigue test on a full scale FRP deck built up of prefabricated, commercially available, hollow square sections. The deck sections were made up of glass fiber reinforced polymer (GFRP) tubes with carbon fiber reinforced polymer (CFRP) panels between each layer of tubes. The sections were built up to look like an I-beam, with the assumption that this shape would disperse loading effectively while allowing for acceptable flexural capacity and deflections (Kumar et al. 2003). The deck was preloaded to simulate service conditions before being subjected to two million cycles of fatigue loading. After that, it was statically loaded to failure. After the fatigue loading there was no visible damage, or loss of strength or stiffness. Ultimate failure was reached at approximately four times the service load used and was gradual rather than sudden. It occurred after the glue adhering some hollow sections failed, causing the sections to warp and eventually crack. The system was deemed to be adequately strong and durable, and was refurbished and implemented on campus at the University of Missouri at Rolla in 2000, (Kumar et al. 2003). A picture of the deck system used by Kumar et al. (2003) is shown in Figure 2-5.

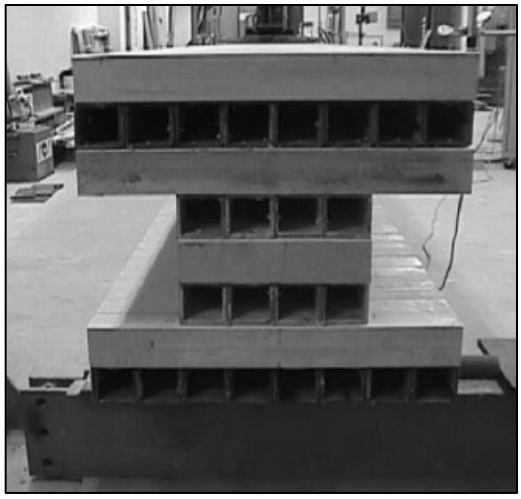

Figure 2-5 Picture of deck section used for experimental testing (Kumar et al. 2003)

A test done by Yanes-Armas et al. (2016) was designed to observe differences between two FRP deck profiles having different geometries but having identical properties otherwise. One profile had trapezoidal geometry while the other was triangular. Failure was gradual in the trapezoidal profile. Small cracks formed in bonds between FRP components, eventually leading to delamination that caused excessive warping. Unlike the trapezoidal profile the triangular one failed suddenly, however the cause of failure was essentially the same. Cracks occurred in bonds but in this profile, it was more comparable to shear cracking rather than cracks opening due to flexure. The triangular profile carried a range of 43-89% more load than the trapezoidal profile (Yanes-Armas et al. 2016).

An all-FRP highway bridge was conceptualized, tested and implemented by Siwowski et al (2018a; b). All structural components of the two-lane road bridge were made from GFRP parts, including the decking. The bridge deck profile was designed as a sandwich panel, the core being supported by closely spaced vertical ribs. The deck was directly adhered to U-shaped FRP girders (Siwowski et al. 2018a). After testing the deck-girder structure for ultimate load capacity, deflection limits, and dynamic response it was deemed to be

acceptable under all service and highway code limits (Siwowski et al. 2018a). The bridge was then implemented in an urban area where it has been constantly monitored by fibre-optic cables built into the superstructure. Monitoring and testing showed that there had been no degradation in the deck or superstructure after eight months of service (Siwowski et al. 2018a; b).

The tests outlined above show that FRP is a viable material to construct bridge decking from and has performed well when implemented as such. Various deck profiles and structures with different material properties have been optimized for individual situations successfully, proving that the variability of FRP is an asset especially for structural use. There have been many more profile designs that have been tested and implemented in new bridge construction other than the ones listed in this section (Hayes et al. 2000; Mara et al. 2013; Zhou et al. 2005), and there have also been plenty of cases where FRP decking has been used to rehabilitate aging infrastructure (Alampalli and Kunin 2002; Liu and Cousins 2007; Loff 2015).

2.2.1.3 Design of All-FRP Decking

One of the main limitations for using all-FRP profiles as bridge decking is the lack of design codes and standards for it (Bakis et al. 2002; Bank 2006a; Keller 2002). Whereas variability in FRP material properties and geometry is advantageous for structures case-by-case, it hinders the ability to standardize a design process for FRP decking (Ascione et al. 2016; Qiao et al. 2000).

Efforts have been made to simplify and standardize a design process for all-FRP bridge decking. The most common author referenced in regard to this seems to be Davalos, who has authored and co-authored several papers on the topic (Chen and Davalos 2014; Davalos

et al. 1996; Qiao et al. 1998, 2000; Salim et al. 1997). Throughout these works, the design of FRP decking has generally been based on three main components: the FRP at a micro level (material properties), macro level (structural properties), and the system level (structural response of the bridge) (Qiao et al. 2000). There are various aspects to consider in the design, the most important being to define the properties of the profile being used and modeling it correctly to predict how it will react to any forces it may be subjected to (bending, shear, etc.) (Davalos et al. 1996). Throughout the literature there are many design and analysis equations used to calculate FRP profile properties, including those for: stiffness, ultimate load capacity, failure mode, and loading cases (Chen and Davalos 2014; Davalos et al. 1996; Qiao et al. 1998, 2000). In all, the design process can be broken down into a few steps:

- Defining FRP profile and bridge geometry along with loading conditions and allowances
- Defining all mechanical and material properties of the FRP profile including equivalent material properties (for cases like sandwich panels with different core and facing materials) using multiple series of equations
- Analysing the system to ensure the load will transfer from the deck to the superstructure properly and that the structural components of the bridge are adequate

Obviously this is a very simplified outline of the design process and there are many parts to each step listed above, but it is an efficient way to generalize the process with so much variability in FRP materials used for decking (Chen and Davalos 2014; Davalos et al. 1996; Qiao et al. 1998, 2000).

2.2.2 FRP Stay in Place Formwork

When constructing reinforced concrete structures, formwork is usually needed. Two main types of formwork exist: temporary and stay-in-place (SIP). For SIP formwork the forms are placed, and concrete is poured, but the forms are not removed when the concrete is set. Depending on how they are designed, these forms can be used in composite with the concrete as a part of the structural system. SIP forms have traditionally been made from corrugated steel or precast concrete. In applications where the structure is susceptible to conditions that can lead to the corrosion of the SIP material, such as bridge decking, this can be a problem. Meltwater contaminated with de-icing salts can infiltrate concrete, causing reinforcement to corrode. Exposed steel, even if treated does not fare much better (Nelson et al. 2014). An alternative is to use FRP profiles as SIP formwork. FRP in combination with concrete can provide the strength and ductility of traditional steel reinforced concrete deck slabs when composite action is achieved all while being less susceptible to corrosion induced degradation (Nelson et al. 2014).

There are many different configurations (layouts) that can be used for FRP SIP formwork. The main goal of any configuration designed is to provide a way for the concrete and FRP to interact and hold together, while achieving composite action (Nelson 2013). Common layouts of FRP SIP formwork can be seen in Figure 2-6. In general, having more surface area for the concrete and FRP to interact promotes better bonding and by extension composite action. Figure 2-6a. shows the “T-Up” system. The “tees” provide many faces for the concrete to bond to and can be modified to have ideal depth and thickness for whatever application is needed. Figure 2-6b. shows a box stiffened plate system. It uses hollow sections for the concrete to bond to and is one of the most used FRP SIP formwork

systems. In Figure 2-6c., a corrugated plate system is shown. They are often used for retrofitting, as they have easily modifiable geometry that mimics the shape of corrugated steel plates used in formwork (Dieter 2002; Nelson et al. 2014; Nelson 2013).

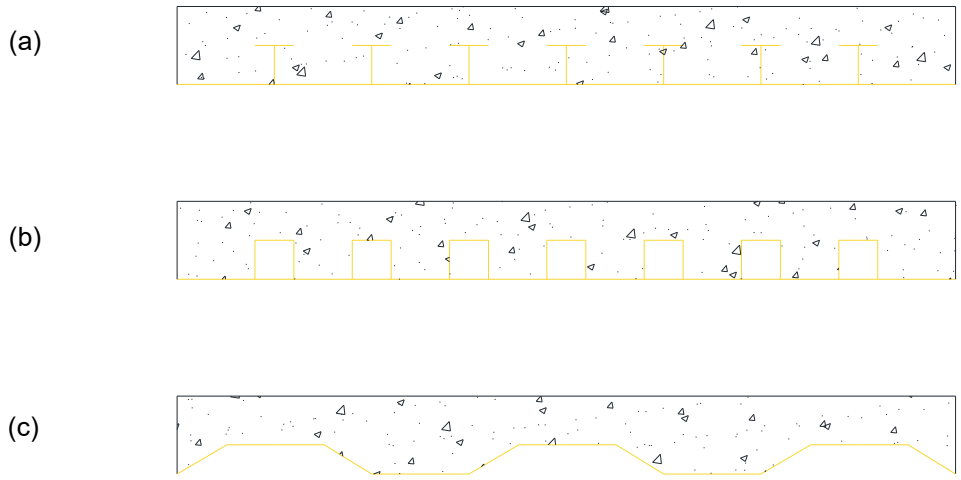

Figure 2-6 Common FRP SIP configurations: (a) "T-up" system, (b) box-stiffened plate system and (c) corrugated plates

Comparing SIP formwork to all-FRP decking profiles there is one main difference that affects the performance of the two methods (other than the obvious addition of concrete to the SIP forms). The geometry of FRP profiles and all the strength and stiffness properties that can be varied with it is not available for SIP formwork. SIP forms are limited to basically rectangular shapes, which may limit some functionality, but is helpful when trying to standardize a design process, as will be outlined later (Nelson et al. 2014).

One of the main challenges to using FRP as a SIP formwork is creating a bond at the concrete-FRP interface strong enough to achieve composite action, thus preventing concrete slippage. Pultruded FRP composites are smooth and need assistance to achieve this bond. There have been a variety of methods used to create and keep a solid bond between the FRP and concrete, including: using shear studs similar to concrete-steel

composite structures, using pultruded sections that have shear stud type ridges or grooves as a part of the structure, bonding a layer of coarse aggregate on top of the formwork to create a rougher surface, and applying an adhesive to the form then pouring concrete while this adhesive is still wet. Combinations of these methods have also been used (Dieter 2002; Hanus et al. 2009; Honickman et al. 2009; Nelson et al. 2014; Nelson 2013; Oliva et al. 2007).

Shear stud connected profiles show the most concrete slippage of the methods mentioned above, although this is counteracted by the studs themselves (more so than geometric pultruded profiles). These types of SIP forms go through three main stages while being loaded: when the concrete-FRP interface is fully bonded and force transfers through it, when slippage occurs and the studs start to take over the force transfer, and when the concrete is effectively debonded and the studs transfer all forces between the concrete and FRP (Gong et al. 2019).

In general, any pultruded geometric profile has been shown to create an effective bond between the FRP and concrete (Nelson et al. 2014). While some slippage occurs, the concrete is held in place more effectively by the geometric profile. Throughout the literature there have not been many comparative studies between the effect of geometric profiles versus studs, but it seems that the profiles are stiffer and allow for less slippage than stud systems (Dieter 2002; Gong et al. 2019; Honickman et al. 2009; Nelson 2013).

The methods using aggregate or adhesive as the main bonding mechanism (“flat” systems) are also effective at creating an initial bond. These systems have been shown to be stiffer than those using geometric profiles or shear studs, meaning outright concrete failure occurs rather than slippage (Honickman et al. 2009).

Discussion regarding modeling FRP SIP formwork and how different bond methods are incorporated is covered in Section 2.3.

2.2.2.1 Experimental Testing of FRP SIP Decking

Many tests have been done to observe the behaviour of FRP SIP deck forms under highway bridge-type loading conditions, like with all-FRP decks. As mentioned, with FRP SIP formwork there is less variability than with all-FRP decks. In theory, this means test results would be more likely to follow patterns and trends because the geometry of the FRP component does not have a direct impact on the mechanics of the deck.

Testing by Dieter aimed to prove that FRP SIP formwork was a viable option for bridge decking (Dieter 2002). The reinforcement system used was comprised of box-stiffened plates with aggregate bonded to the base plate, as well as a bi-directional GFRP grid having I-sections in the transverse direction, and longitudinal oval bars cast into the concrete slab. The testing examined the response of the FRP SIP system under bending in positive and negative moment regions and how it would react to fatigue loading (Dieter 2002). To simulate positive moment conditions, three-point bending tests were carried out. The specimens were preloaded to simulate service conditions, loaded statically until failure, and after failure was deemed to have occurred, the failure load was sustained to observe post-ultimate behaviour. Two specimens had an FRP mesh placed near the top of the concrete to control cracking while one did not. The specimen without the FRP mesh experienced more cracking but all failed due to concrete crushing at a similar load. The main difference between the specimens with and without crack control measures was in post-ultimate behaviour. The ones with the FRP mesh maintained strength and stiffness post-ultimate failure while the one without the mesh experienced a constant drop in these

properties (Dieter 2002). To simulate negative moment conditions, two specimens were subjected to a two-span, five-point bending test. One span was loaded up to 50 kip and had that load sustained until failure occurred, the other span was loaded continuously until failure. Cracking occurred near the middle support throughout testing and both failed at similar loads, but failure mode was different. One specimen experienced a sudden two-way shear failure that originated at the middle support. The other had two-way shear cracking but its concrete debonded from the FRP in the continuously loaded span before the specimen failed due to shear (Dieter 2002). Fatigue testing was carried out using the same setup as the negative moment test, one span had load held at a constant amount while the other was subjected cyclic loading. No cracking, or strength or stiffness degradation was observed during the cyclic loading. The specimen was brought to failure like in the negative moment tests where it failed at a slightly lower load due to punching shear (Dieter 2002). Conclusions from this testing showed that failure differs in positive and negative moment regions, the former having crushing govern while the latter was shear controlled, and fatigue loading had little effect on the specimens. The system overall was deemed viable for highway use (Dieter 2002).

Many other tests have been conducted following a similar experimental program, testing different FRP SIP configurations under positive and negative bending conditions along with fatigue loading. The results of all of these yielded some general observations about the performance of FRP SIP formwork:

- Concrete always governed failure, usually due to crushing under positive bending and two-way shear under negative bending

- Fatigue loading did not cause strength or stiffness degradation in FRP SIP formwork for simulated highway conditions
- SIP forms with no top reinforcing (either compression bars or crack controlling mesh) can retain strength and stiff post-ultimate failure

These observations are stripped down to a very basic level, but the results have shown that structurally, FRP SIP formwork is a viable system for use in bridge decking (Cheng and Karbhari 2006; Dieter 2002; Gai et al. 2013; Hanus et al. 2009; Nelson et al. 2014; Nelson 2013; Noël and Fam 2016; Oliva et al. 2007).

There has not been an abundance of durability testing done on FRP SIP formwork, like there has been for all-FRP decking profiles. But studies done have shown that FRP SIP decking panels can be resilient when exposed fire or extreme heat conditions (Nicoletta et al. 2018) and freeze-thaw cycles (when frost heave in concrete can be avoided) (Boles et al. 2015; Wardeh et al. 2010).

2.2.2.2 Design of FRP SIP Decking

While FRP SIP forms seem practical for highway use, there is currently no design code or standard for transportation departments to follow to implement them. However, there has been some work done on coming up with design equations to help FRP SIP forms become a more standard bridge component.

Nelson and Fam (2014) created a finite element model to predict, among other properties: moment curvature response in longitudinal and transverse directions, deflected shape of the concrete, and ultimate capacity given punching shear failure for FRP SIP forms (Nelson and Fam 2014). This model was used in a parametric analysis of multiple deck forms to explore the effects of various conditions on the properties mentioned. The results from the

model matched well with experimental values, but the model was not practical for design use as it was not user friendly and was based on complex mathematics that a general design engineer would not be expected to understand (Nelson and Fam 2014). To make a more user-friendly model, Noël and Fam came up with two design equations based on the parametric study: one for ultimate load capacity and one for stiffness. The equations were developed assuming composite action would be achieved and the FRP panels would act as bottom reinforcement (Noël and Fam 2016).

To produce the full equations, some simple base equations were developed based on important parameters identified in Nelson and Fam's model. The deck span (L), deck width (B) and an effective reinforcement index (ω_{eff}) were deemed to be the most influential on stiffness and ultimate capacity (Nelson and Fam 2014). The effective reinforcement index was a variable used to compare and standardize the properties of all FRP SIP components, no matter what material properties or configuration they have. It was developed by finding FRP reinforcement ratios in both transverse and longitudinal directions and relating them to steel using the respective Young's moduli. ω_{eff} was a weighted average of these transformed ratios. A linear relationship was noticed between the punching shear (P_u), and ω_{eff}. This relationship was what a first simplified equation was based off. ω_{eff} did not have much of an effect on stiffness (K), however it was noted that it had more of an influence at higher loads than lower ones. The relationship between deck span and P_u was also found to be linear while its relationship with K followed a power curve. The relationship between deck width and P_u and K was more difficult to determine through a model because it was a localized occurrence; finite sections of the deck were defined and considered for this. The relationship also considered the aspect ratio (B/L) of the form. Punching shear was found

to govern failure when the aspect ratio was greater than 1.5, so Noel and Fam wanted to find simple expressions to predict ultimate failure when aspect ratio was below this limit (Noël and Fam 2016).

The final design equations are presented below. Equation (2-1) is for nominal strength and Equation (2-2) is for stiffness.

$$\frac{P_n}{b_o d_{ave}\sqrt{f'_c}} = 0.375\left(\omega_{eff} + 0.0334\right)(B + 4.0)(5.6 + L) \quad (2\text{-}1)$$

$$\frac{K}{\bar{d}_{ave}^3} = (1.8 \times 10^{-4})\omega_{eff} B L^{-3.66} \quad (2\text{-}2)$$

where: P_n is the nominal strength

K is the slab stiffness

b_o is the perimeter of the punching shear failure plane

d_{ave} is the average depth from the concrete compressive face to the centroid of FRP reinforcement

f'_c is the concrete compressive strength

ω_{eff} is the effective reinforcement index

B is the deck width

L is the deck span

Noël and Fam noted that although the same variables were used to derive these equations, they were not dependent on one another. These equations could also be slightly modified depending on aspect ratio, where B could be substituted for an equivalent value of L, or vice versa (Noël and Fam 2016).

The design equations were tested using a database of 52 FRP SIP systems from various experiments, including those by Dieter and Boles mentioned above (Boles et al. 2015; Dieter 2002; Noël and Fam 2016). These systems had varying properties including

compressive strength of concrete, SIP formwork dimensions, type of FRP configuration, and bond adhesion methods, among others. When comparing the model results to experimental results there was an 87% correlation between the two for nominal strength with a standard deviation of 19%. For stiffness, the correlation was 242% with a standard deviation of 164%. Clearly the stiffness equation did not match with experimental results used in the study, but it was concluded that it could provide a fairly accurate estimate of whether service load deflections were acceptable or not (Noël and Fam 2016).

These equations are not refined enough to be considered for practical design use, being subjective to only the experimental results used in the parametric study. Other parameters would eventually need to be considered including durability factors, deck connections, bond strength, and compression reinforcement (Noël and Fam 2016). The equations do form a basis upon which to continue studying in hopes of one day standardizing a design process for FRP SIP formwork for bridge decking.

2.2.3 Other FRP Composite Bridge Decking Systems

While concrete is the most common material used in composite with FRP for bridge decking applications, the use of other materials has been studied. Steel, timber, and foam composites have been researched and are discussed in this section.

2.2.3.1 FRP-Foam Composite Decking

Other than concrete, a combination of FRP and foam is the most common composite decking system currently. The most common configurations tested and used are sandwich panels with a pure foam core, sandwich panels with a foam-web core, and profiles having the voids filled with a foam core (shown in Figure 2-7). These have been tested

experimentally and in the field, yielding positive results (Bank 2006b; Huo et al. 2015; Volz et al. 2017).

In general, FRP-foam composites have similar properties to all-FRP beams or profiles up to their ultimate stress limits but post-ultimate behaviour differs between the two. For an all-FRP profile or section, failure is sudden and catastrophic (Bank 2006a). In the majority of sandwich panel FRP-foam composites tested for bridge decking use, failure tended to happen either in the compression face or by the delamination, rendering composite action obsolete (Huo et al. 2015; Manalo et al. 2017; Volz et al. 2017). When these types of failures occurred, the foam often retained its structural integrity and although it could not carry any more load, the shape remained to provide at the very least a surface for users to be suspended on. The post-ultimate behaviour was not unlike that of FRP SIP formwork, albeit less effective. This contrasts with an all-FRP deck failing or a case in which the foam core of the composite fails and provides no structural integrity, which could lead to more damage to the superstructure of a bridge (Bank 2006b).

Overall, FRP-foam composites in decking combine the beneficial properties of all-FRP decking (corrosion resistance, high strength to weight ratio, etc.) with improved post-ultimate behaviour (Manalo et al. 2017). This along with positive results from field implementation makes them an attractive alternative to traditional decking materials (Volz et al. 2017).

Figure 2-7 FRP deck profile with foam-filled sections (Volz et al. 2017)

2.2.3.2 FRP-Timber Composite Decking

Timber is commonly used in bridge decking, but mostly for short span bridges in low traffic volume areas (Keller 2002). It is not as durable as concrete and its lighter weight is not much of an asset for decking applications; timber is not as practical for use in highway bridges as concrete. Research has been done on timber-FRP composites to see if they could be used as a practical decking material for short-span and highway bridges (Keller et al. 2014; Lopez-Anido and Xu 2002; Qi et al. 2017).

One way in which timber-FRP composites have been used for bridge decking was having sandwich-style beams encased in an FRP skin that were able to be built up modularly (Figure 2-8) (Lopez-Anido and Xu 2002; Qi et al. 2017). This application could be used as an alternative to all-FRP beams, allowing for savings on material costs as FRP panels are less expensive than pultruded FRP beams (Qi et al. 2017). The FRP gave the composite increased strength and stiffness while also protecting the wood core from environmental wear (Lopez-Anido and Xu 2002). Experiments on these types of beams have been done with variable parameters including wood type, wood orientation, fiber orientation in FRP sandwich faces, and the ratio of wood to FRP. In experiments done by Qi et al., wood-only

control beams all failed in shear, but when an FRP skin was introduced the shear cracking in the wood was contained and FRP properties governed, improving bending capacity by 50% at minimum (Qi et al. 2017). Experiments conducted by Lopez-Anido and Xu showed that adding FRP sandwich facings to glulam panels with unidirectional fiber orientation parallel to the wood grain could significantly improve ultimate load capacity and stiffness (Lopez-Anido and Xu 2002).

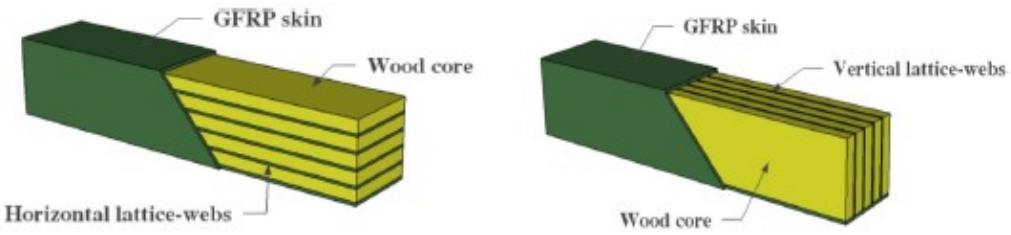

Figure 2-8 Drawing of FRP-timber composite beams (Qi et al. 2017)

Another way to use timber and FRP compositely is to make a sandwich structure with FRP panels and a low-density timber core. Experimental testing of this method showed results like those of FRP-foam sandwich panels, which makes sense as the concept of the two methods is identical. A specimen made of GFRP face sheets and a balsa wood core resisted fatigue loading with no significant damage, and then when loaded to failure showed post-ultimate behaviour identical to FRP-foam sandwich panels (Keller et al. 2014). The post-ultimate capacity of the balsa wood was better than that of foam as well (Keller et al. 2014; Manalo et al. 2017). Ultimate limit states and serviceability of the deck system were satisfactory as defined by the Swiss Standards Association, leading to it being implemented as a replacement for an aging bridge deck in Switzerland in 2014. The deck was made of one piece which reduced the construction period by an estimated 40 days compared to a

concrete bridge deck and eliminated the need for thermal expansion joints (Keller et al. 2014).

In general, FRP can improve the performance of timber used for decking purposes. FRP-timber composites act similarly to FRP-foam, the former outperforming the latter in some cases. Experimental testing has yielded promising results in increasing the capacity of rectangular wood beams and systems have been implemented in the field. Overall, FRP-timber composites have been proven to be effective for short-span bridge decking (Keller et al. 2014; Lopez-Anido and Xu 2002; Qi et al. 2017).

2.2.3.3 FRP-Steel Composite Decking

There has not been much research done on using steel in composite with FRP for bridge decking compared to other materials. The main area of research regarding steel and FRP in composite is using FRP based decking on a steel superstructure, slab-on-girder style (Figure 2-9). In general, FRP-steel decking mimics steel-concrete composite decking, in the cases outlined below the FRP takes the place of concrete. One proposed method would see an FRP panel bolted to steel girders (Satasivam et al. 2017) and another similar method would see a foam filled FRP sandwich-panel system adhered to steel girders (Jiang et al. 2013; Manalo et al. 2017). The goal of creating FRP-steel composite decking has been to improve the shear capacity compared to steel-concrete composite decking. Experimental tests by Jiang et al. (2013) were successful at this, but the method has only been analysed experimentally and by finite element model. There have been no analytical models developed nor parametric studies completed on FRP-steel composites. More research needs to be completed before FRP-steel composite decking can be implemented in real-life situations (Jiang et al. 2013).

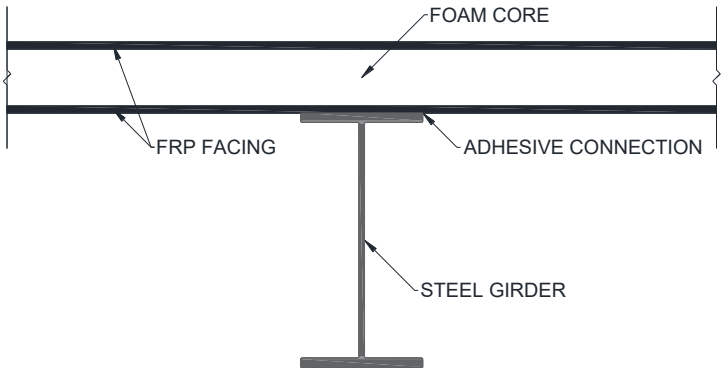

Figure 2-9 Concept of steel-FRP sandwich panel composite (Manalo et al. 2017)

2.3 REVIEW OF BEAM THEORY USED IN ANALYTICAL MODELLING

This section will deal with numerical modelling of all-FRP and FRP SIP formwork under bending conditions. Finite Element Methods (FEM) can be and have been used extensively in modelling these types of conditions but since FEM was not used in this study, it will not be covered.

All beams tested in the experimental program were subjected to four-point bending. Beams were subjected to two equal and symmetric point loads, creating two zones of maximum shear and a plateau for the maximum bending moment. This is shown in Figure 2-10, below. Deflection response of the beam can be calculated with the base equations: (2-3), (2-4), and (2-5) (Sadeghian et al. 2018).

$$\Delta_B = \frac{P}{96D}(2L^3 - 3Lx^2 + x^3) \tag{2-3}$$

$$\Delta_S = \frac{P}{4GkA}(L - x) \tag{2-4}$$

$$\Delta_{TOTAL} = \Delta_B + \Delta_S \quad (2\text{-}5)$$

where: Δ_B is the deflection due to bending moment

Δ_S is the deflection due to shear

P is the applied load on the beam

D is the flexural stiffness of the beam

G is the shear modulus of the beam

k is the shear coefficient of the section (explained in detail below)

A is the shear area of the cross section

L is the total span length

x is the shear span

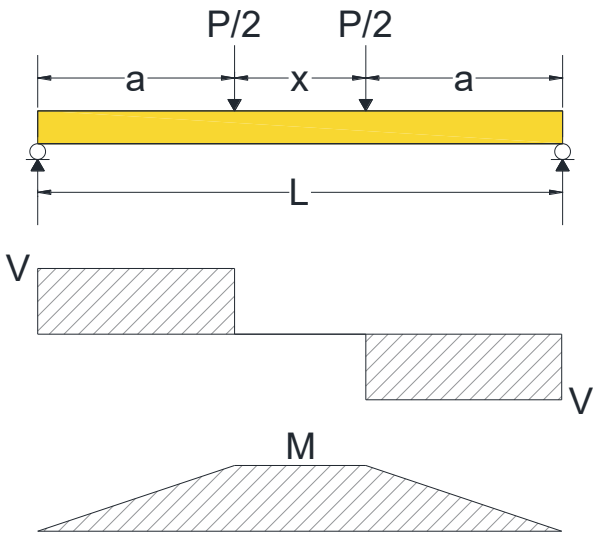

Figure 2-10 Shear and moment diagrams of a beam subjected to four-point bending

Modelling the deflection due to bending under four-point bending is straightforward so long as the stiffness properties are known, deflection due to shear is slightly more complicated.

2.3.1 Shear Effect on Deflection

Like traditional materials, the shear modulus for FRP is generally much lower than the longitudinal elastic moduli. This causes significant amounts of shear deformation that must be considered when modelling beam behaviour under bending (Omidvar 1998). The basis of a shear deformation formula is consistent throughout the literature for the most part; components P, L, x, G and A are all present in some form for all formulae (x is sometimes interchanged with the term a, shown in Figure 2-10. The main difference between formulae used in the literature is the term k, the shear coefficient and how it relates to the shear area of the cross-section, A. The shear coefficient is a constant which accounts for shear stress not being evenly distributed over a beam cross-section (Bank 1989).

There have been various methods used to calculate the value of k. The basis for these is to modify the shear area of a given cross-section of an FRP beam. In the case of the square hollow section seen in Figure 2-11, the unmodified shear area is the total area of the web of the section (shown in grey). For this, the shear coefficient would be represented as:

$$kA = A_w \tag{2-6}$$

where: k is the shear coefficient of the section

A is the shear area of the cross-section

A_w is the area of the cross-section web

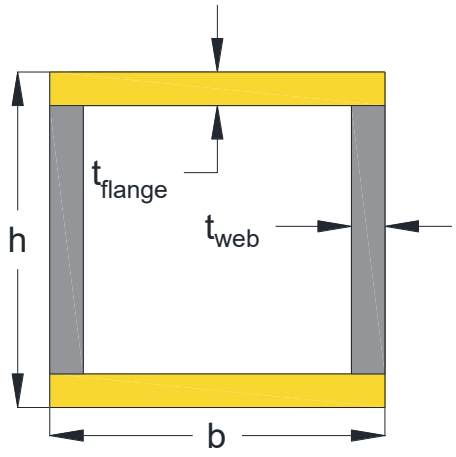

Figure 2-11 Cross-section of square HSS – gold represents flange area, gray represents web area

Bank (1989) derived a formula for k based on an earlier one by Cowper (1966) that considered the longitudinal and shear moduli as well as the Poisson's ratio in the longitudinal direction and assumed uniform shear stress along the cross-section (Bank 1989; Cowper 1966). This was further modified by Omidvar (1998) to include the Poisson's ratio in the transverse direction. When simplified, Omidvar's equation can be approximated as follows (Omidvar 1998):

$$kA = t_w(h - 2t_f) \tag{2-7}$$

where: k is the shear coefficient of the section

A is the shear area of the cross-section

h is the height of the cross-section

t_w is the thickness of the web

t_f is the thickness of the flange

Comparatively, Roberts and Al-Ubaidi (2002) derived an equation for k based on transverse shear strain energy while assuming non-uniform shear stress along the cross-section (Roberts and Al-Ubaidi 2002):

$$kA = t_w(h - t_f) \tag{2-8}$$

These two formulae, along with others derived by methods such as the virtual work theorem (Kollar and Springer 2003) were compiled and used in a parametric study to estimate the deflection of a beam under four-point bending (Minghini et al. 2014). Eight different methods were used to calculate the shear coefficient. Almost all could be simplified down to the basic components seen in Equations (2-7) and (2-8) with some sort of modification for one of them (the components being t_w, t_f, and H). The results showed a 13% spread between shear coefficient values with Omidvar's model being the most accurate compared to experimental results for shear deformation of I-beams (Minghini et al. 2014).

The other component in determining the stiffness of a beam due to shear is its shear modulus (G). This value has been derived in different ways for FRP materials. It can be obtained experimentally by means of a three-point bending test (Bank 1989; Mottram 2004). This method, originally proposed by Bank (1989), had the user obtain load-deflection values from experimental three-point bending tests of different sized beams and graph the relationship between deflection-to-load ratio against the slenderness ratio of a beam (a property which determines the shear contribution to deflection in the beam). Once the relationship was plotted, a linear regression was performed. The shear modulus for the

material was taken as the y-intercept of the plotted line (Bank 1989). An example of a plot used to calculate shear modulus is shown in Figure 2-12.

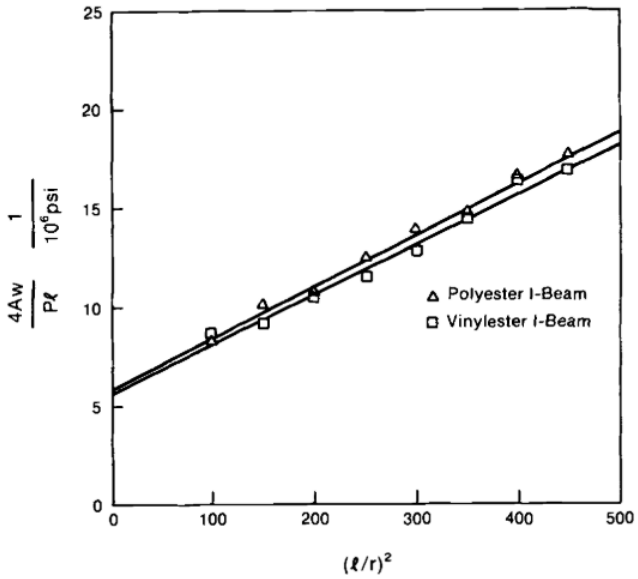

Figure 2-12 Plot used in graphical method of finding shear modulus, y-intercept value would be considered shear modulus (Bank 1989)

This method does have issues in that very small changes in experimental values can have a large effect on the slope of the regression line and can lead to significant fluctuation in the intercept value and in turn shear modulus (Mottram 2004; Roberts and Al-Ubaidi 2002). After testing coupons for shear modulus using a variety of different experimental methods, Mottram found that it is best to assume that the shear modulus in any given pultruded FRP material is not one singular value but rather a small range of values. It was concluded that this range should have a lower bound of 3 GPa with a variable upper bound dependent on the cross-section of the pultruded beam, ending up somewhere between 4 and 5 GPa (Mottram 2004; Nguyen et al. 2018).

2.3.2 Failure Modes

There have been multiple different failure modes observed throughout various tests for all-FRP sections, but it seems that those due to pure longitudinal tension or compression are less likely to occur than those influenced by transverse forces or shear (Minghini et al. 2014). Although local buckling due to pure compression is a possibility, often it is some combination of both transverse shear and bending forces that cause failure in FRP beams subjected to bending (Bank 2006a). There are a variety of failure modes that encompass both flexure and shear, such as local buckling (in either the web or flange), web crippling, or web crushing. Pure shear failure is also possible (Bank 2006a; Borowicz and Bank 2011; Minghini et al. 2014). There are also many factors that can affect which failure mode will occur such as section geometry (Muttashar et al. 2016), loading rate (Das et al. 2007), and how a specimen is loaded (loading through bearing plates have been found to alter failure mode) (Borowicz and Bank 2011).

Ultimate load in all-FRP beams under bending can be somewhat tricky to calculate because of the many possible failure types and factors affecting them. It has been seen through multiple experimental tests that to accurately predict the failure load a combination of bending and shear forces must be considered (Bank 2006a; Muttashar et al. 2016). For local buckling or crushing failure, neglecting shear has been seen to consistently overestimate ultimate load (Ascione et al. 2013). To generalize an equation that predicts ultimate failure load, both flexural and shear properties must be utilized. Suggested by ASCE, an interaction equation that accounts for both flexure and shear is presented as Equation (2-9) (ASCE 1985):

$$\frac{\sigma_{act}}{\sigma_{all}} + \frac{\tau_{act}}{\tau_{all}} \leq 1 \quad (2\text{-}9)$$

where: σ_{act} is the actual flexural stress in a bending specimen

σ_{all} is the allowable flexural stress in a bending specimen

τ_{act} is the actual shear stress in a bending specimen

τ_{all} is the allowable shear stress in a bending specimen

While σ_{all} and τ_{all} are based on material properties, σ_{act} and τ_{act} can be calculated by basic mechanical equations, specific to four-point bending:

$$\sigma_{act} = \frac{Mc}{I} \quad (2\text{-}10)$$

$$M = \frac{Pa}{2} \quad (2\text{-}11)$$

$$\tau_{act} = \frac{VQ}{It} \quad (2\text{-}12)$$

$$V = \frac{P}{2} \quad (2\text{-}13)$$

where: M is the bending moment

P is the applied load on the specimen

V is the shear force in the specimen

I is the cross-sectional moment of inertia

Q is the cross-sectional first moment of area

c is the neutral axis depth

t is the web thickness of the section

a is the distance from the support to the closest applied loading point, in four-point bending

Rearranging and combining the above equations gives a prediction for ultimate load that considers shear and bending effects:

$$P = \left(\frac{ac}{2I\sigma_{all}} + \frac{Q}{2It\tau_{all}}\right)^{-1} \quad (2\text{-}14)$$

This equation weights flexural and shear behaviour equally, which may not always be accurate depending on loading conditions. However, it has been used to reasonably predict ultimate failure loads for hollow FRP beams under four-point bending that fail due to local buckling (Muttashar et al. 2016).

2.3.3 Considerations for Modelling FRP SIP Formwork

Modelling FRP SIP formwork is in many ways like modelling all-FRP behaviour under bending. The addition of concrete adds an extra non-linear component to the stress response of the section as well as different failure modes to consider. As noted above, failure in FRP SIP formwork is almost always governed by the concrete rather than the FRP, although failure of the bond between FRP and concrete must also be considered (Nelson et al. 2014).

Concrete failure in FRP SIP formwork can be modelled using the same general process as a reinforced concrete beam or slab depending on dimensions (Honickman et al. 2009; Nelson et al. 2014). A variety of failure cases can be considered, though from the literature it seems as if shear failure usually governs for SIP formwork (Cheng and Karbhari 2006;

Dieter 2002; Nelson et al. 2014; Noël and Fam 2016). Modelling a bond failure is generally less straightforward than pure FRP or concrete failure, as the type of bond and its effectiveness at transferring forces is the determining factor; the amount of composite action in the system must be assessed for an accurate model (Nelson et al. 2014; Oliva et al. 2007). Bond failure will occur when the shear stress between the FRP and concrete exceeds the bond strength of the system. The bond stress and strength are variable between specimens and depend on bond type. Studies have been done to model bond effectiveness for different bonding types with good accuracy, although full composite action is usually assumed even when slippage occurs (Goyal et al. 2016; Oliva et al. 2007; Yuan and Hadi 2018).

Along with different failure modes, another main component in modelling FRP SIP formwork is accurately predicting the stiffness in specimens subjected to bending (or stiffness increase compared to all-FRP specimens). Considerations for this include neutral axis location (and how it is influenced by cracking) and again the bond between FRP and concrete (Honickman et al. 2009; Nelson et al. 2014). An approach for modeling moment-curvature and eventually load-deflection response in FRP SIP formwork has been implemented successfully by Honickman et al. (2009). The process was based off equilibrium of forces and strain compatibility. It was carried out by calculating stresses in layers of a cross-section for different strains at the extreme tensile fiber, finding forces from these and using to calculate the sum of moments across the section. Curvature was taken as the slope of the strain profile for each initial strain. The sum of moments and strain-based curvature was taken as a point on the moment curvature profile of the specimen, and the process was repeated to establish a full moment-curvature response.

Once the full response was known, load-deflection could be found by integration (Honickman et al. 2009). Like others, this process assumed full bond between FRP and concrete (Honickman et al. 2009).

This section provided an overview to what must be considered when modelling FRP SIP formwork. There is much more that goes into it and it is far more complex than these couple paragraphs would indicate. Most modelling for FRP SIP forms has used FEM, but authors like Honickman have shown it is possible to forgo these methods.

CHAPTER 3 EXPERIMENTAL PROGRAM

The goal of the experimental program was to design and test bridge decking systems using commercially available FRP materials. The FRP materials used were pultruded, square, hollow sections originally 3 m in length (most were eventually cut to be smaller for testing). The FRP was composed of glass fibers and vinyl ester matrix. The sections had outer dimensions of 100 mm by 100 mm and wall thickness of 6 mm. A picture of a beam used for bending tests is shown in Figure 3-1.

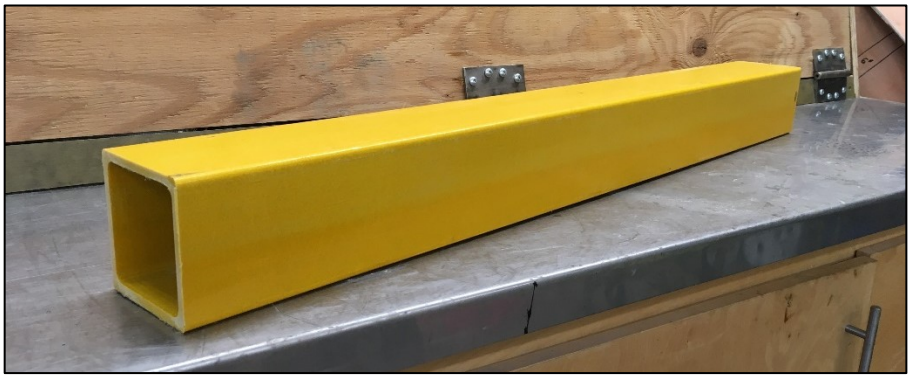

Figure 3-1 1 m long hollow FRP section

The sections were not wide enough to cover a whole section of a bridge like the decking panels mentioned in the previous section. Conceptually, individual sections would be built up modularly and used in slab-on-girder style bridge deck, replacing traditionally used reinforced concrete slabs. The built-up sections would be laid perpendicular to the direction of traffic. An image of how the decking system would be implemented in a slab-on-girder type application is shown in Figure 3-2, below (note that the concrete slabs shown in the image are only for a reference of what would be replaced by the FRP decking system).

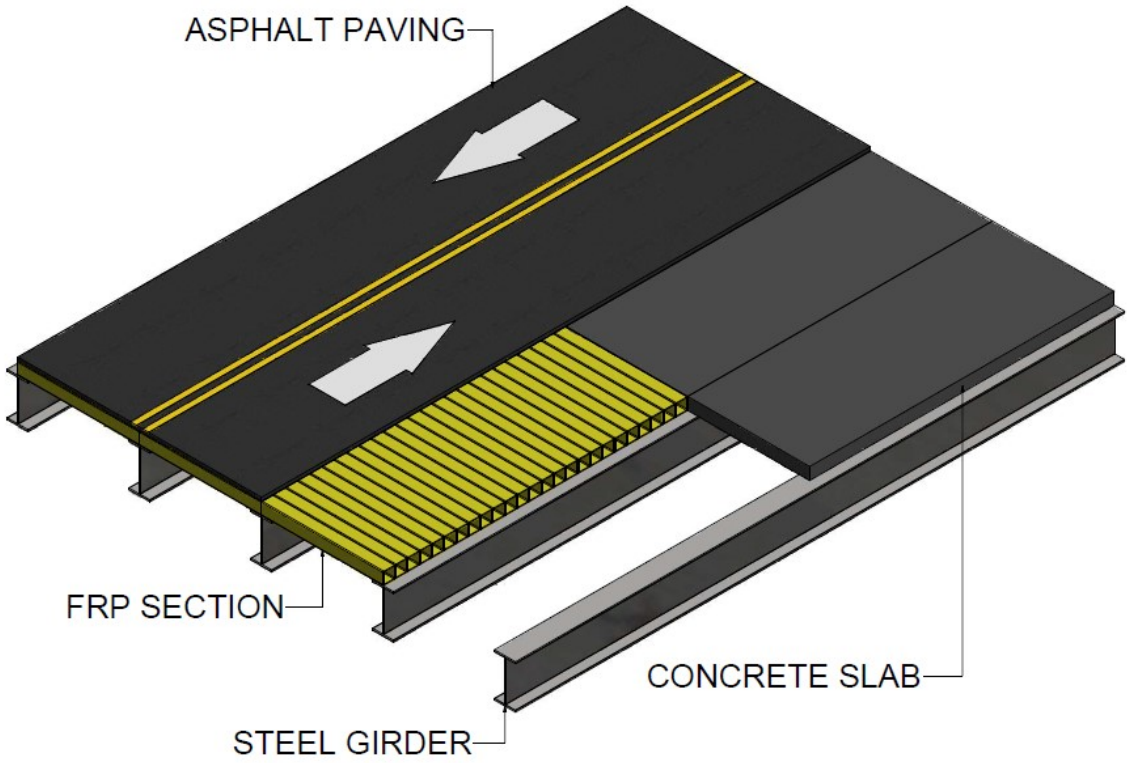

Figure 3-2 Components of a slab-on-girder bridge

According to the Canadian Highway Bridge Design Code, concrete decking slabs must be designed considering: flexural and axial loads, shear and torsional effects, crack control, and immediate and long-term deformations (CSA Group 2019). Based on this, it was decided that the test program for this study would focus on how individual specimens would respond under transverse flexural loading, considering shear effects. Immediate deformations (deflections) due to loading were examined as a part of this. Four-point bending tests were chosen to assess the FRP specimens to loosely simulate wheel-loading conditions that would be experienced on a typical highway bridge.

This chapter will discuss the mechanical properties of the FRP material used, the test matrix for the four-point bending tests, procedure for specimen fabrication, test set-up and instrumentation, and a discussion of the results.

3.1 FRP PROPERTIES

There were two main components to the testing of material properties for the FRP specimens used in this study. The first was to characterize the physical properties of the material, including the fiber layout and the material composition by weight. The second was to determine the material properties of the FRP, specifically: tensile, compressive, and shear. The FRP sections were manufactured by and purchased from Hangzhou Wind Composite Co., Ltd. (a division of parent company Wind International Trade Development Ltd.). A data sheet was provided by the company with values for mechanical properties such as strength and elastic modulus for tension, compression, flexure, and shear for the FRP sections. Upon initial four-point bending testing and subsequent attempts at modelling the behaviour of the sections, it was thought that the properties listed may not have been accurate. Test standards used by the manufacturer to obtain mechanical properties followed ASTM (American Society for Testing and Materials) guidelines but were designed for "structural plastics". It was decided that testing for mechanical properties needed to be done independently using ASTM standards used for testing FRP materials. The details of these tests are outlined in the following subsections.

3.1.1 Properties of Test Materials

The fiber orientation of the FRP material being studied was found by means of an ignition loss (burnout) test. The testing was carried out according to ASTM D2584: Standard Test Method for Ignition Loss of Cured Reinforced Resins (ASTM 2018). Six test specimens were cut from one of the FRP beams. The specimens were square in shape, having length and width of 25 mm (1") and thickness 6 mm. Each specimen was weighed and placed in a crucible which was then inserted into a small furnace that had been heated to

approximately 575° C. Once in the furnace the vinyl ester matrix ignited and burned away, leaving only the glass fibers. The specimen was removed from the furnace and the remaining fibers were weighed. From the two weights (before and after burnout) the ignition loss weight percentage was calculated using Equation (3-1). The results from ignition loss testing are presented in Table 3-1.

$$ILW\% = \frac{W_0 - W_3}{W_0} \times 100 \tag{3-1}$$

where: ILW% is the ignition loss weight percentage

W_0 is the weight of the original specimen (fiber and matrix)

W_3 is the weight of the remaining fiber after burnout

Table 3-1 Ignition loss test results

Specimen I.D.	Specimen Weight (g)	Fiber Weight (g)	ILW (%)
IL1	7.4	4.9	33.8%
IL2	7.6	5.3	30.3%
IL3	7.7	5.3	31.2%
IL4	7.8	4.9	37.2%
IL5	7.9	5.0	36.7%
IL6	8.0	5.4	32.5%
Mean	7.7	5.1	33.6%
Standard Deviation	0.2	0.2	2.6%

The resin matrix of all specimens burned away completely, which allows for the assumption that the FRP material is only made up of resin and matrix. The significance of this is that the ignition loss can be considered as the resin (matrix) content

The ignition loss specimens before testing are shown in Figure 3-3. The fiber components of the specimens after ignition loss are shown in Figure 3-4. The ignition loss test revealed that the FRP material has unidirectional fibers oriented at an angle of 0° in relation to the length of the tubes. These unidirectional fibers are sandwiched between two mats of randomly oriented chopped fiber.

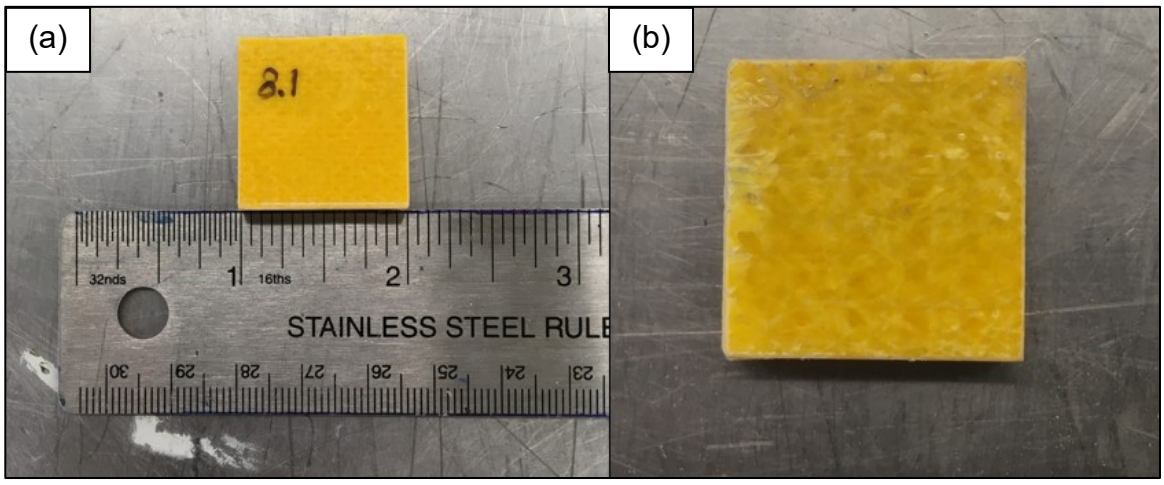

Figure 3-3 Ignition loss specimen before testing: (a) front side with ruler for scale and (b) back side

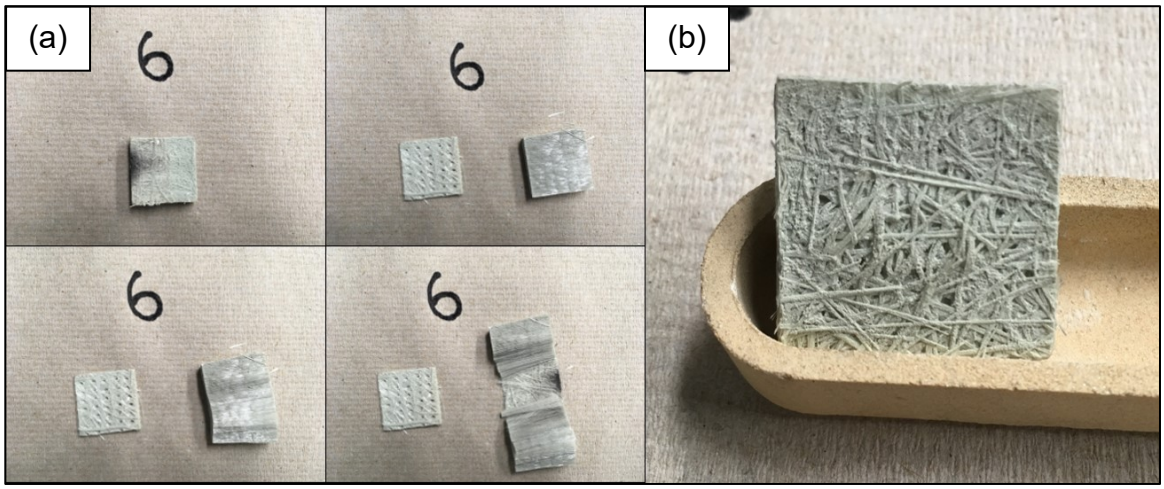

Figure 3-4 Ignition loss specimens after testing: (a) components of specimen separated and (b) chopped fiber mat

3.1.2 Material Properties

3.1.2.1 FRP Tension Testing

Tension testing was carried out based on ASTM D3039: Tensile Properties of Polymer Matrix Composite Materials (ASTM 2017). Five coupons were cut out of one of the FRP sections, each was set into grips in a 2MN Instron 5590-HVL Static Hydraulic Universal Testing System. The coupons were all an identical size, having a length of 609 mm (24”), width 50 mm (2”) and thickness 6 mm. The gauge length for each specimen was 203 mm (8”). Axial strain gauges were attached to the center of the front and back of four of the specimens (T1 through T4). This differed slightly from the ASTM guideline so one specimen (T5) was affixed with three strain gauges attached: one on the front in the center and two on the back in the middle of the gauge length and one eighth of the width in from either side, as per the standard. The specimens were pulled apart at a rate of 2 mm per minute until failure was achieved. A drawing of the test setup is shown in Figure 3-5, a picture of a tension specimen during testing is shown in Figure 3-6 (below).

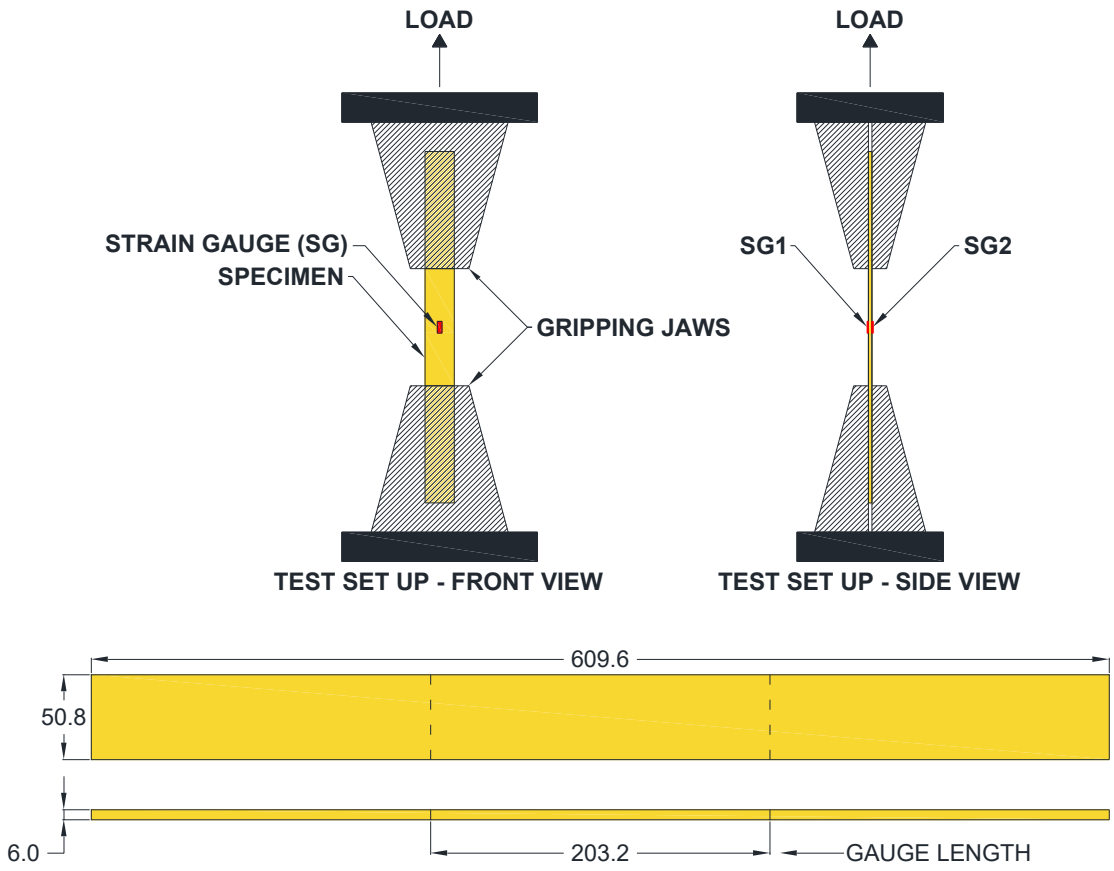

Figure 3-5 Details of tension test set up and specimen, all dimensions in mm

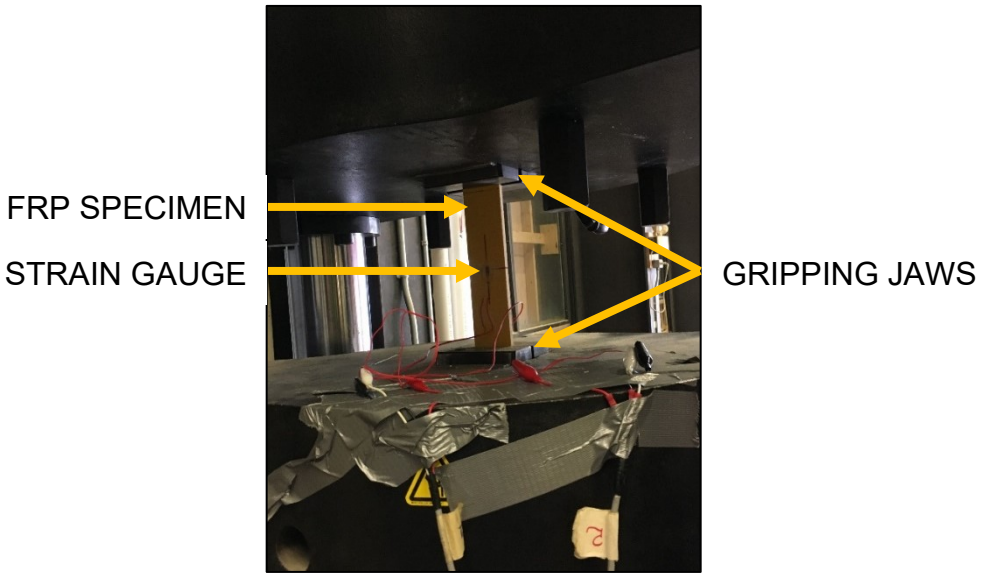

Figure 3-6 Tension specimen in test fixture

The results from the tensile testing can be seen in Table 3-2. These values were used for calculations and in analytical models for predicting the behaviour of the bending specimens.

Table 3-2 Tensile material properties

Specimen I.D.	P_{max} (kN)	F_{tu} (MPa)	ε_{tu} (με)	E_t (GPa)
T1	180.1	581.6	18775	33.1
T2	177.8	574.0	18490	34.9
T3	184.7	596.3	19918	36.2
T4	187.3	605.0	18890	33.4
T5	198.2	640.2	18645	38.4
Mean	185.6	599.4	18943	35.2
CV	4%	4%	3%	6%

The stress-strain curves for each specimen, shown in Figure 3-7, followed a generally linear pattern and were all similar. The results from these were used in calculating the tensile strength and modulus. The specimens started to fail when they reached approximately 10 kN below their ultimate load capacity. Pieces of the coupons would start to splinter off from the sides randomly until the specimen ripped apart suddenly. Images of the specimens after failure are shown in Figure 3-8.

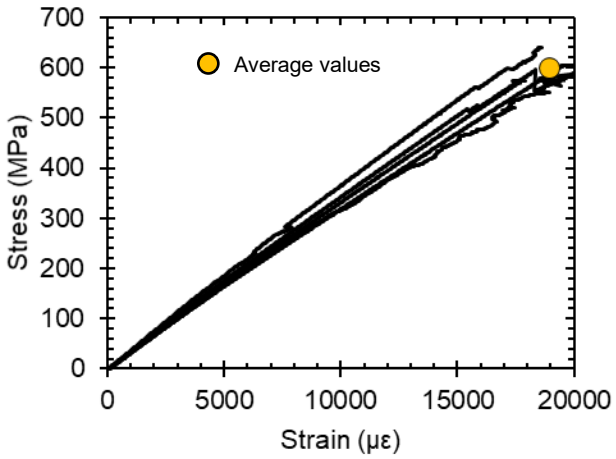

Figure 3-7 Stress vs. strain curves from tensile testing

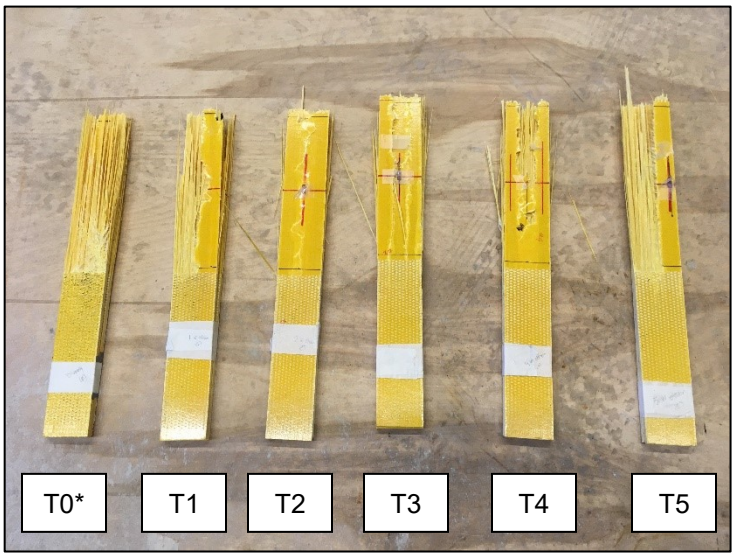

Figure 3-8 Tension specimen after failure
*T0 was a preliminary test, results not provided

3.1.2.2 FRP Compression Testing

Compression testing was carried out based on ASTM D3410: Compressive Properties of Polymer Matrix Composite Materials with Unsupported Gage Section by Shear Loading (ASTM 2016). Six coupons were cut out of one of the FRP sections and placed into a test fixture. The fixture was loaded using a 2MN Instron 5590-HVL Static Hydraulic Universal

Testing System until the coupon inside failed. The coupons were all an identical size, having a length 229 mm (9”), width 25 mm (1”), thickness 6 mm, and gauge length ranging from 19 to 22 mm. The ideal gauge length for the test was 20 mm, as it seemed to be the cut-off where Euler buckling of the specimens (an unacceptable failure mode according to ASTM D3410) could be avoided. The gauge length varied because it was difficult to place and align the specimens in the fixture without them moving around while they were being secured in place. The specimens were placed between small metal plates in the test fixture and secured by tightening bolts at the face of the fixture. The specimens were aligned with the ends of the fixture to try to avoid excessive slippage. The fixture was placed in the 2MN Instron and loaded at a rate of 2 mm per minute. A drawing of the test setup is shown in Figure 3-9, pictures of a compression specimen during testing is shown in Figure 3-10 (both below).

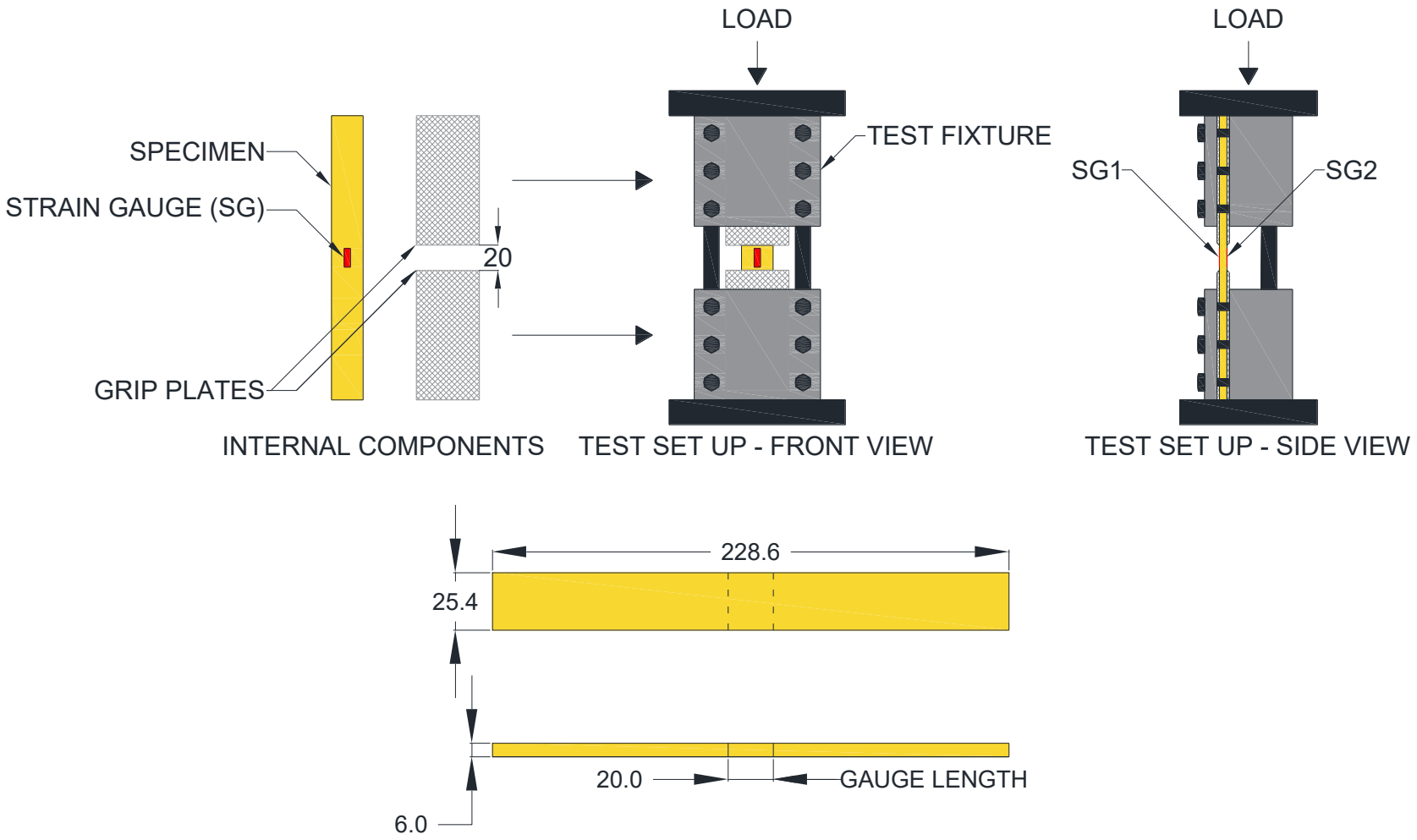

Figure 3-9 Details of compression test set up and specimen, all dimensions in mm

Figure 3-10 Compression specimen in test fixture

The results from the compressive testing can be seen in Table 3-3. These values were used for calculations and in analytical models for predicting the behaviour of the bending specimens.

Table 3-3 Compressive material properties

Specimen I.D.	P_{max} (kN)	F_{cu} (MPa)	ε_{cu} (με)	E_c (GPa)
C1	91.9	612.6	18204	33.3
C2	104.4	695.7	18301	38.0
C3	95.3	635.1	17959	35.7
C4	89.5	596.4	16441	36.0
C5	73.0	486.5	14951	37.4
C6	82.8	551.8	13130	37.6
Mean	89.4	647.8	16497	36.3
CV	12%	12%	13%	5%

The compressive modulus obtained was based on all six tests and the ultimate stress was based on only the first three (C1, C2, C3), the reasoning is explained below. Each test was consistent in that the stress-strain curves were linear, as shown Figure 3-11. Three failure

modes were observed: end-crushing, Euler buckling, and brooming along the gauge length in the middle of the coupon (BGM). Images of this BGM failure can be seen in Figure 3-12. The first coupon tested (C1) experienced failure due to end-crushing because the testing fixture was slightly off center in the 2MN Instron. ASTM deems this an unacceptable mode of failure, but the results were included in determining compressive properties of the FRP sections because the stress-strain curve was consistent with all other coupons.

Coupons C4 and C6 experienced Euler buckling, which is also an unacceptable mode of failure, but the results were used in determining the compressive modulus as again, the stress-strain curves were consistent with the coupons that did not buckle. Coupons C2, C3, and C5 had BGM as a mode of failure. Specimens C2 and C3 were ideal for determining material properties, C5 was only used to find the compressive modulus as it appeared to fail prematurely.

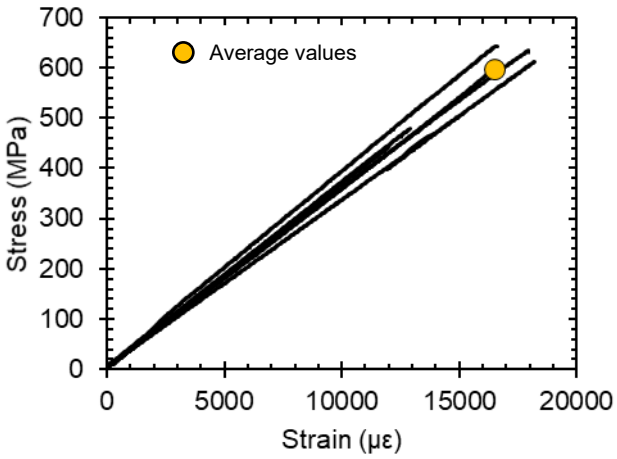

Figure 3-11 Stress vs. strain curves from compression testing

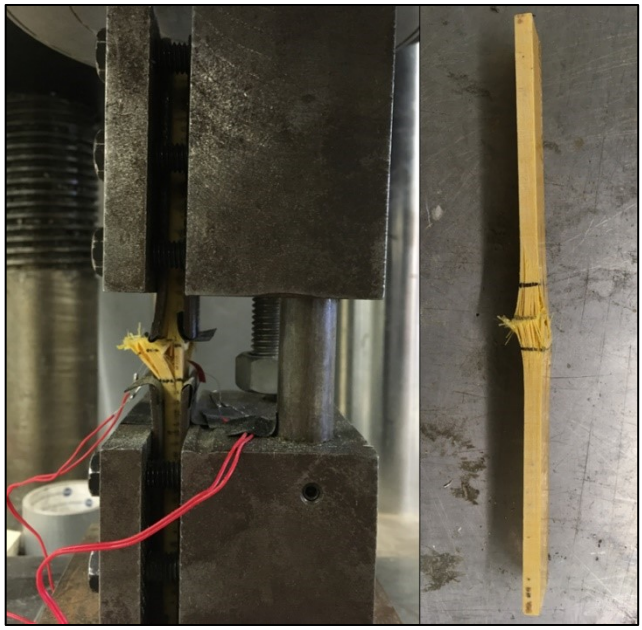

Figure 3-12 Compression specimen C2 after BGM failure

3.1.2.3 FRP Shear Testing

Testing the FRP to obtain shear properties was carried out based on ASTM D2344: Standard Test Method for Short-Beam Strength of Polymer Matrix Composite Materials and Their Laminates (ASTM 2011). Sixteen coupons were cut out from an FRP section for testing, of which thirteen were tested successfully. They were placed into a small test fixture and loaded under three-point bending. The fixture was loaded using an Instron 8501 Universal Testing Machine until the short beam specimen failed.

The specimens were small, and it was hard to cut them to identical dimensions; the average length of successfully tested specimens was 53.29 mm and the average width was 12.39 mm. Height was the same as the wall thickness of the HSS section, 6 mm. An original gauge length of 40 mm was used and eventually reduced to 32 mm (the smallest the test fixture would allow) to try to isolate an ideal failure. With the fiber orientation being unidirectional for the material, half of the specimens were cut so the fibers ran

perpendicular to the loading direction (designated “VA”) and the other half were cut so the fibers ran parallel to the loading direction (designated “VB”). The VA specimens gave shear material properties of the HSS, while the VB specimens gave crosswise tensile strength.

The specimens were placed into the three-point bending fixture and the gauge length was aligned to the outer two loading points, with the middle loading point aligned with the center of the specimen. The fixture was placed into the Instron 8501 and loaded at a rate of 1 mm per minute. A drawing of the test setup is shown in Figure 3-13, pictures of the short beam specimens can be seen in Figure 3-14.

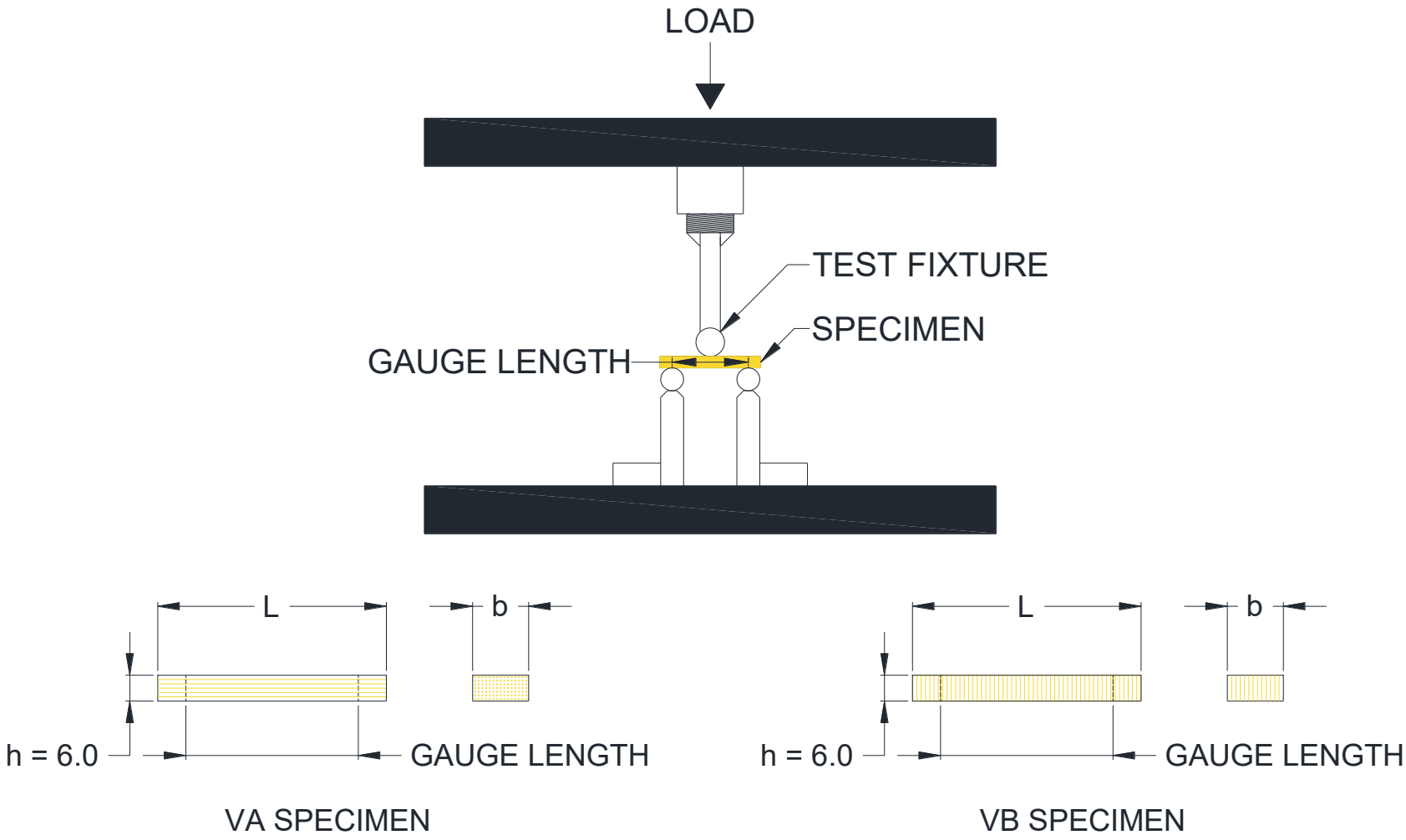

Figure 3-13 Details of shear test set up and specimens, all dimensions in mm

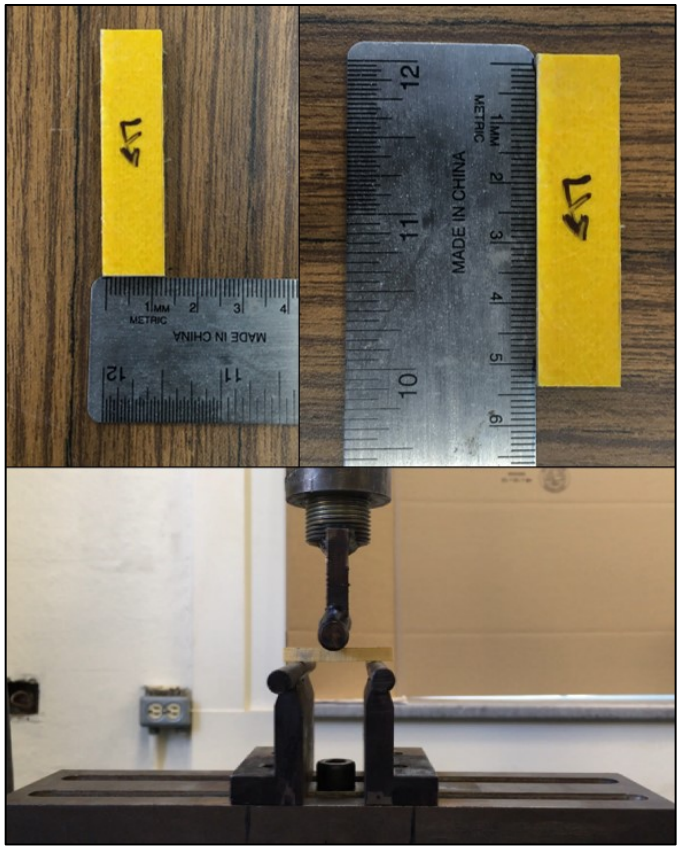

Figure 3-14 Images from short beam tests: (a) specimens used for shear testing with ruler for scale and (b) specimen in test fixture

Table 3-4 (below) shows results from the short beam tests as well as specimen dimensions. These values were used for calculations and in analytical models for predicting the behaviour of bending specimens.

Table 3-5 (below) shows test averages for maximum load and short beam strength.

Table 3-4 Material properties obtained from short beam testing

Specimen I.D.	Width (mm)	Length (mm)	Thickness (mm)	Gauge Length (mm)	$P_{max.}$ (kN)	F_{sbs} (MPa)
VA1	13.65	53.10	6	40	4.887	44.749
VA2	13.16	53.19	6	40	4.558	43.292
VA3	13.01	53.09	6	40	4.651	44.687
VA4	13.38	53.32	6	40	4.505	42.083
VA5	13.41	53.19	6	40	4.243	39.546
VA6	13.41	53.11	6	40	4.516	42.091
VB1	12.56	53.52	6	32	1.041	10.360
VB2	12.53	53.67	6	32	0.713	7.110
VB3	12.67	53.66	6	40	0.749	7.391
VB4	12.64	53.21	6	32	0.952	9.418
VB5	12.54	53.15	6	32	0.796	7.935
VB6	12.52	53.39	6	32	0.964	9.623
VB8	12.65	53.32	6	40	0.809	7.990

Table 3-5 Short beam strength test averages for shear and crosswise tension

Specimen Group	VA – Shear		VB – CW Tension	
	$P_{MAX.}$	F_{sbs}	$P_{MAX.}$	F_{sbs}
Mean	4.560	42.741	0.869	8.547
St. Dev.	0.210	1.788	0.134	1.152
C.V.	5%	4%	15%	13%

For the specimens, $P_{max.}$ was considered as the highest value of load recorded during the test. F_{sbs} was the short beam strength, obtained from Equation (3-2). This value was taken as the interlayer shear (VA specimens) or crosswise tensile (VB specimens) strength of the specimen.

$$F_{sbs} = 0.75\frac{P_{MAX.}}{bh} \quad (3\text{-}2)$$

where: F_{sbs} is the short beam strength of the specimen

$P_{max.}$ is the maximum load from test data

b is cross-section width of the specimen

h is the cross-section height of the specimen

All specimens in each group behaved the same. The VA specimens all gained load in the same manner until failure. Upon reaching the failure load, the specimens sheared in two along what looked to be the midspan of the section. There was no audible or visual indication of impending failure in the specimens, loading did slow as they neared ultimate capacity though. While VB specimens were being tested audible cracking could be heard, accompanied by hairline fractures in the loading direction in some specimens near ultimate load. Upon failure, the specimens split from the tension face toward the compression face, generally in the direction of loading. Pictures of VA and VB specimens after failure can be seen in Figure 3-15 and Figure 3-16, respectively.

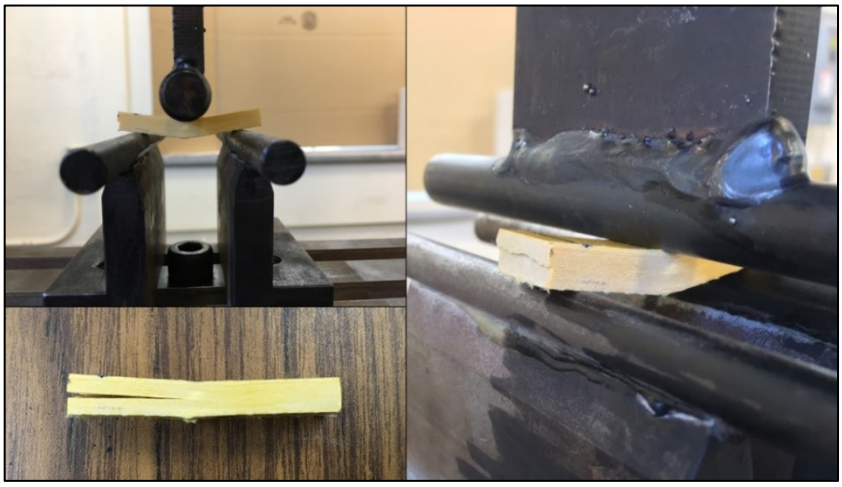

Figure 3-15 Images of a VA specimen after shear failure

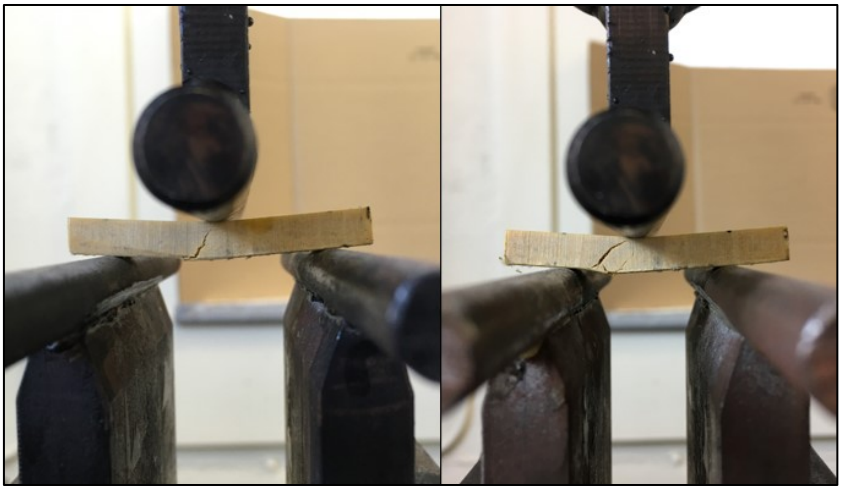

Figure 3-16 Images of VB specimens after tensile failure

3.1.2.4 Concrete Compressive Strength Testing

For each batch of concrete made for the 2 m long slab specimens tested under four-point bending, concrete cylinders were prepared to be tested for compressive strength. To manufacture the concrete, materials were combined in a wheelbarrow and mixed with a shovel. Concrete that was not placed overtop the slabs was placed in cylinders and cured for at least 28 days before being fitted with a capping agent to provide a smooth surface for testing. The cylinders were then tested under compression. Table 3-6 shows the results of these compressive tests. Naming convention will be explained in Section 3.2. Figure 3-17 shows pictures of a concrete cylinder during stages of compressive strength testing.

Table 3-6 Summary table for concrete compressive strength testing

No.	Specimen I.D.	Surface Area (mm^2)	Failure Load (lbs.)	Concrete Strength			
				f'c (MPa)	Mean f'c (MPa)	St. Dev. (MPa)	CV
1	SSA2 1-01	8271.7	307.0	37.12			
2	SSA2 1-02	8171.3	331.5	40.57	39.8	2.41	6.1%
3	SSA2 1-03	8203.4	342.6	41.77			
4	SSA2 2-01	8141.7	329.3	40.44			
5	SSA2 2-02	8217.0	364.9	44.41	40.88	3.51	8.6%
6	SSA2 2-03	8148.9	304.8	37.40			
7	SSA2 3-01	8172.1	358.2	43.83			
8	SSA2 3-02	8152.1	371.6	45.58	45.4	1.42	3.1%
9	SSA2 3-03	8205.0	382.7	46.64			
10	SSB2 1-01	8152.1	331.5	40.67			
11	SSB2 1-02	8211.4	382.7	46.60	46.1	5.21	11.3%
12	SSB2 1-03	8193.2	418.3	51.05			
13	SSB2 2-01	8155.3	331.5	40.65			
14	SSB2 2-02	8243.5	342.6	41.56	41.1	0.46	1.1%
15	SSB2 2-03	8089.8	331.5	40398			
16	SSB2 3-01	8262.1	351.1	42.44			
17	SSB2 3-02	8014.2	360.4	44.97	43.8	1.21	2.8%
18	SSB2 3-03	8120.1	356.0	43.84			

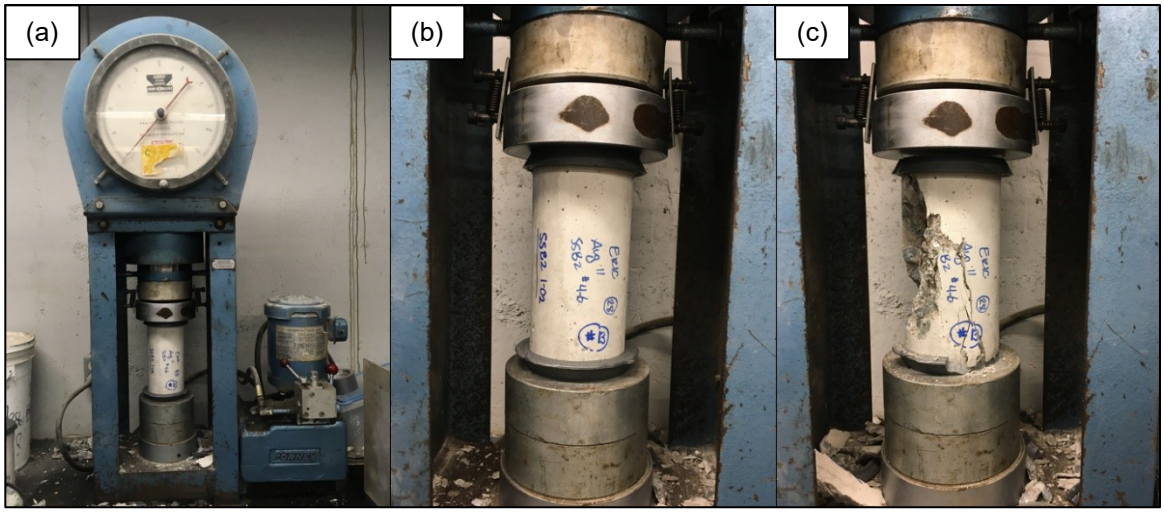

Figure 3-17 Images of a concrete cylinder being tested for concrete strength (a) cylinder in testing rig, (b) cylinder before testing and (c) cylinder after testing

3.1.3 Summary of FRP Material Testing

After comparing results of the testing conducted on the FRP material and the properties provided by the manufacturer, it was clear there was a discrepancy between the two. Table 3-7 shows a comparison of mechanical properties obtained from the manufacturer data sheet and those obtained from the material tests described above. The cause of these discrepancies is unknown, but as mentioned above it is thought that the standards used for by the manufacturer, intended for "structural plastics", did not accurately represent the mechanical properties of the FRP material for its use under the loading conditions in this study. The test results obtained independently were used for all calculations and modelling of the FRP specimens in the study.

Table 3-7 Comparison of mechanical properties from manufacturer and material tests

Mechanical Property	Data Sheet	Test Result	Variance
Tensile Strength (MPa)	230	599.4	62%
Tensile Modulus (GPa)	24.2	35.2	31%
Compressive Strength (MPa)	280	647.8	57%
Compressive Modulus (GPa)	21	36.3	42%
Interlayer Shear Strength (MPa)	25	42.7	41%

3.2 BEAM TEST MATRIX

The four-point bending tests conducted were split into three phases. The first phase had preliminary testing of hollow beams at various lengths. The second had preliminary testing of composite beam systems, in which the FRP specimens were either filled with concrete or topped with a concrete slab. The third phase was the focus of the thesis which had eighteen 2 m long slab sections tested. A brief overview of the phases with explanations of specimen designations will be discussed in this section. Specific details about the specimens and testing will be covered in the following sections.

All specimens were first categorized by type. Hollow specimens were given the designation "HS", filled "FS", and slab "SS". The filled section had an extra designation for the number of tubes adhered together and the slab sections had added designations for the bonding method used to create composite action between the FRP and concrete and slab thickness. The epoxy and aggregate bond specimens were called "SSA", bolted bond "SSB", and commercially available concrete adhesive bond "SSC". Specimen lengths were given a numerical designation of either 1, 2, or 3, corresponding to how long they were in meters. Specimens were also given a number based on the order in which they were tested. As

examples: the first 1-meter-long hollow section was called “HS1-01”, the second bolt bonded slab section with 35 mm thickness was called “SSB2-35-02”.

In the first phase of beam testing, hollow sections were subjected to four-point bending to examine behaviour under flexure. Length and shear span (spacing between loading points) were varied to get a sense of what would be most practical both for testing and simulation of a bridge deck. Table 3-8 shows the main sections tested and the varied parameters.

Table 3-8 Phase one test matrix

Specimen I.D.	Length (mm)	Shear Span (% of total length)
HS1-01	1000	33
HS1-02	1000	20
HS2-01	2000	20
HS2-02	2000	20
HS2-03	2000	20
HS3-01	3000	20

In phase two, different methods to create a composite beam with the FRP tubes and concrete were tested. The first test had three 2 m long tubes adhered together and filled with concrete. Various 1 m long sections with concrete slabs cast overtop were then tested to determine an ideal was to bond the concrete to the FRP. Four different bonding methods were used on the FRP tubes before pouring a 35 mm slab overtop. A brief description of each is mentioned in Table 3-9, (explained in more detail in Section 3.3). Table 3-9 also shows length of specimens tested with designations.

Table 3-9 Phase two test matrix

Specimen I.D.	Length (mm)	Surface Treatment (slab sections only)
FS2x3-01	2000	N/A
SSC1-01	1000	Concrete bonding adhesive
SSA1-01	1000	Aggregate set in epoxy
SSA1-02	1000	
SSB1-01	1000	Bolted – with steel anchor bar
SSB1-02	1000	Bolted – epoxy coated bolts, no anchor bar

Phase three contained the full-scale beam tests, the main portion of experimental testing for this thesis. 2 m long FRP sections had top surfaces treated with either aggregate set in epoxy or epoxy coated bolts and had slabs of various thicknesses poured overtop. Table 3-10 shows the variation in slab thickness and surface treatment between specimens tested in phase three.

Table 3-10 Phase three test matrix

Group I.D.	Slab Thickness (mm)	Surface Treatment
SSA2-35	35	Aggregate set in epoxy
SSA2-55	55	
SSA2-75	75	
SSB2-35	35	Epoxy coated bolts
SSB2-55	55	
SSB2-75	75	

3.3 SPECIMEN FABRICATION

As mentioned above, three fabrication methods were used to create bridge decking systems:

- Cutting hollow FRP specimens to desired lengths and testing without any other modifications.
- Filling the specimens with concrete before testing.
- Applying a bonding agent to the top of the FRP specimens and pouring a concrete slab overtop before testing.

3.3.1 Hollow Sections

Unaltered, individual FRP sections of varying length were tested to examine behaviour when subjected to four-point bending. The tubes were cut into lengths of either 1000, 2000, or 3000 mm.

3.3.2 Filled Section

Three hollow sections, 2000 mm long, were adhered together using an epoxy adhesive (MasterEmaco ADH 1420). This set of tubes was stood upright, and concrete was poured into them to create a composite section. The concrete had compressive strength of approximately 40 MPa.

3.3.3 Slab Sections

3.3.3.1 Preliminary Tests

Hollow sections were cut into 1000 mm lengths for preliminary testing to gauge the effectiveness of bond enhancing methods on the concrete-FRP interface. The bond enhancers and fabrication methods used to create the specimens are listed below.

- Commercially available concrete adhesive:

The FRP section was placed into a form and the top face was coated with a concrete bonding adhesive (QUIKRETE® Concrete Bonding Adhesive). The adhesive was allowed to dry almost completely, per manufacturer recommendations. A 35 mm thick concrete slab was then poured overtop. The concrete was cured for seven days and had compressive strength of approximately 30 MPa.

- Aggregate set in epoxy:

  The top face of the FRP section was coated with a two-part epoxy (West Systems 105 and 206). Aggregate that had passed through a 9.51 mm (1/4") sieve and was retained on a 6.35 mm (3/8") sieve was placed on top of this epoxy coat that was allowed to dry completely (Figure 3-18). The amount of aggregate throughout the preliminary and full-scale tests was approximately 7550 g/m^2. The section was placed in a form and a 35 mm slab was poured overtop. The concrete was cured for seven days and had a compressive strength of approximately 30 MPa.

Figure 3-18 Aggregate set in epoxy on top face of FRP section

- Bolted connectors

  The FRP section had ten bolts drilled into the top face at 100 mm intervals (Figure 3-19a). It was designed to mimic shear studs in a traditional steel-concrete

composite section. Two different methods were used to help connect the bolts to the FRP. First, a thin hollow steel section was placed inside the tube to anchor the bolts and keep them upright (Figure 3-19b). Second, holes were tapped in the FRP where the bolts would go, and an epoxy resin (West Systems 105 and 206) was applied to the holes and bolts before they were inserted. For both methods, the sections were then placed in a form and a 35 mm slab was poured overtop. The concrete was cured for seven days and had compressive strength of approximately 30 MPa.

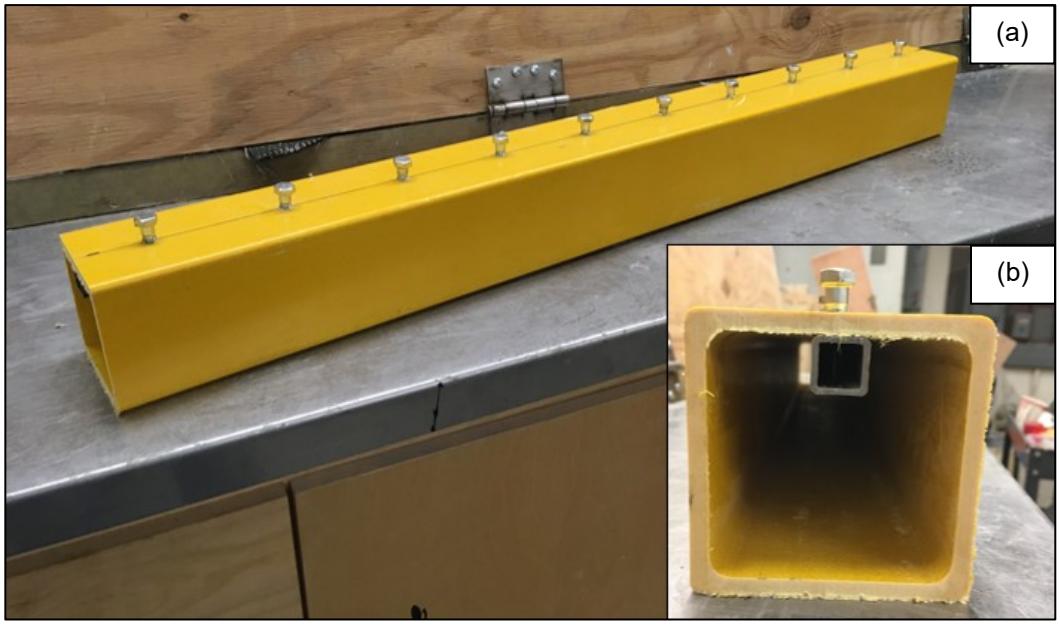

Figure 3-19 Specimen with bolted connectors before slab was cast overtop

3.3.3.2 Full Scale Tests

The bonding methods of using epoxy set in aggregate and epoxy coated bolts were found to provide the most effective bond between the concrete and FRP and were used for the 2 m long specimens in full scale tests. Discussion regarding why these methods were chosen is included in Section 3.5. For the epoxy/aggregate method, the epoxy used was changed

to a more paste-like adhesive (Sikadur®-30 Part A and 20B) for more efficient fabrication. The size and amount of aggregate remained the same. The bolts were drilled so that they extended half of the way into the slab from the FRP face.

After the surfaces had been treated with the bonding agents the specimens were placed in forms and slabs of three different thicknesses, 35 mm, 55 mm, and 75 mm, were poured overtop. These thicknesses were chosen to simulate three different conditions of neutral axis location, one where the neutral axis was in the FRP web (35 mm), one where it was close to the concrete and FRP interface (55 mm), and one where it was in the slab (75 mm). The thicknesses chosen also allowed for ease of fabrication as they were not overly large and would not become too heavy to transport. Figure 3-20 shows pictures of the fabrication stages of a bolt bonded specimen.

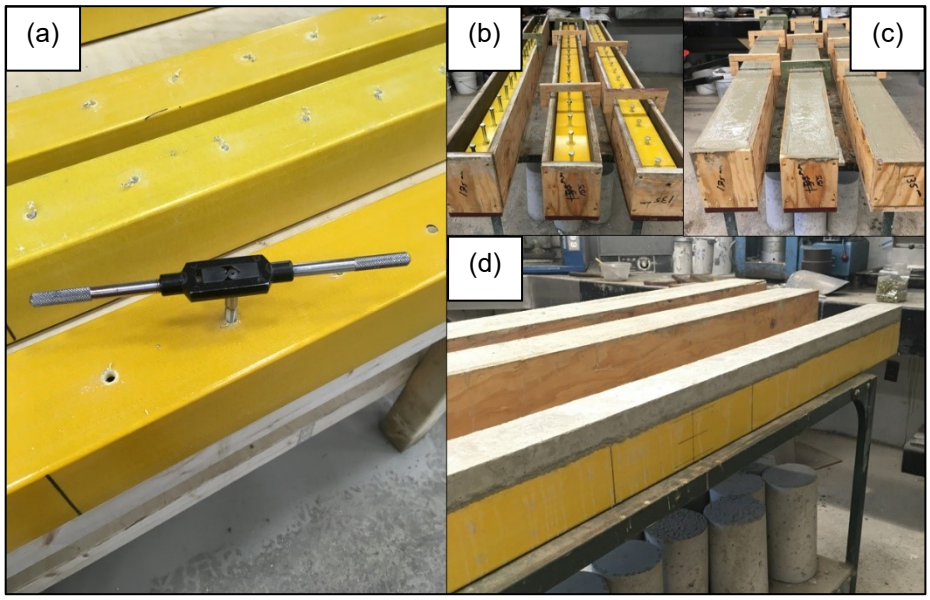

Figure 3-20 Fabrication stages of bolt bonded slab specimen: (a) tapping drilled holes, (b) specimens in formwork, (c) specimens after slabs were poured and (d) specimens after concrete cured for 24 hours

The concrete was made by combining materials in a wheelbarrow and mixing with a shovel until combined. The concrete mix was poured into the formwork over the slabs and tamped down in stages. The remaining concrete was poured into cylinders, used for compressive strength testing (see Section 3.1.2.4). Concrete material amounts are listed in Table 3-11. The amount of concrete used for each batch of three slabs was 0.045 m^3, which filled all forms completely and left enough to make three cylinders (100 mm in diameter, 200 mm in height).

Table 3-11 Material quantities used to make concrete for 2 m long slab specimens

Material	Quantity (for 1 m^3)
Water (kg)	200.000
Cementitious Material (kg)	395.238
Fine Aggregate (kg)	574.553
Coarse Aggregate (kg)	888.889
Water/Cement Ratio	0.51

3.4 INSTRUMENTATION AND TEST SET-UP

This section briefly explains the set-up for the four-point bending tests, the instrumentation used to record data, and includes images and detailed drawings of different types of specimens before testing.

3.4.1 Instrumentation

3.4.1.1 Hollow Sections

The instrumentation used for the four-point bending tests on the hollow sections is listed below. A picture of the test set-up can be seen in Figure 3-21.

- String potentiometer – used to measure deflection, attached to the section by a string at midspan.
- Strain gauges – used to measure tensile and compressive strain, adhered to the tensile and compressive faces of the specimen at midspan.

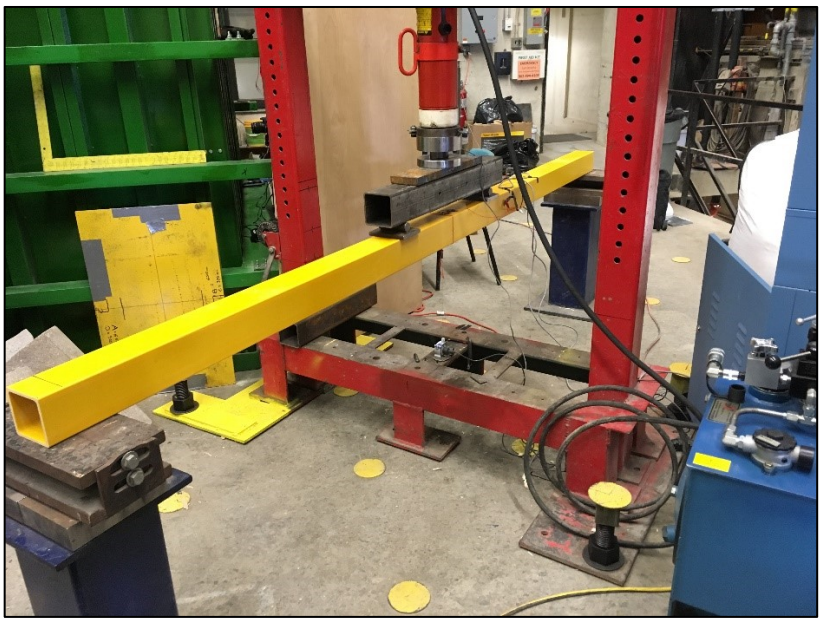

Figure 3-21 Picture of four-point bending test set-up for hollow specimen HS3-01

3.4.1.2 Filled Section

The instrumentation used for the four-point bending tests on the filled section is listed below. A picture of the test set-up can be seen in Figure 3-22.

- String potentiometer – used to measure deflection, attached to the section by a string at midspan directly under the middle beam.
- Strain gauges – used to measure tensile and compressive strain, adhered to the tensile and compressive faces of the middle FRP beam at midspan.

Figure 3-22 Pictures of four-point bending test set-up for the filled specimen FS2x3-01

3.4.1.3 Slab Sections

The instrumentation used for the four-point bending tests on the slab sections is listed below. A picture of the test set-up can be seen in Figure 3-23.

- String potentiometer – used to measure deflection, attached to the section by a string at midspan directly under the middle beam.
- Strain gauges – used to measure tensile and compressive strain, one adhered to the tensile face at midspan and another adhered to an exterior side wall at midspan, 10 mm from the compression face (this was done as opposed to placing the gauge directly under the concrete). Strain gauges were not used for preliminary slab section testing.

- Linear potentiometers – used to measure concrete slippage, attached by a small jig to each end of the FRP beam, placed so the reading would be taken in the middle of the slab. Linear potentiometers were not used for the preliminary slab section testing.

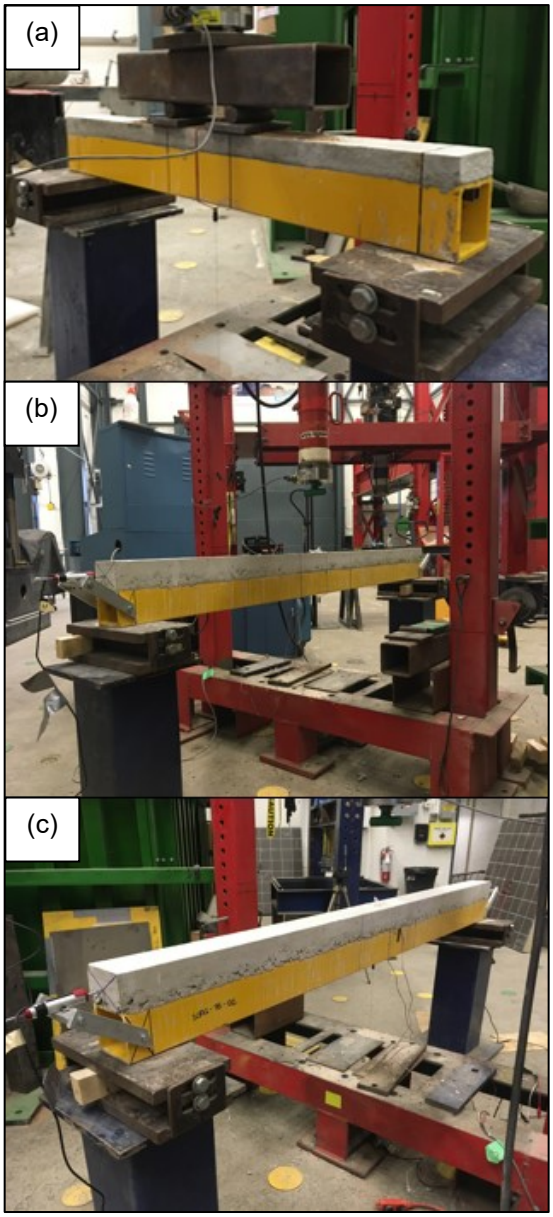

Figure 3-23 Pictures of four-point bending test set-up for the slab specimens: (a) preliminary slab specimen SSB1-35-01, (b) and (c) full-scale slab specimen SSA2-75-02

3.4.2 Beam Set-Up

For the four-point bending tests, specimens were set onto roller-pin supports. An overhang of 50 mm was left on each end, making the effective length of each specimen 100 mm less than the actual length (for example, a 2000 mm long specimen had an effective length of 1900 mm). The specimens were loaded statically through a steel hollow structural section until failure was deemed to have occurred, explained in Section 3.5. The steel section was placed overtop steel cylinders and bearing plates to create point loads. Detailed drawings of the test set-up and instrumentation are shown in Figure 3-24 and Figure 3-25 (below).

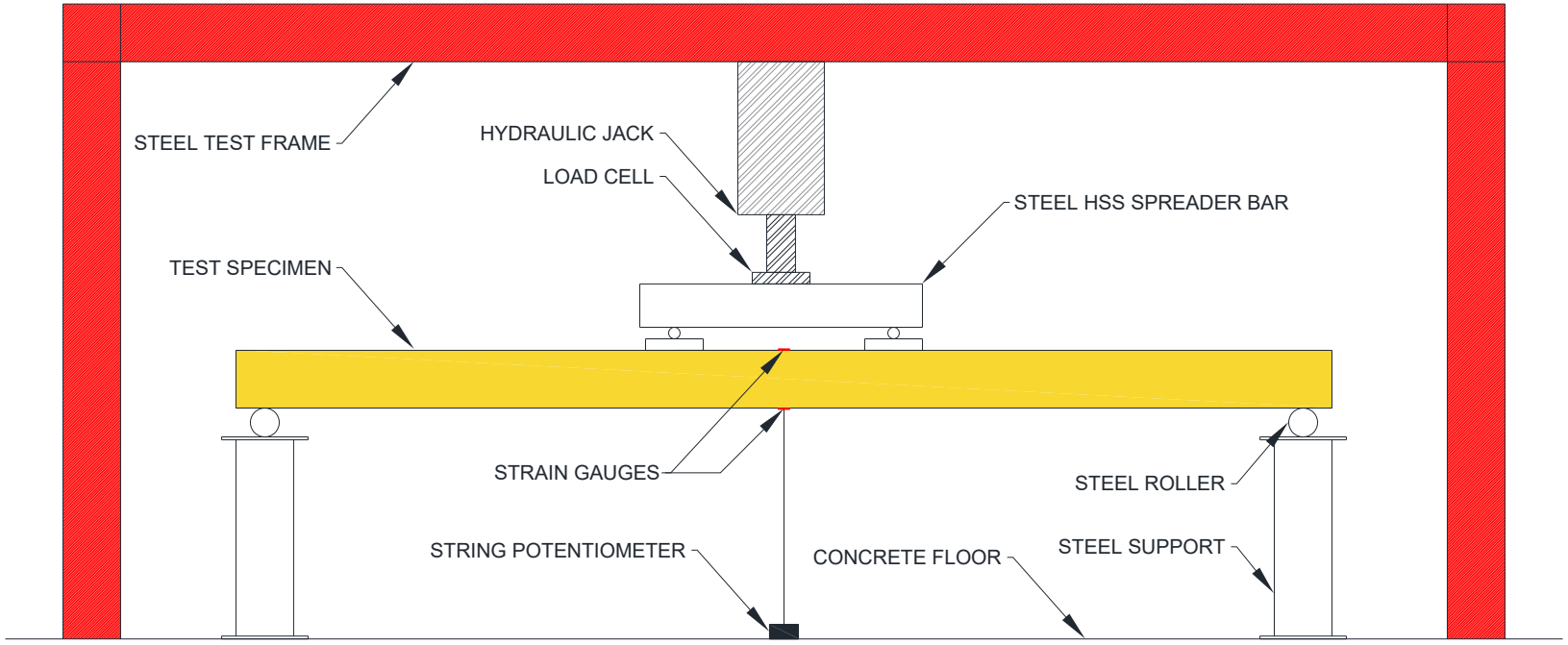

Figure 3-24 Details of four-point bending test set up for hollow and filled specimens

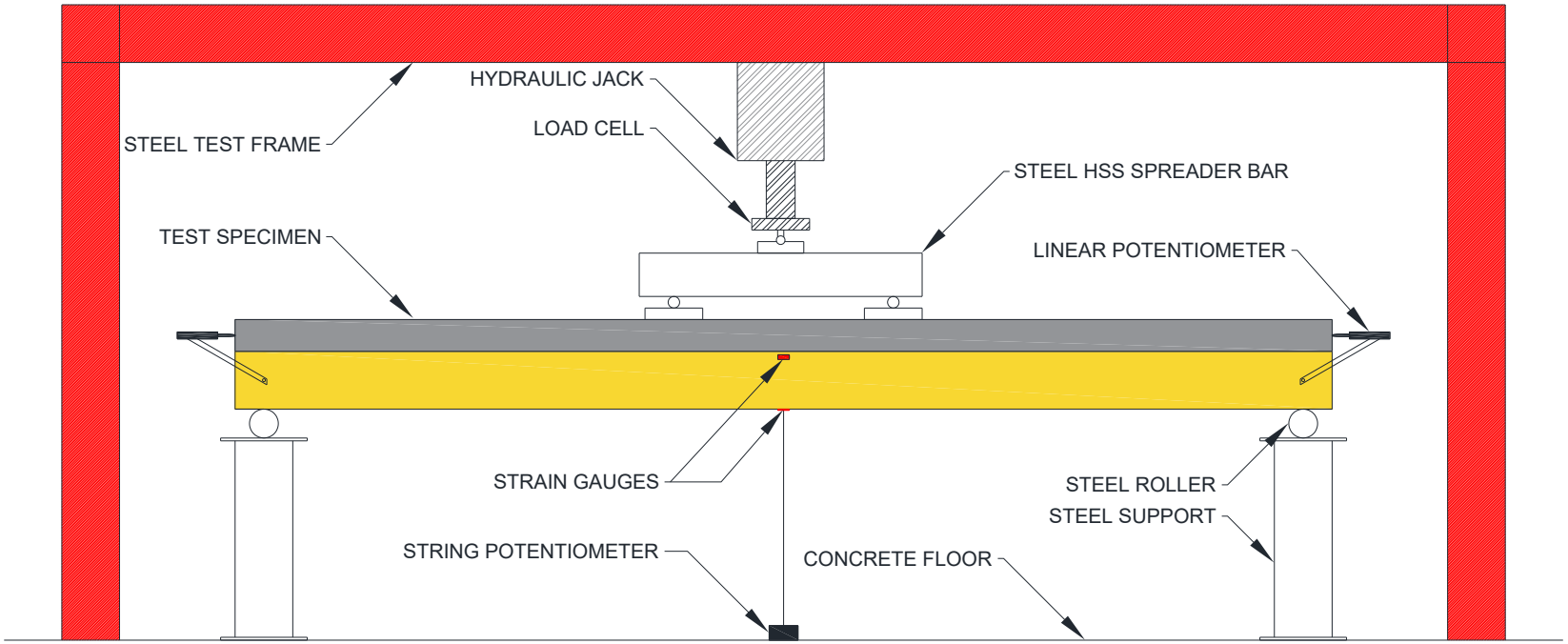

Figure 3-25 Details of four-point bending test set-up for full-scale slab sections

3.5 TEST RESULTS AND DISCUSSION

The following section will outline the results of the four-point bending tests conducted. Load-deflection behaviour and failure modes will be analyzed for all beams; load-strain behaviour will be examined for applicable sections as well. In addition, the effect of slab thickness and bonding method on stiffness, slippage and ultimate load capacity will be discussed. Test results are shown in tables Table 3-12,

Table 3-13, Table 3-14, and Table 3-15).

Table 3-12 Summary table of test results for hollow and filled specimens

Specimen I.D.	Peak Load (kN)	Moment at Peak (kN-m)	Deflection at Peak (mm)	Maximum Strain (με)	
				Compressive	Tensile
HS1-01	87.8	15.8	15.5	N/A	N/A
HS1-02	91.9	16.5	17.4	-5673*	7273
HS2-01	64.5	24.5	89.7	-10209	11951
HS2-02	62.5	23.8	85.5	-7999	10365
HS2-03	63.0	23.9	85.1	-9261	11123
HS1-03	38.8	22.5	177.5	-9746*	10734
FS2x3-01	69.2	26.3	79.9	-9225	11673*

All failure modes were the same for these tests, discussed in Section 3.5.1. A "*" indicates the strain gauge recording that data failed during testing, therefore the strain value was interpolated from the linear portion of the data set.

Table 3-13 Summary table of test results for 1 m long slab specimens

Specimen I.D.	Peak Load (kN)	Moment at Peak (kN-m)	Deflection at Peak (mm)	Failure Mode
SSA1-35-02	86.3	15.5	13.8	Crushing/FRP – Simultaneous
SSB1-35-01	105.6	19.0	21.9	Cracking/FRP – Simultaneous
SSB1-35-02	84.4	15.2	17.4	
SSC1-35-01	96.8	17.4	16.1	Bond/FRP – Non-simultaneous

Strain was not recorded for these tests, as they were designed to assess bond effectiveness.

Table 3-14 Summary table of results for 2 m long epoxy and aggregate bonded slab specimens

Specimen I.D.	Peak Load (kN)	Moment at Peak (kN-m)	Deflection at Peak (mm)	Strain at Peak (με)		Curvature at Peak (1/m)	Slip at Peak (mm)		Failure Mode
				"Compressive"	Tensile		End 1	End 2	
SSA2-35-01	44.0	16.7	21.9	181	4382	0.050	0.02	0.03	Bond
SSA2-35-02	43.2	16.4	25.9	-387	5007	0.060	0.19	0.11	Crushing
SSA2-35-03	46.4	17.6	27.2	-1048	5159	0.069	0.08	0.09	Crushing
SSA2-55-01	48.2	18.3	20.1	576	4319	0.054	0.10	0.02	Bond
SSA2-55-02	44.3	16.8	18.5	344	3943	0.048	0.07	0.11	Bond
SSA2-55-03	58.1	22.1	27.6	466	5871	0.068	0.05	0.01	Crushing
SSA2-75-01	48.5	18.4	15.9	878	3527	0.049	0.05	0.04	Bond
SSA2-75-02	53.6	20.4	18.7	832	4023	0.054	0.01	0.04	Bond
SSA2-75-03	58.9	22.4	19.5	978	4299	0.059	0.01	0.11	Bond

Note that "compressive" refers to the fact that the strain gauge recording this data was affixed to the side wall of the FRP beam, 10 mm from the compression face.

Table 3-15 Summary table of results for 2 m long bolt bonded slab specimens

Specimen I.D.	Peak Load (kN)	Moment at Peak (kN-m)	Deflection at Peak (mm)	Strain at Peak (με)		Curvature at Peak (1/m)	Slip at Peak (mm)		Failure Mode
				"Compressive"	Tensile		End 1	End 2	
SSB2-35-01	16.9	6.4	17.8	-474	3157	0.040	0.54	0.68	Tension – Concrete
SSB2-35-02	35.9	13.6	23.4	-667	4066	0.053	0.60	0.83	
SSB2-35-03	31.8	12.1	20.5	-392	3491	0.043	0.58	0.60	
SSB2-55-01	25.1	9.5	23.4	-195	4033	0.047	0.75	1.06	
SSB2-55-02	43.0	16.3	23.9	-239	4216	0.049	1.09	0.91	
SSB2-55-03	45.6	17.3	24.9	-179	4316	0.050	0.80	0.76	
SSB2-75-01	29.5	11.2	22.2	-33	3884	0.044	1.07	1.30	
SSB2-75-02	49.8	18.9	22.2	-65	3892	0.044	1.25	1.19	
SSB2-75-03	53.3	20.3	22.9	-102	4243	0.048	1.64	1.21	

Note that "compressive" refers to the fact that the strain gauge recording this data was affixed to the side wall of the FRP beam, 10 mm from the compression face.

The first four-point bending tests were conducted on individual hollow specimens of different lengths, as a part of phase one of the test matrix. The results of this round of testing showed that the hollow specimens were too flexible to be considered practical for bridge decking use. While there are technically no deformation limits on concrete decks in the Canadian Highway Bridge Design Code, the FRP specimens of all lengths experienced visible deflection at lower loads than the greatest wheel loads used to simulate traffic live loading by the bridge code (CSA Group 2019). For this reason, it was decided that the FRP beams needed to be stiffened. To do this, concrete was added to the specimens to create a stiffer composite material. An increase in stiffness when compared to hollow sections became the main criterion in gauging whether the composite beams tested could be viable for bridge decking use.

The two methods used to create FRP-concrete composite beams, filling the hollow FRP sections and casting a slab overtop of the FRP, were tested in phase two of the test matrix. After determining that the filled sections were not suitable for further testing (discussed below), creating an effective bond between concrete and FRP became the focus of the phase. Bond effectiveness was assessed based on two criteria: the composite beam being stiffer than the hollow and the composite beam having more load capacity than the hollow. This will also be discussed in more detail below, but from examining load-deflection results it was observed that the aggregate set in epoxy and both bolted bonding methods increased initial stiffness of the composite beam when compared to a hollow specimen of the same length. The bolt bonding method with the steel anchor bar also increased ultimate load capacity compared to hollow specimens. It was concluded that the aggregate set in epoxy and epoxy coated bolting method with no anchor bar would be used to construct specimens

for the third phase of the test matrix. The bolt bonded method did not make use of the anchor bar as it was much easier to fabricate specimens without it.

The length of specimens used in phase three, 2 m, was chosen for two main reasons. First, testing from phase one showed that the 2 m long specimens had the highest moment capacity of the three lengths tested (discussed below). Second, a length of 2 m seemed to be the most practical considering the composite beams were being tested to be used in bridge decking systems. A rough study was conducted to determine the average girder spacing for highway bridges around the Halifax Regional Municipality in Nova Scotia, Canada. The results of this study concluded that the average girder spacing was approximately 2 m.

3.5.1 Failure Modes

The first tests completed were on hollow specimens. All specimens behaved the same, regardless of length, they deflected constantly under sustained load until failure. Near the failure loads for each, loading would slow slightly at which point some cracking could be heard shortly before a loud, somewhat violent failure. Upon examining the specimens, they seemed to fail in a shearing manner that originated at the corners of the tubes. For the 2 m and 3 m hollow specimens, the top face would warp inward or outward (the direction was arbitrary) after becoming detached from the corners. The 1 m specimens differed from this, the top face would stay intact while the shearing from the corners would move laterally into the side walls, causing them to crush. Pictures of hollow specimens of different lengths after failure are shown in Figure 3-26.

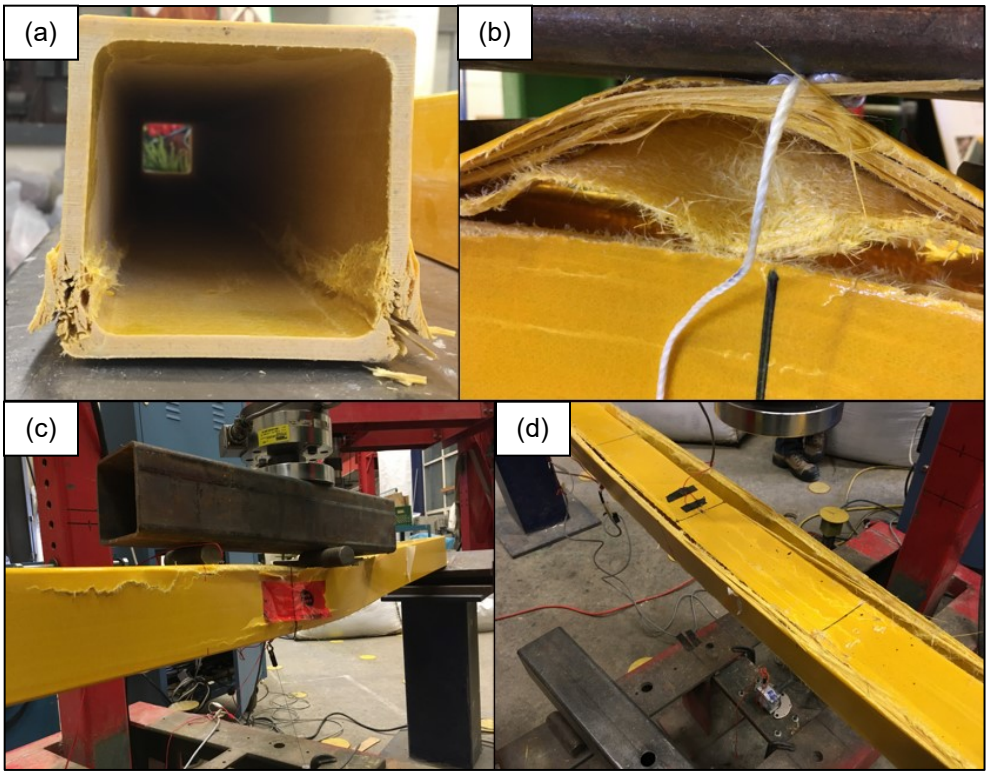

Figure 3-26 Pictures of hollow specimens after failure under four-point bending: (a) HS1-01, (b) HS2-02, (c) and (d) HS3-01

The filled section essentially behaved the same way as the hollow sections. While it was being loaded audible crackling noises could be heard, assumed to be the glue holding the tubes together and concrete cracking within the section. When the specimens reached peak load one of the outer beams failed in the shearing manner seen in the hollow tubes. When the FRP failed the concrete inside was forced out violently causing the system to skew the other way. With load still being applied the other two tubes were shot in the opposite direction. It was unclear if the FRP in the other tubes had failed before this, or if they ended up breaking due to impacting the test frame at a high speed. After examining the pieces from the test, it could be seen that the concrete was also broken into several pieces. Again, it was unclear if this had occurred while in the tubes or because of the impact they were subjected to. The violent and dangerous failure (along with the fact that stiffness and load

capacity were similar to the hollow specimens) was why only one test was conducted on a filled section. Pictures of the filled specimen after failure are shown in Figure 3-27

Figure 3-27 Pictures of the filled specimen FS2x3-01 after failure under four-point bending

Failure modes and load capacities of the preliminary 1 m slab specimens were used to determine which bonding methods would be used for the full-scale 2 m slab section tests. The first bonding method tested was applying a commercially available concrete adhesive to the FRP before casting concrete overtop. The adhesive was unsuccessful in keeping the specimen composite, as the concrete debonded from the FRP at the end faces early in the test. The concrete eventually crushed, and the specimen was loaded until the FRP failed. Peak load and failure mode was consistent with the hollow tests. The second bonding method tested had the top face of the FRP covered with aggregate set in epoxy before pouring the concrete slab overtop. The specimen failed due to concrete crushing. This happened at a high enough load that the FRP almost simultaneously failed after the concrete

was no longer taking any of the load, only transferring it directly to the FRP. This method was considered successful in creating composite action and it was chosen to be used for the full-scale tests. The next bonding method tested was to drill bolts into the top face of the FRP, anchoring them with a steel bar, and pouring concrete overtop. The result of this test was similar to the epoxy and aggregate bonding method, although the failure mode was slightly different. A small crack formed in the concrete, visible at the end face at around 75% of its ultimate load. As the load increased so did the crack, when it had propagated through the entire slab, the concrete stopped taking load like the epoxy and aggregate specimen and transferred it all into the FRP which failed immediately. This specimen had the highest peak load of all the 1 m slab sections, almost certainly due to the steel anchor bar. The last specimen also used the bolting method to bond the concrete to the FRP, but it did not have the steel anchor bar. It behaved the same as the first bolted specimen, with the FRP failing immediately after a crack had propagated through the slab. The only difference between this specimen and the specimen with the anchor bar was that the specimen with the bar had a higher peak load. Both bolted bonding methods were considered effective, but the one without anchor bar was chosen for the 2 m specimens. Although it had a lower peak load, it was much easier and less time consuming to fabricate. Pictures of the preliminary slab specimens after failure are shown in Figure 3-28.

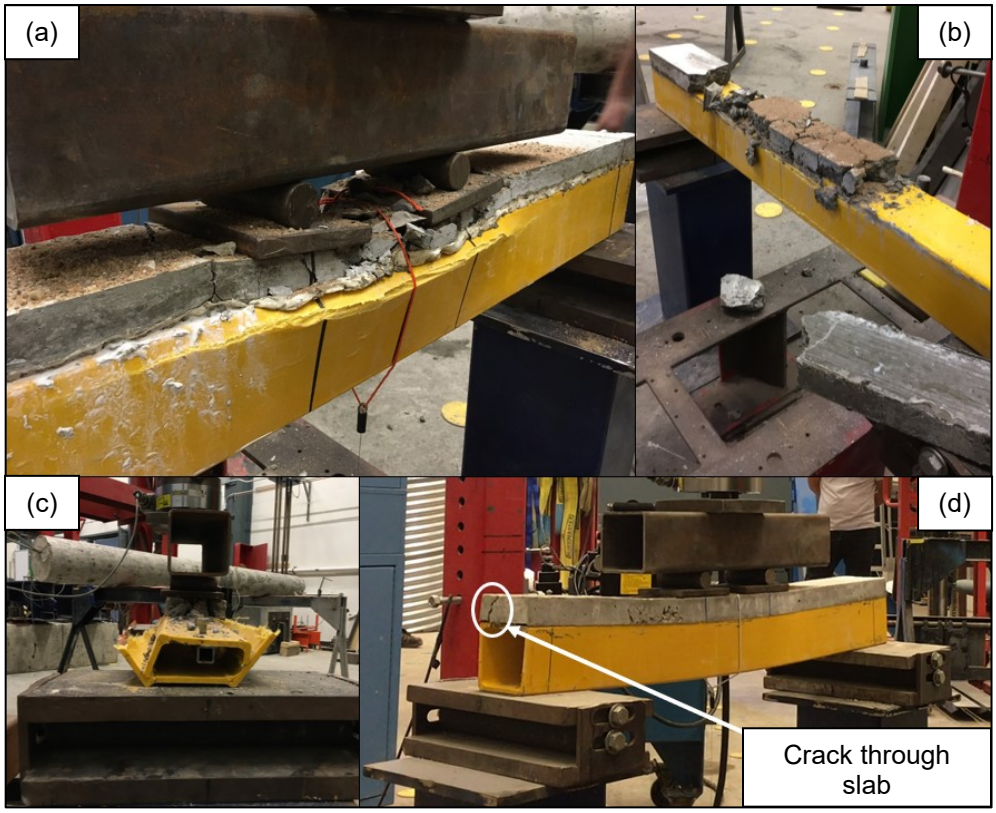

Figure 3-28 Pictures of 1 m long slab specimens after failure due to four-point bending: (a) SSA1-35-02, (b) SSC1-35-01, (c) SSB1-35-01 and (d) SSB1-35-02 (just before FRP failure)

The 2 m slab specimens with epoxy and aggregate bond failed in two different manners. Two of each of the 35 mm and 55 mm failed due to concrete crushing, while the rest exhibited bond failure. Failure was considered to be the point at which the specimen lost composite action, when the concrete stopped taking load and instead only transferred it into the FRP. It was assumed the thicker slabs would be more likely to have bond failure while the thinner ones would crush, and while the 75 mm specimens all failed due to debonding, there was no clear indication as to why the other specimens failed in a certain way before or during the tests. Examining load-deflection results showed that the 35 mm slab specimen that failed due to bond was slightly stiffer than the ones that crushed. There were no differences in stiffness between the 55 mm specimen that failed due to crushing

compared to the ones that failed due to debonding. Pictures of SSA sections after failure due to debonding and crushing are shown in Figure 3-29 and Figure 3-30, respectively.

Figure 3-29 Pictures of SSA2-75-02 after concrete bond failure due to four-point bending

Figure 3-30 Pictures of SSA2-55-03 after concrete crushing failure due to four-point bending

The 2 m long bolted bond specimens all failed in the same manner. Upon reaching peak load the concrete slabs split laterally along the center of the beam, following the pattern of the bolts. This split, due to tension, originated from the loading points and extended to the end faces. Like the epoxy and aggregate bonded specimens, failure was also considered to

be at the point where composite action ceased. Pictures of an SSB section after failure is shown in Figure 3-31.

Figure 3-31 Pictures of SSB2-55-01 after concrete tensile failure due to four-point bending

Examining the data collected from the linear potentiometers, it was seen that these specimens experienced noticeable outward slippage. While slippage was occurring, the bolts were also rotating inward due to the deflection the beam was experiencing. These opposite motions were what caused the concrete to split. This is also why the 1 m and 2 m bolted specimens failed in different manners. There seemed to be a certain breakpoint for the 2 m specimens at which the rotation caused by deflection was too much for the slab to handle, whereas the 1 m specimens did not deflect and in turn rotate enough for this tension split to occur. Compared to the bolted specimens, the epoxy and aggregate bonded

specimens had negligible amounts of slip. Slippage was plotted against load for the 2 m long bolt bonded specimens and is shown in Figure 3-32, below. It is noticeable in these plots that the load for one data set on each is significantly lower than the other two. This will be addressed in the following section.

(a)

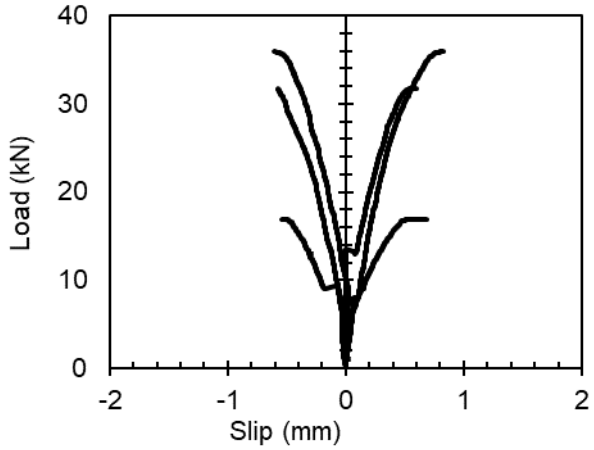

(b)

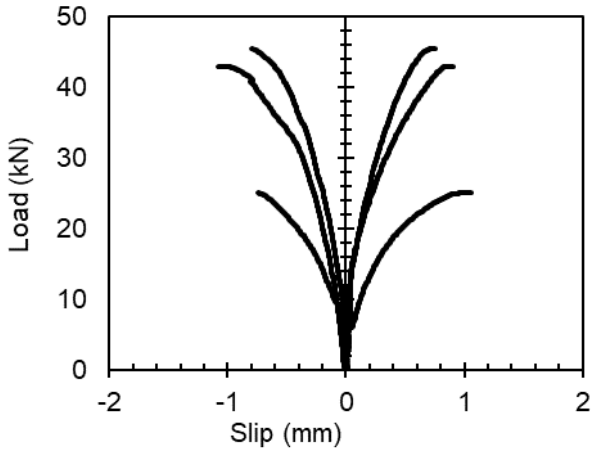

(c)

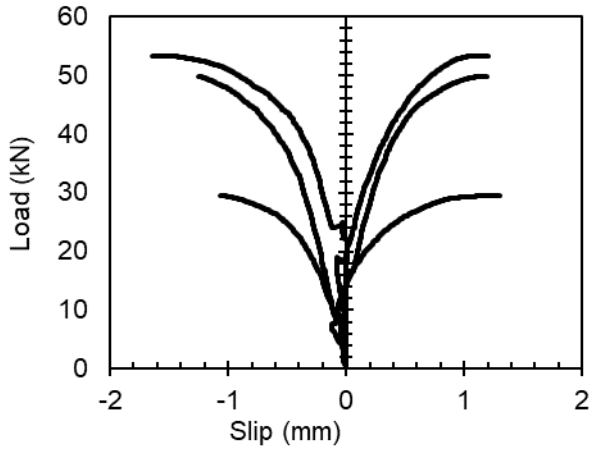

Figure 3-32 Load-slip plots for 2 m long bolt bonded slab specimens: (a) SSB2-35, (b) SSB2-55 and (c) SSB2-75

3.5.2 Load-Deflection Behaviour

Load-deflection response of the specimens was used to assess stiffness and ultimate load capacity, stiffness being the main metric used to determining if the systems tested could be viable for bridge decking use. Data for the load on specimens was recorded by a load cell. Deflection was measured by a string potentiometer positioned directly underneath the midspan location of all specimens.

The preliminary hollow sections tested all behaved similarly. As expected, stiffness and load capacity directly correlated to the length of the specimen. The 1 m long specimens were the stiffest and had the highest peak loads, while the 3 m long specimen tested was the least stiff and had the lowest peak load. The 2 m specimens had peak load and stiffnesses between those of the 1 and 3 m specimens. Load-deflection response followed a generally linear trend for all specimens. Any non-linear behaviour was attributed to strain gauges failing prematurely. Average results from the hollow tests of each length are shown in Figure 3-33.

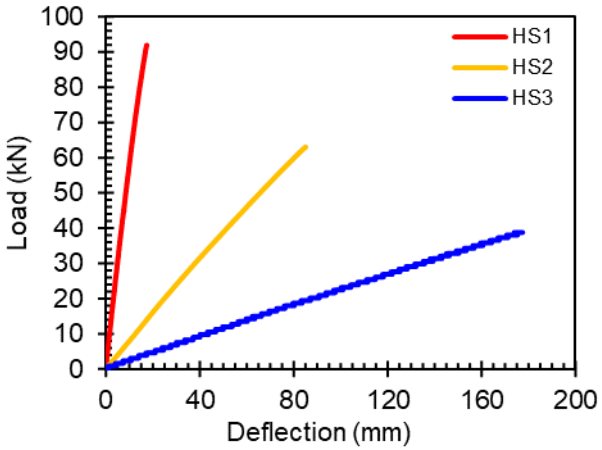

Figure 3-33 Load-deflection plot for hollow specimens

The filled specimen had a similar load-deflection response to the hollow beams. It had a higher initial stiffness that levelled out to closer match that of the hollow specimens later in the test. This was likely due to the concrete cracking within the tubes during the test and becoming less effective in stiffening the beams. The specimen had a non-linear load-deflection response due to the presence of concrete. Overall, the ultimate load was slightly higher, and the maximum deflection was slightly lower than the average of the hollow sections. When the catastrophic nature of failure was weighed against the small gain in ultimate load and stiffness observed, it was deemed that it was no longer beneficial to test specimens filled with concrete. The load deflection plot, modified to reflect one filled beam, can be seen in Figure 3-34. The load-deflection curve for hollow section HS2-03 was included in this plot for visual comparison with hollow specimens of the same length.

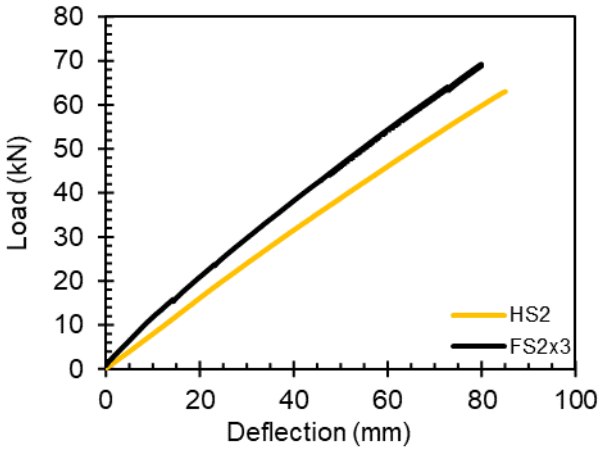

Figure 3-34 Load-deflection plot for filled specimen with hollow specimen as reference

The 1 m slab specimens offered a more promising outlook on improving the stiffness of the hollow beams. All 1 m slab specimens tested had a higher initial stiffness than the 1 m hollow sections, as shown in Figure 3-35. For all slab specimens though, there was a point

at which the initial stiffness “gave out” and reverted to a stiffness more like the hollow specimens. The concrete adhesive specimen had this happen the earliest when the bond between the concrete and FRP failed. The stiffness of this specimen ended up being greater than that of the hollow and bolted sections because the debonded, but intact, concrete still provided some additional stiffness to the specimen. The epoxy and aggregate bonded specimen had its initial stiffness drop at the latest point comparatively, but it reverted to a stiffness almost identical to that of the concrete adhesive specimen. The two bolted specimens behaved almost identically, they both had stiffness drops around the same load, the stiffnesses before and after the drop were almost identical as well. The only major difference between the two was that the specimen with the anchor bar, SSB1-01, had a higher ultimate load compared to all the 1 m slab and hollow sections. This was attributed to the presence of steel in the specimen. Figure 3-35 shows load-deflection plots for the 1 m slab specimens, with hollow section HS1-02 included for reference.

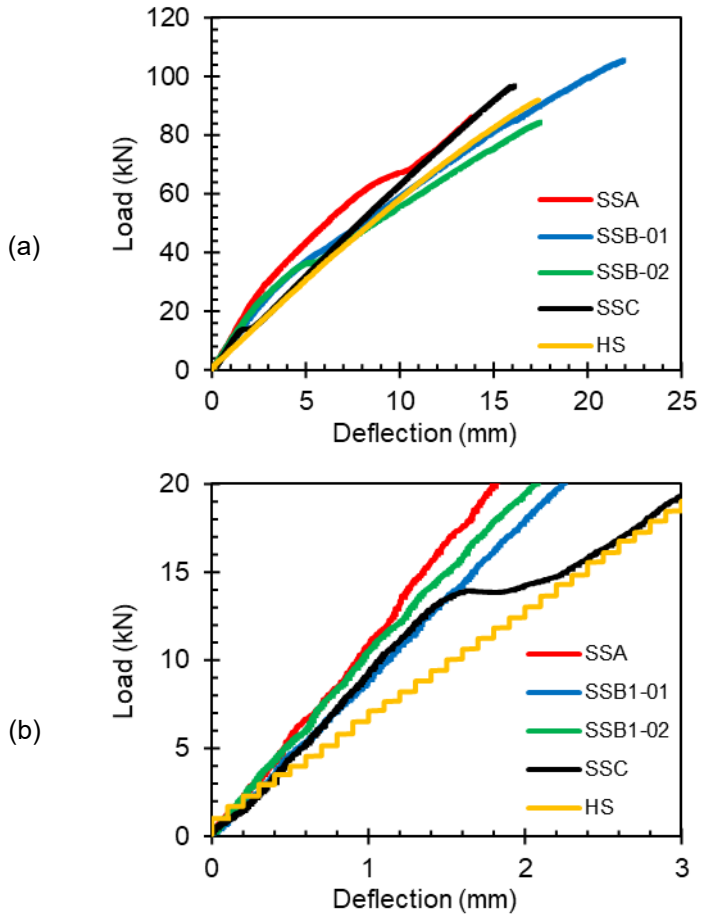

Figure 3-35 Load-deflection plots for 1 m slab specimens: (a) full curves and (b) zoomed in plot to show initial stiffness and stiffness drop in specimen SSC1-01

Each group of 2 m slab sections with epoxy and aggregate bond had similar load-deflection curves. The only anomaly to this was that the 35 mm slab specimen that failed due to bond had a higher overall stiffness than the ones that failed by concrete crushing, the initial stiffness of this specimen was comparable to the other two in its group. All specimens followed a non-linear trend, it being most noticeable in the 35 mm specimens and least pronounced in the 75 mm specimens. Peak load and overall stiffness behaved predictably, the thicker slab specimens were stiffer and generally had the highest peak loads. The only exception to this was the 55 mm specimen that failed by concrete crushing (SSA2-55-03)

which had the second highest overall peak load of the epoxy and aggregate bonded specimens.

The load deflection responses of the bolt bonded slab sections were less consistent than those from epoxy and aggregate bonded specimens. The results of first round of specimens tested differed from the others significantly and were considered outliers. These specimens were overall less stiff and had lower peak loads compared to other specimens with the same slab thickness. The most likely cause for this discrepancy was a calibration error in the testing instrumentation. Excluding the outliers, initial stiffnesses for the 35 mm and 55 mm slab specimens were similar, with the 55 mm being slightly higher. These specimens also had similar initial stiffness to the 2 m long hollow specimens tested. The 75 mm sections had the highest initial stiffness of the group. Again, excluding the outliers, peak load followed the same trend of the thicker slabs having the highest peak loads and the thinner slabs having the lowest, like the behaviour observed for the epoxy and aggregate bonded slab specimens. A unique observation made about the bolted sections was that their failure seemed to be governed by deflection rather than load. More noticeable in the 55 and 75mm sections (excluding outliers), failure occurred at varying loads, but had a consistent maximum deflection in the range of 23 to 25 mm. It was hypothesised, given the failure mode, that there was a certain point at which the opposite motion of the inward rotation of the bolts and outward slippage of the concrete caused the concrete to fail in tension before the bond or concrete compressive strength could govern. More testing on this type of beam would be needed to confirm this hypothesis.

Figure 3-36 shows load-deflection plots for the 2 m slab sections. The lighter coloured curves on the SSB2 plot are for the results considered to be outliers.

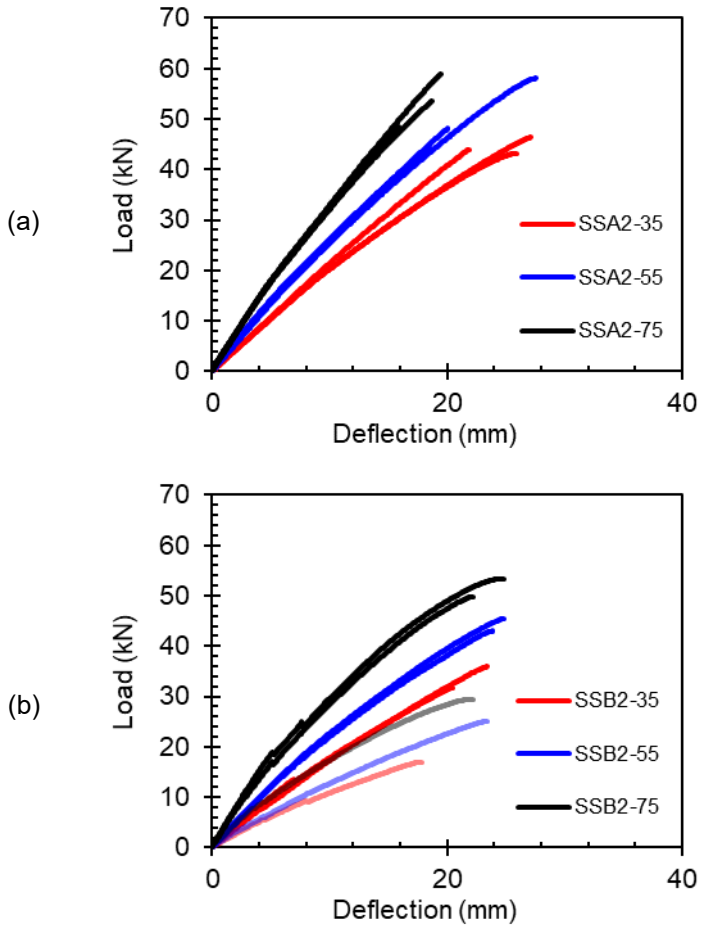

Figure 3-36 Load-deflection plots for 2 m long slab specimens: (a) SSA2 and (b) SSB2

As predicted, the addition of concrete slabs, regardless of bonding method, significantly increased stiffness in the hollow FRP beams. To quantify this, initial stiffness was estimated for each 2 m slab section and compared to that of the hollow sections. Initial stiffness was calculated by taking slope of the load-deflection curves in the linear region, in a range between loads of 0 and 10 kN depending on how linear they were (determined by a linear regression between the 0 and 10 kN threshold). Table 3-16 shows this comparison in stiffnesses between hollow and slab specimens. Figure 3-37 corresponds to this as well. Note that specimens SSB2-35-01, SSB2-55-01, AND SSB2-75-01 were

considered outliers and were not included when calculating mean initial stiffness for their respective specimen groups.

Table 3-16 Initial stiffness comparison between hollow and slab specimens

Specimen Group	Mean Initial Stiffness (kN/mm)	Stiffness Increase
HS	0.794	N/A
SSA2-35	2.108	62%
SSA2-55	2.709	71%
SSA2-75	3.610	78%
SSA2-35	1.719	54%
SSA2-55	2.360	66%
SSA2-75	3.777	79%

(a)

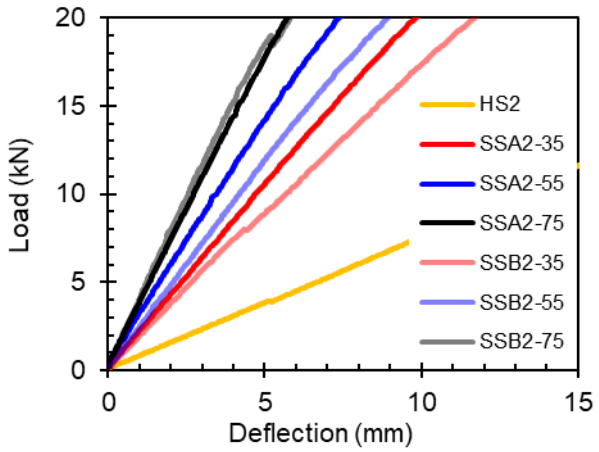

(b)

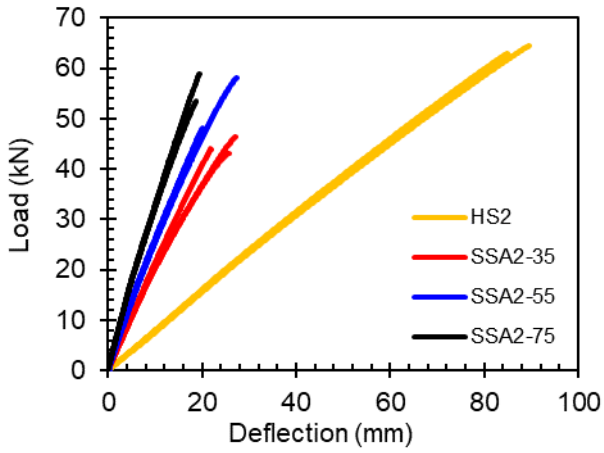

(c)

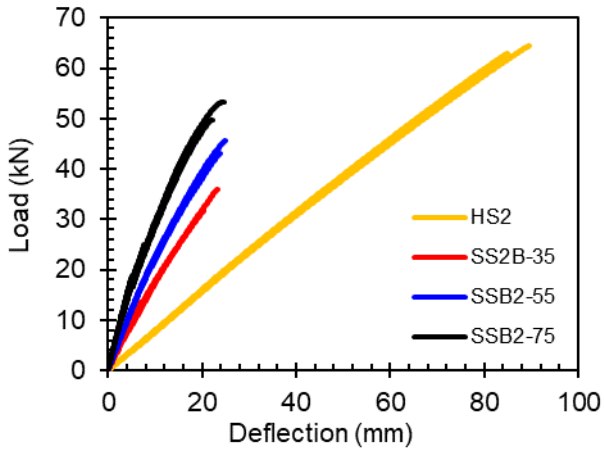

Figure 3-37 Stiffness comparison between hollow and slab sections: (a) initial stiffness comparison for all specimens, (b) full comparison for hollow and SSA2, and (c) full comparison for hollow and SSB2 (outliers not included)

3.5.3 Load-Strain Behaviour

Strain gauges were applied to all specimens except the first 1 m long hollow beam tested and the 1 m long slab sections. For all specimens, one gauge was placed at the center of the tension face. The hollow and filled specimens had a second gauge placed at the center of the compression face, while the 2 m long slab specimens had a second gauge placed on a side wall at midspan, 10 mm from the compression face. The strain gauges were used to collect information on the compressive and tensile nature of the specimens, and to estimate the location of the neutral axis of the beams, to be used as reference for the analytical model.

Bending strain in the hollow sections followed a linear trend with the tensile strain always being larger than the compressive. This was expected given the elastic moduli of the materials (the tensile being slightly less than the compressive). A load-strain plot for hollow specimens is shown in Figure 3-38. Strain gauges on the compressive face tended to fail prematurely, which can be seen in the 2 m specimens by the decrease near peak load. Similar behaviour was noted well before peak load in the 1 and 3 m specimens, which is why a "projected strain" was used. This projected strain was obtained by applying the linear equation of the "good" data to the loads obtained during testing. The 1 m long beam that had strain recorded had the lowest strain capacity of all the hollow beams. The peak strains for the 2 m and 3 m long beams were similar.

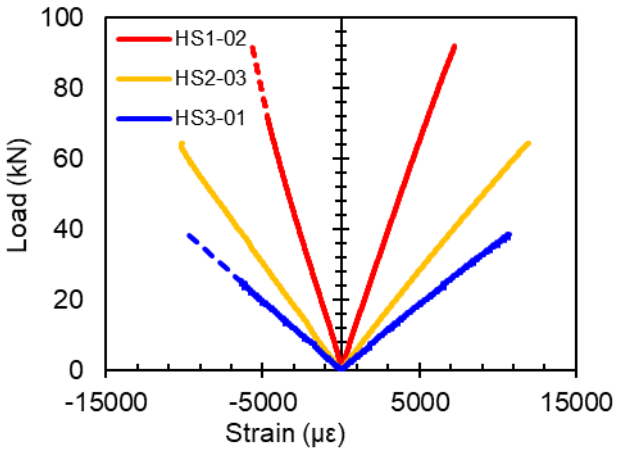

Figure 3-38 Load-strain plot for hollow specimens, dotted lines represent projected strains

The load-strain data from the filled tests seems to be bi-linear in nature. Both the initial tensile and compressive slope of the test indicated that it would end up having less strain capacity than a 2 m hollow specimen, but when the equivalent of approximately 15 kN of load had been applied to one beam, the slope decreased, becoming closer to that of the hollow specimens. As mentioned, audible cracking noises were heard throughout the test, some of which may be attributed to the encased concrete cracking. This could be a reason why the load-strain data appeared to be bi-linear. In all, the filled section had nearly the same tensile and compressive strain capacity as the hollow specimens of the same length. As with some of the hollow sections, the compressive strain gauge on the filled specimen failed prematurely, so a projected strain was used. This projected strain was calculated in the same manner as that of the hollow specimens. The load strain plot for the filled section is shown in Figure 3-39, with hollow section HS2-03 included for comparison.

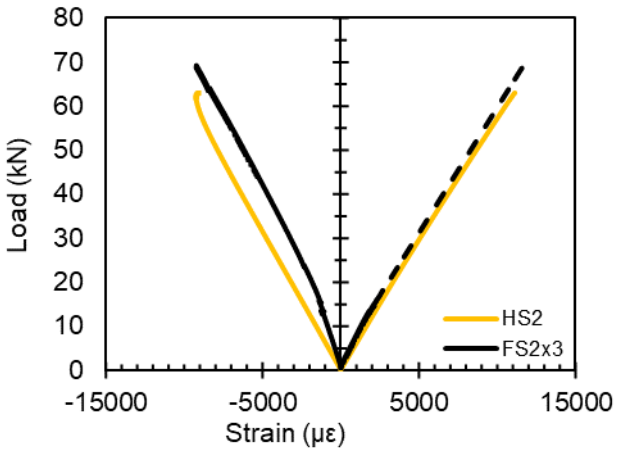

Figure 3-39 Load-strain plot for filled section with hollow specimen as reference, dotted line represents projected strain

Strain capacity in the epoxy and aggregate bonded slab specimens was less than the hollow beams due to the concrete. Crushing failure in the concrete is expected to occur at 3500 με, which is much less than the average compressive strain in of 9156 με in hollow specimens. In general, the reduced strain capacity can be attributed to the increased stiffness in the beams, although failure mode (specifically whether the concrete crushed or not) can be directly associated with the amount of strain in the slab. The projected compressive strain at the top of the concrete slab was calculated using Equation (3-3) and the strain diagram in Figure 3-40, based on the assumption that the concrete and FRP were fully bonded until failure. While it did not perfectly indicate crushing failure at 3500 με and should not be taken as the actual strain in the concrete, it was able to show that specimens that experienced crushing failure exceeded this threshold. Those that failed due to bond did not exceed the 3500 με threshold.

$$\varepsilon_{Cc} = \frac{d\varepsilon_{F1} - H(\varepsilon_{F1} - \varepsilon_{F2})}{d} \tag{3-3}$$

where: ε_{Cc} is the calculated strain at the extreme compressive fiber in the concrete slab

ε_{F1} is the strain at the extreme tensile fiber, taken from strain gauge data

ε_{F2} is the is the strain in the FRP near the concrete-FRP interface, taken from strain gauge data

d is the distance from between the two strain gauges

H is the total height of the specimen

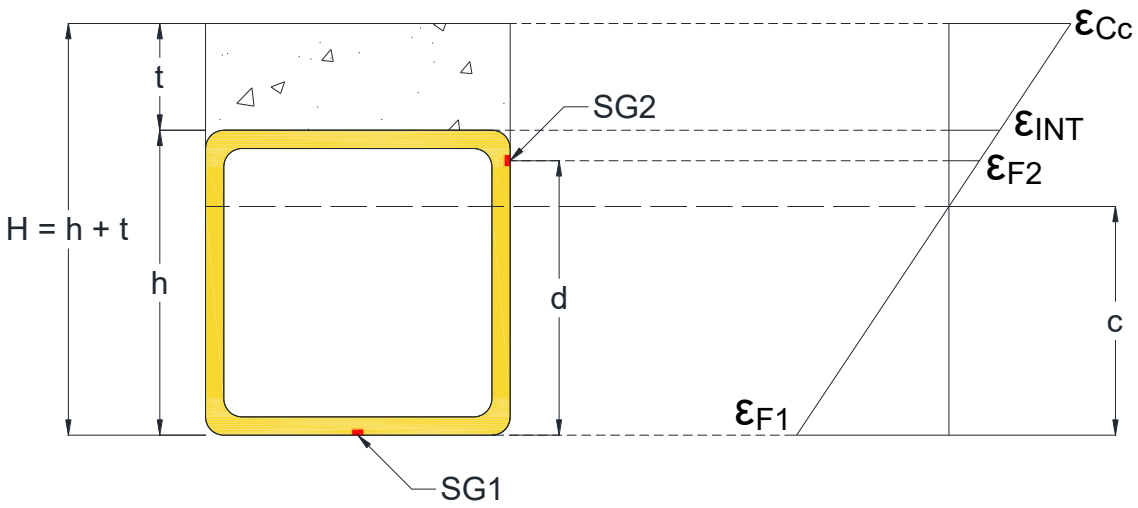

Figure 3-40 Strain diagram corresponding to Equations (3-3) and (3-6).

Strain capacity in the bolt bonded slab specimens was also limited due to concrete. When compared to the epoxy and aggregate bonded specimens, there was not much difference in strain capacity. The epoxy and aggregate bonded specimens generally had a slightly higher tensile strain capacity, while the "compressive" strain capacity (based off recordings from the strain gauge attached to the side wall, closer to the compression face) was generally greater for the bolt bonded specimens. Projected concrete compressive strain was not calculated for the bolt bonded specimens. Strain was a less indicative measure of failure in these specimens because, as mentioned, they seemed to be controlled by deflection. Load-strain plots for slab specimens are shown in Figure 3-41.

(a)

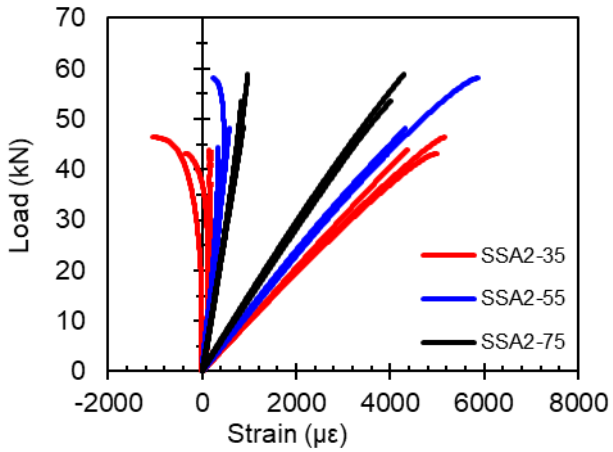

(b)

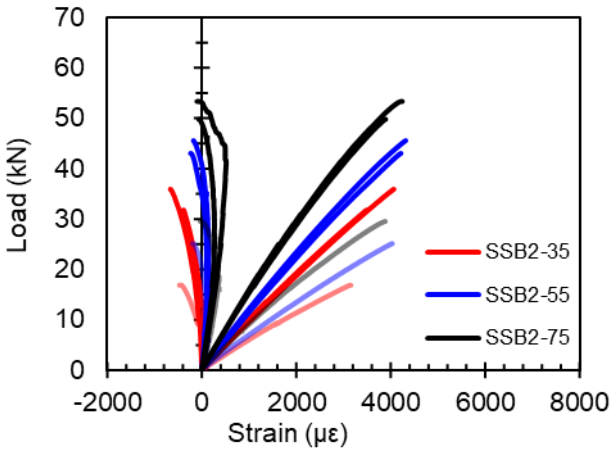

Figure 3-41 Load-strain plots for slab specimens: (a) SSA2 and (b) SSB2

3.5.4 Bending Moment Data

3.5.4.1 Moment-Curvature Behaviour

For each bending test, bending moment and curvature were calculated from the data using Equations (3-4) and (3-5), respectively.

$$M = \frac{P}{2}(a) \tag{3-4}$$

$$\psi = \frac{|\varepsilon_T| + |\varepsilon_c|}{d} \tag{3-5}$$

where: M is the calculated moment

P is the load, taken from load cell data

a is the distance from the support to the closest point load

ψ is the calculated curvature

ε_T is the tensile strain, taken from strain gauge data

ε_C is the compressive strain, taken from strain gauge data

d is the distance from between the two strain gauges

Moment-curvature followed a linear trend for the hollow sections with the 2 m long sections having the highest moment capacity while also experiencing the most curvature. Non-linear behaviour near the peak moment was attributed to strain gauge malfunction. The epoxy and aggregate bonded slab sections followed a generally linear trend as well, while the bolt bonded slab specimens had more pronounced non-linearity. Moment-curvature plots can be seen in Figure 3-42.

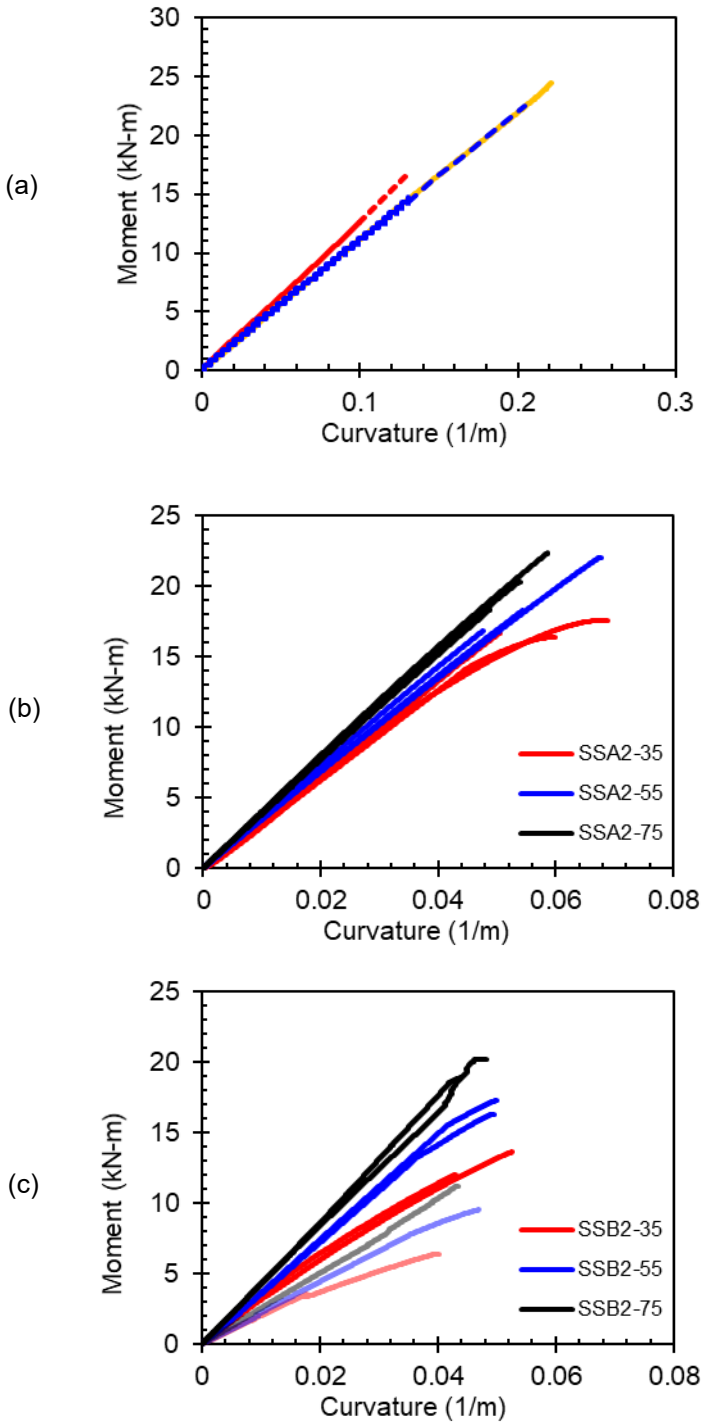

Figure 3-42 Moment-curvature plots: (a) hollow specimens, (b) SSA2 and (c) SSB2

Moment-curvature plots were mostly used to compare to results from the analytical model. The moment-curvature response was also useful for confirming two pieces of information

taken from other data. First, the stiffness of the hollow FRP sections does increase when concrete is added. Examining the moment-curvature plots, it can be seen that stiffness (slope) increases slightly for the filled section when compared to hollow. Stiffness increases in the slab sections are much more noticeable and are related to slab thickness. Second, that failure in the bolt bonded slab sections was deflection (or rotation) controlled. The trend of failing around similar levels of deflection is reflected by the curvature, and while deflection and curvature are directly related, curvature being the second derivate of vertical displacement, the curvature was calculated using strain data. Having these data match up confirms the validity of failure in the bolted slab specimens being deflection controlled.

3.5.4.2 Neutral Axis versus Moment Plots

Estimated neutral axis data was also calculated for each bending test, using Equation (3-6). The corresponding strain diagram for this equation is shown in Figure 3-40 (above). For the 2 m hollow and slab sections, it was plotted against the bending moment data.

$$c = \varepsilon_{F1}\left(\frac{d}{\varepsilon_{F1} - \varepsilon_{F2}}\right) \tag{3-6}$$

where: c is the calculated neutral axis location with respect to the bottom of the FRP

ε_{F1} is the strain at the extreme tensile fiber, taken from strain gauge data

ε_{F2} is the is the strain in the FRP near the concrete-FRP interface, taken from strain gauge data

d is the distance from between the two strain gauges

The neutral axis location was used mostly to compare with the analytical model. It did serve one main purpose to the experimental testing though, confirming that the slab

thicknesses used were effective in creating three different scenarios for the neutral axis, one being in the FRP web (35 mm), one being close to the concrete-FRP interface (55 mm) and one being in the slab itself (75 mm). Shown on the neutral axis-moment graphs is a line indicating the location of the concrete-FRP interface (100 mm from the bottom of the FRP) for comparison with the estimated location of the neutral axis throughout the test. Also, as expected, the neutral axis for the hollow sections fell around the middle of the cross section.

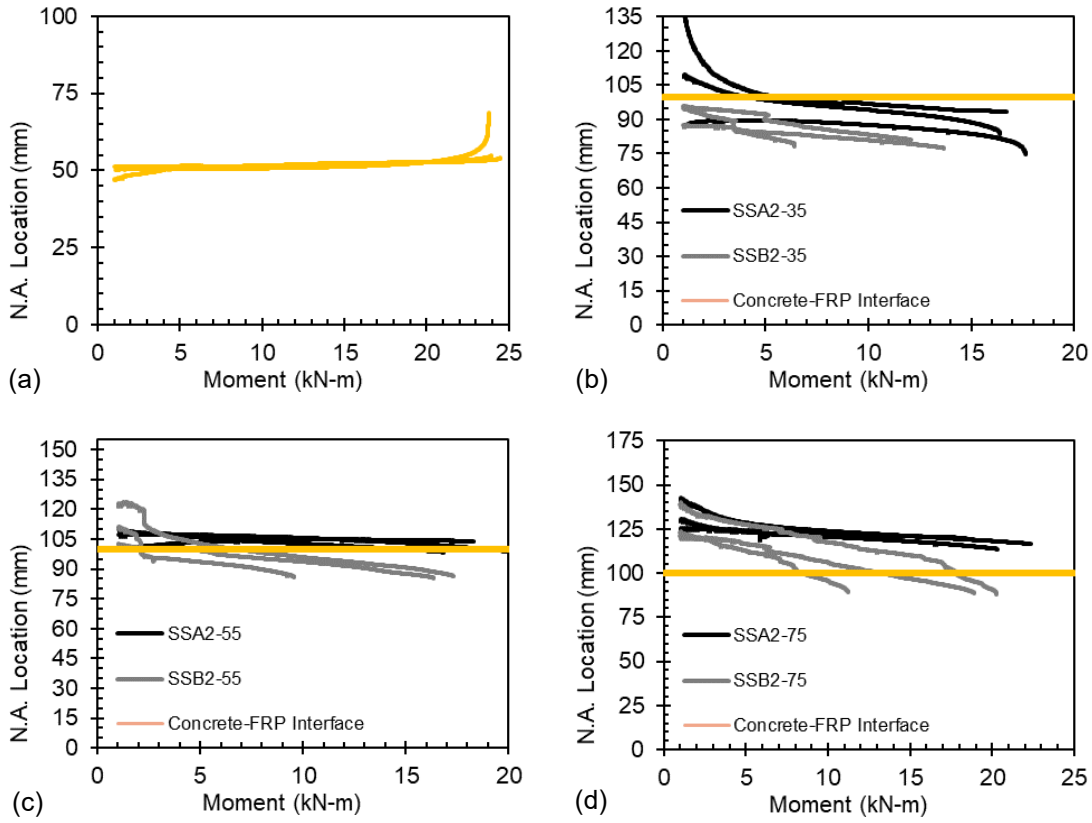

Figure 3-43 Neutral axis location vs. moment diagrams: (a) hollow specimens, (b) 35 mm slab sections, (c) 55 mm slab sections, and (d) 75 mm slab sections

3.6 EXPERIMENTAL PROGRAM SUMMARY

Reviewing the results of experimental testing, it was observed that while the addition of concrete decreased system strength, it increased overall stiffness of the sections. Depending on slab size, stiffness increased between 62 and 78% for the epoxy and aggregate bonded specimens, while the bolt bonded specimens had a stiffness increase of between 54 and 79%. Given these stiffness increases and failure modes of the sections, it seems as if the epoxy and aggregate bonded specimens could be suitable for bridge decking use. Though the key metric of having a stiffness increase compared to the hollow sections was met for both bonding methods, the higher ultimate load capacity of the epoxy and aggregate bonded beams makes them a more promising concept to be used as a component of a bridge decking system. Obviously, using the epoxy and aggregate bonded beams as bridge decking would be dependent on further testing.

CHAPTER 4 ANALYTICAL MODELING

Numerical modelling was used to predict behaviour of the four-point bending specimens. Two models were developed, a linear one for the hollow sections and a non-linear one for the slab sections. Material properties of the FRP sections obtained from coupon testing (and concrete compressive testing where applicable) were used in equations mentioned in the Section 2.3 (Review of Beam Theory) to create load-deflection and moment-curvature plots that could be compared to experimental results. Developing and using these models can help to understand behaviour under load, specifically how flexure and shear both contribute to deflection, as well as assist in predicting the type of failure that will occur in the specimen. Above all, the models can be used to justify test results. This section will analyze the models and explain methods and assumptions used to develop them.

4.1 MODELLING HOLLOW FRP SECTIONS

As mentioned, a linear model was used to predict behaviour of the hollow FRP sections under four-point bending. A linear model was chosen because the specimens behaved in a linear-elastically during experimental testing. There were two main components to the model: predicting the slope of the load-deflection curve (stiffness when combined shear and bending effects were considered) and predicting the failure load of the specimen. After finding these components the model could be easily modified to predict load-strain or moment-curvature behaviour.

4.1.1 Load-Deflection Behaviour

Modelling the load-deflection response of the hollow specimens took place in three main phases. First, material properties for the FRP were obtained from material testing, as

outlined in Section 3.1.2. Next, a cross-sectional analysis was conducted to get the section properties of the specimens. Finally, once all material and cross-sectional properties were known, values were put into the equations for bending and shear deflection, Equations (2-3) and (2-4), respectively. Equation (2-5) was used to give the total deflection due to combined bending and shear at any given load.

For the cross-sectional analysis, the cross-section dimensions of the hollow FRP beam as well as length and shear span were used as known inputs. Also known were the tensile and compressive strengths and moduli from material testing. The end goal of this analysis was to obtain values for the neutral axis location and moment of inertia. Since the FRP material had different compressive and tensile properties, a transformed section was used. The dimensions of the compressive region of the beam were transformed using the factor *n*:

$$n = \left(\frac{E_C}{E_T}\right) \tag{4-1}$$

where: n is the transformation factor for dimensions in the compressive region
E_C is the compressive modulus of the FRP
E_T is the tensile modulus of the FRP

After the section had been transformed to reflect the tensile properties of the FRP beam, an area balance was performed on the section to get a quadratic equation that yielded the neutral axis location:

$$c = \frac{-4th + \sqrt{(4th)^2 - 4[2(t_{TR} - t)][-2th^2 + t^2(b_{TR} - 2t_{TR}) - (b - 2t)]}}{2[2(t_{TR} - t)]} \tag{4-2}$$

where: c is the neutral axis location in relation to the compression face of the FRP

t is the wall thickness of the FRP cross-section

h is the height of the FRP cross-section

b is the base width of the FRP cross-section

t_{TR} is the transformed wall thickness in the FRP compressive region

b_{TR} is the transformed base width in the FRP compressive region

After finding the neutral axis location of the cross-section, moment of inertia was found still considering the compressive region as transformed:

$$I_{C_{TR}} = \frac{1}{12}\left[c{b_{TR}}^3 - (c-t)b'^3\right] \tag{4-3}$$

$$I_T = \frac{1}{12}[(h-c)b^3 - (h-c-t)b'^3] \tag{4-4}$$

$$I_{TR} = I_{C_{TR}} + I_T \tag{4-5}$$

where: I_{CTR} is the moment of inertia in the compressive region of the section

I_T is the moment of inertia in the tensile region of the section

I_{TR} is the transformed moment of inertia of the section

From this, the stiffness parameter, D, was obtained using the following:

$$D = EI_{TR} \tag{4-6}$$

where: D is the flexural rigidity of the beam

E is a modulus of elasticity of the FRP, either compressive or tensile

In Equation (4-6), either tensile or compressive modulus could be used depending on the FRP material. For the FRP beams used in this study, tensile modulus governs over compressive, so the value of E_T would be inputted in the equation to solve for D. At this point, all values needed to solve for the bending component of deflection were known.

The remaining unknown values for shear deflection were the shear modulus, G, and shear area of the cross-section with the shear coefficient, kA. Shear modulus was assumed to be 3 GPa, deemed acceptable for pultruded FRP material if sufficient test data is not available, as referenced by Mottram's findings (Mottram 2004; Nguyen et al. 2018). For shear area and coefficient, four different equations were used and were made editable to see the effect of changing the property on the total predicted deflection. After trial and error, it was found that Equation (2-7), proposed originally by Omidvar (1998), gave a value that was most accurate when compared to experimental results.

With all inputs for both bending and shear components of deflection known, values were inserted into Equations (2-3), (2-4), and (2-5). The value for load, P, was left as a variable to be filled by the ultimate load.

4.1.2 Ultimate Load

Observing four-point bending test results, pure tensile or compressive failure did not occur for the setup and shear span used. Failure consistently affected the webs of the hollow sections. It was first assumed to be a shear failure originating around the corners of the specimens, but the predicted ultimate failure load due to pure shear underestimated the ultimate load reached during testing. It was decided that the combined effects of bending

and shear should be considered when calculating an ultimate load, which made sense given these effects were considered in the deflection prediction for the beams.

Along with the properties c and I_{TR}, values for the first moment of area, Q, at two different points on the cross section were calculated. When considering pure shear, the value Q_c was used. It was calculated at the point where shear stress is maximum, the neutral axis, in relation to the compression face. For combined shear and bending, the value Q_i was used. This value was calculated at the web-flange interface of the FRP section in relation to the web. This location was chosen to represent where shear stress along the cross section would see a significant increase, and because it seemed to be where failure in the test specimens originated. The web-flange interface may not be the exact location where failure originates, but using this spot gives a conservative estimate for ultimate load when used in the combined shear and bending equation, discussed below.

Ultimate load for four different types of failure was calculated. Equations (4-7) and (4-8) predict the ultimate load for pure tension and compression, respectively. Although these failure modes did not govern for the specimens and setup tested in this study, modifications to beam length and shear spans could lead to a compressive or tensile in similar specimens. Equations (4-9) and (4-10) predict ultimate load for a pure shear failure and combined bending and shear failure, respectively. Equations (4-7), (4-8), (4-9) are derived from the basic mechanical equations, listed in Section 2.3 as Equations (2-10), (2-11), (2-12), and (2-13). Equation (4-10) is based on one derived from basic mechanics and used to predict ultimate loads in hollow FRP sections by Muttashar et al. (2016). Known values were put into these equations to obtain predicted values for ultimate load.

$$P_{ULT_{B-T}} = \frac{2\sigma_T I_{TR}}{ac} \tag{4-7}$$

$$P_{ULT_{B-C}} = \frac{2\sigma_C I_{TR}}{a(h-c)} \tag{4-8}$$

$$P_{ULT_S} = \frac{2\tau_{ULT} I_{TR} t}{Q_c} \tag{4-9}$$

$$P_{ULT_{SB}} = \left(\frac{ac}{2I_{TR}\sigma_{ULT}} + \frac{Q_i}{2I_{TR}\tau_{ULT}t}\right)^{-1} \tag{4-10}$$

where: $P_{ULT\,B\text{-}T}$ is the predicted failure load due to bending with tensile failure

$P_{ULT\,B\text{-}C}$ is the predicted failure load due to bending with compressive failure

$P_{ULT\,S}$ is the predicted failure load due to pure shear

$P_{ULT\,SB}$ is the predicted failure load due to combined shear and bending

σ_T is the tensile strength of the FRP

σ_C is the compressive strength of the FRP

τ_{ULT} is the ultimate shear strength of the FRP

Q_c is the first area of moment about the neutral axis of the cross-section

Q_i is the first area of moment about the web-flange interface of the cross-section

a is the distance from the end of the beam to the nearest loading point

Other variables used have been mentioned previously in this section.

4.1.3 Comparison of Model and Experimental Results

When comparing the analytical model to experimental test results the predicted ultimate load due to a strictly tensile or compressive failure is much higher than the actual failure

load. With shorter spanned beams the ultimate predicted load due to combined bending and shear seems to match well with experimental results, but when span length increases this prediction becomes less accurate. Pure shear gives the closest prediction for the 3 m long hollow specimen, but this could be coincidental as the combined bending and shear prediction for the 1 and 2 m beams fit experimental data the best. It is likely that there is some threshold for when pure shear (and conversely pure bending) governs over the combined failure mode. The factor that influences this would be the ratio between shear span and length of the specimen. More testing would need to be done on specimens of different lengths to confirm what this threshold is though.

Table 4-1 and Figure 4-1 show a comparison of results between the model and experimental data for the three different lengths of hollow specimens.

Table 4-1 Comparison of results from experimental data and analytical model

Specimen I.D.	Length (mm)	Ultimate Load (kN)			Deflection at Peak (mm)		
		Experimental	Model	CV	Experimental	Model	CV
HS1-02	1000	91.9	91.2	0.8%	17.4	16.2	7.2%
HS2-03	2000	64.5	63.1	2.2%	89.7	79.0	12.0%
HS1-03	3000	38.8	48.2	24.2%	177.5	202.9	14.3%

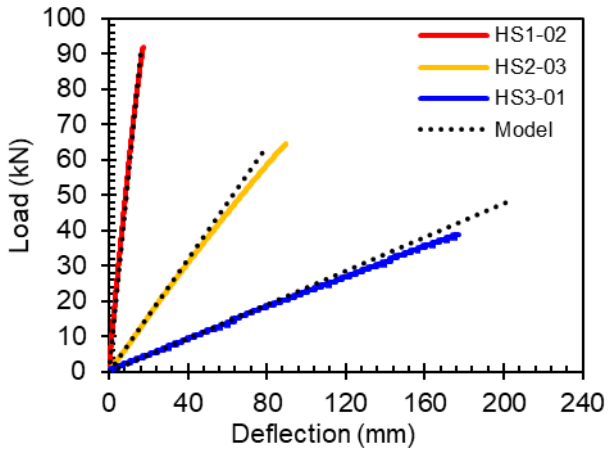

Figure 4-1 Load-deflection plot with experimental data and model predictions

4.2 MODELLING SLAB SECTIONS

The end goal of modelling the slab sections was the same as the hollow sections in that the model needed to be able to predict stiffness from load-deflection and ultimate load. The process for modelling the slab sections was slightly different though. A non-linear model was used for these sections because concrete is a non-linear material and gives the composite section a material non-linearity that did not need to be considered for the linear-elastically behaving hollow sections.

4.2.1 Load-Deflection Behaviour

To model load-deflection in the slab sections, the moment-curvature behaviour had to be modeled first. The first step to this was completing a cross-sectional analysis to determine the neutral axis of the section in an unloaded condition. Once a formula had been generated that could predict the initial neutral axis, an initial strain was assumed at the extreme tensile fiber of the FRP. The stresses along the cross-section (both in FRP and concrete) were determined at different layers, a layer width of 1 mm was used in this analysis, but this was

an arbitrary value that could be increased or decreased depending on section size. For concrete in compression, Equation (4-11) was used to determine stress in a layer (Sadeghian and Fam 2010). A linear stress-strain relation was used for concrete in tension, as well as for FRP regardless of whether it was in tension or compression.

$$f_c = f'_c \left[2\frac{\varepsilon_c}{\varepsilon'_c} - \left(\frac{\varepsilon_c}{\varepsilon'_c}\right)^2 \right] \quad (4\text{-}11)$$

where: f_c is the stress in the concrete layer

f'_c is the concrete compressive strength

ε_c is the strain in the concrete layer

ε'_c is the strain in the concrete layer at f'_c

The stresses were then multiplied by layer area to get a specific force for that layer and all forces were summed. The sum of forces value was used as a check to see if the neutral axis depth used was accurate or not, if the sum of forces was equal to approximately zero the value was deemed acceptable. Usually, the original value calculated was not equal to zero. Microsoft Excel's "Goal Seek" function was used to determine what neutral axis depth would make the summed forces approximately zero in these cases. After the force check was satisfied, the sum of moments was calculated. The curvature was calculated as the slope of the strain profile of the section, which was then plotted against the value of the summed moments. The initial strain was increased, and the process was repeated to give a complete moment-curvature profile of the cross-section. The cut-off point for the moment-curvature profile was when calculated strain at the extreme compressive fiber of the concrete reached its crushing point, 3500 με per CSA A23.3 (Design of Concrete Structures) (CSA Group 2014). Inputs for slab thickness and material strength were

variable, so model moment-curvature profiles for different experimental conditions used in the study could easily be generated.

Based on the moment-curvature behaviour, load deflection behaviour was determined using Figure 4-2 along with Equations (4-12), (4-13), (2-4), and (2-5) (Equations (2-4), and (2-5) used for calculating deflection due to shear and total deflection, respectively). The modelled moment-curvature response was quadratic but not overly non-linear, because of this, secant area under the curve was taken at each initial tensile strain point to obtain deflection values rather than fully integrating the curve, a plot showing secant areas can be seen in Figure 4-3.

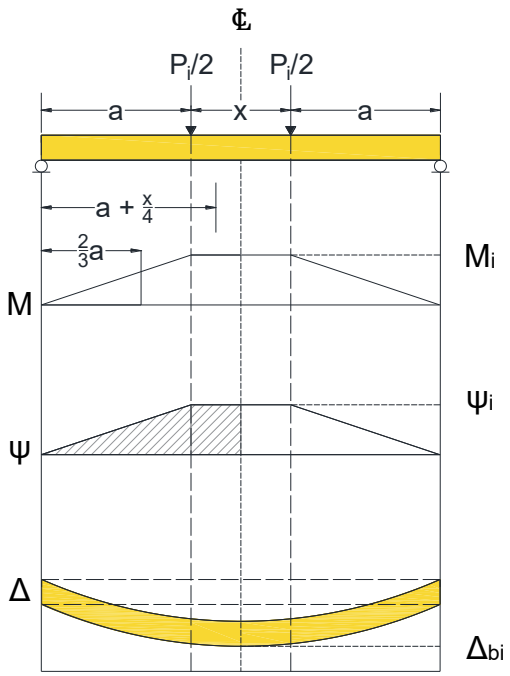

Figure 4-2 Beam diagrams used to determine deflection due to bending in slab sections

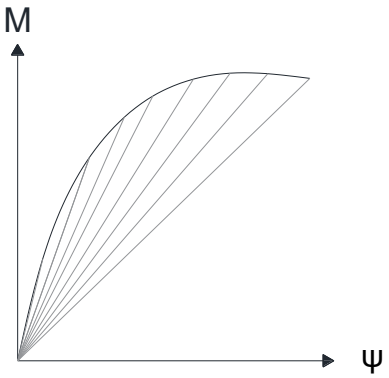

Figure 4-3 Sample moment-curvature diagram with secant lines

$$P_i = \frac{2M_i}{a} \tag{4-12}$$

$$\Delta_{bi} = \frac{\psi_i a^2}{3} + \frac{\psi_i x}{2}\left(a + \frac{x}{4}\right) \tag{4-13}$$

where: P is the calculated load on the beam

M is the moment obtained from the moment-curvature analysis

Ψ is the curvature obtained from the moment-curvature analysis

Δ_b is the calculated deflection due to bending

x is the shear span of the beam

a is the distance from the end of the beam to the nearest loading point

The modelled moment-curvature profile and subsequent load-deflection profile was created assuming full composite action between the concrete and FRP, however, it is unlikely that the slab sections tested were fully composite. Considering that the concrete slabs slipped when loaded (as shown in the load-slip plots in Figure 3-32, above), it was concluded that the concrete slabs were not perfectly bonded to the FRP and were only partially composite. Modelling partial composite action was not in the scope of this research, so a lower bound to the model that assumed no composite action was created

instead to provide an estimate of how much composite action was occurring between the concrete and FRP.

A linear model was used for the lower bound. The FRP portion of the section was transformed to concrete properties, and equations (2-3) and (4-10) were used to model peak deflection due to bending, and ultimate load, respectively. Deflections due to shear in the transformed section were negligible.

4.2.2 Ultimate Load

From reviewing the literature (on FRP SIP formwork) and observing experimental tests, FRP properties never governs failure for the slab sections. By design, the process for creating the moment-curvature profile of the section is cut off when the calculated concrete strain reaches crushing failure, so by default the ultimate load predicted by this model is for when crushing should occur.

The other failure types observed during experimental testing were bond failure in the epoxy aggregate bonded specimens and tensile concrete failure in the bolt bonded specimens (caused by excessive bolt rotation, brought on by bond failure between the concrete and FRP.). These both occur before concrete can reach its crushing strain, so the model needed to be truncated based on the predicted ultimate loads of these failures. To predict ultimate load at bond failure, bond strength needed to be calculated first. This was done by taking the average moment at debonding failure for each specimen group (SSA2-35, SSB2-35, SSA2-55, etc.) and putting it into the non-linear model. The model was used to back-calculate the strain at the extreme tensile fiber for this moment and produce forces for each

1 mm layer of the section. The sum of forces across all layers was taken and used in Equation (4-14) to calculate bond strength for each specimen group.

$$\tau_{BOND} = \frac{\sum F_C}{b\left(L/2\right)} \tag{4-14}$$

where: τ_{BOND} is the bond strength (or stress)

ΣF_C is sum of forces in each layer under compression along the cross-section (the sum of tensile forces could also be used instead)

b is the bond width, in this case the width of the concrete slab

L is the specimen length

The bond strength between the concrete and FRP was taken as the average bond strength of all epoxy and aggregate bonded specimens that failed due to debonding: 1.63 MPa. Equation (4-14) was used to calculate bond stress for each initial strain value used in the model. Once the bond stress exceeded the bond strength calculated for each group of sections, bond failure was assumed to have occurred. The upper and lower bounds of the model were truncated at the load corresponding to the moment at which the bond strength was exceeded.

4.2.3 Comparison of Model and Experimental Results

The model was used to predict moment-curvature and load-deflection response for the three slab sizes and the two bonding methods for each of them. The difference between parameters during the model runs was slab thickness and concrete strength. Concrete strength was generalized based on the results of the concrete compressive strength testing. For the most accurate results the strength for each set of specimens could have been used

but using an average concrete strength across different slab sizes was deemed acceptable for the purposes of this study.

Load-deflection predictions in general followed the curve for the upper bound of the model rather than the lower. Load-deflection in thinner slabs was more accurately predicted than in thicker ones. The initial stiffness predicted by the model in most cases generally matched the experimental curves, but as load increased the experimental data softened at a much higher rate than the model did. Ultimate load predictions based on crushing failure underestimated the ultimate load obtained from the experimental data. The largest discrepancy between the model and test data was 7%. Ultimate load predictions based on debonding failure both overestimated and underestimated results from experimental testing, the largest discrepancy being 11%. While this model can predict a range that the load-deflection curve for a slab section would be in, to accurately model the behaviour of the slab sections partial composite action would need to be considered. Plots showing the comparison between experimentally tested and modelled load-deflection behaviour can be seen in Figure 4-4 (below) Model predictions for crushing failure were only included for the specimen groups that experienced it: SSA2-35 and SSA2-55.

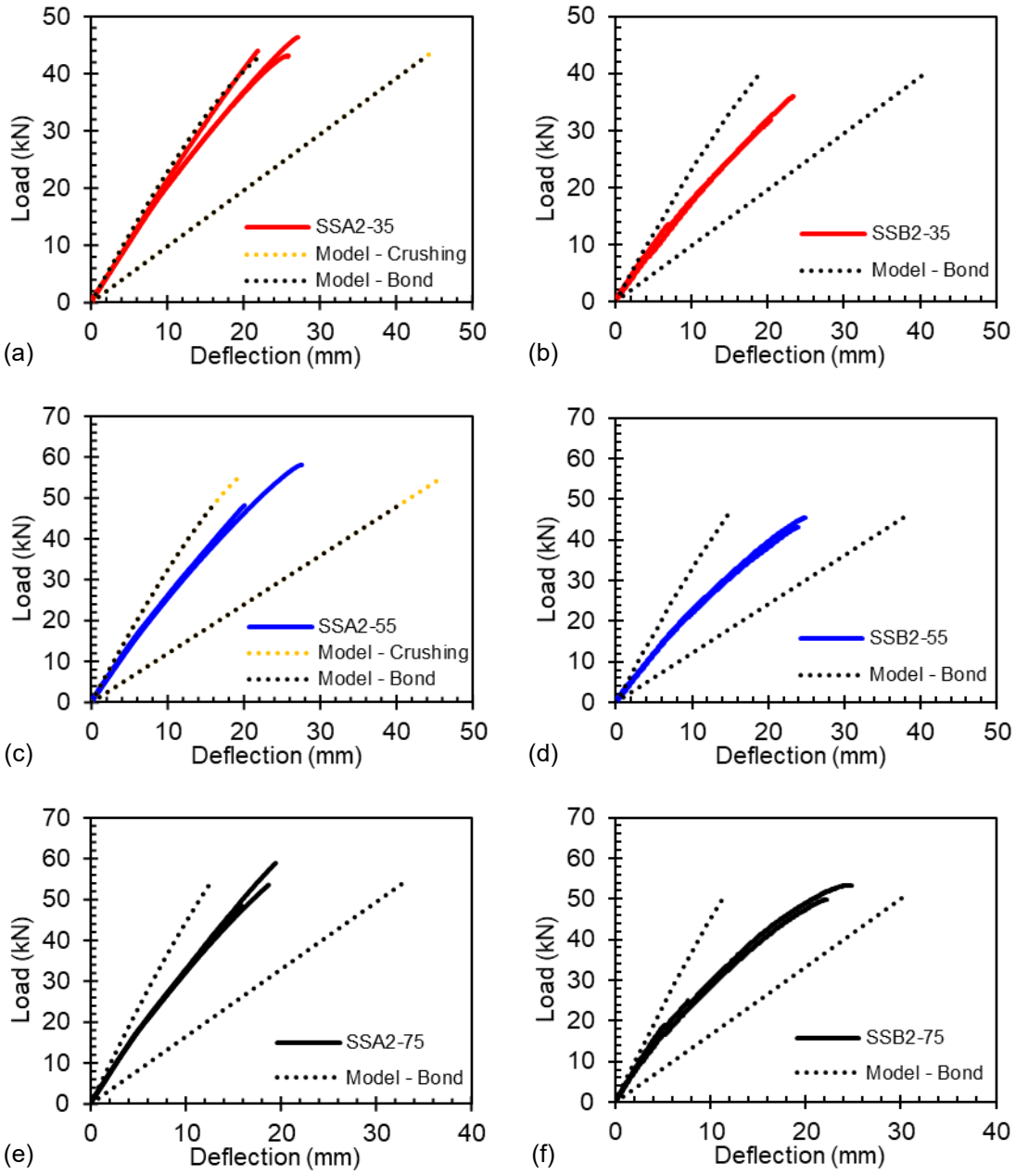

Figure 4-4 Load-deflection plots for slab sections with experimental data and model predictions: (a) SSA2-35, (b) SSB2-35, (c) SSA2-55, (d) SSB2-55, (e) SSA2-75 and (f) SSB2-75

4.3 PARAMETRIC STUDY

A parametric study was conducted on the slab sections to observe the effects of changing variables not considered in the experimental program on load-deflection response. The

parameters analysed were: FRP section geometry, concrete strength, and shear span. These metrics were chosen in an attempt to improve upon the criterion of increasing stiffness compared to hollow sections. Adding slabs of different thickness showed increased stiffness in the sections experimentally tested; this study attempts to model parameters that could further improve stiffness, as well as ultimate load capacity. A "base case" beam was chosen to be modelled for each parameter that represented the results from experimental testing. The base case specimen had the following properties:

- Length of 2 m
- Outer FRP dimension of 100 mm by 100 mm with 6 mm wall thickness
- FRP modulus of elasticity of 36 GPa (only one modulus was used rather than having different tensile and compressive properties)
- Concrete thickness of 55 mm
- Concrete compressive strength of 40 MPa
- Shear span of 20% the total span
- Epoxy and aggregate bond with a bond strength of 1.63 MPa

To model the load-deflection response for the study, the variable parameters for each specimen were used to create upper and lower bounds of each slab section to give a range the curve could fall into. Only bending deflections were considered as shear deflection was negligible. To create a more accurate curve for the modelled load-deflection, a "Composite Percentage Factor" (CPF) was applied to each range. To do this, experimental test results from specimens SSA2-55-01 and SSA2-55-03 (55 mm slab specimens that failed due to debonding and crushing, respectively) were taken determine how compositely the specimens behaved at a certain load. The deflection values at the upper bound were

assumed to be 100% composite, values at the lower bound were assumed to be 0% composite. The experimental deflection results for curves of different failure modes were interpolated in terms of percentage to determine the CPF at each tenth of ultimate load. As an example, a CPF of 90% at any given load indicates that the section was experiencing 90% composite action at that load. The composite percentage factors used for specimens that failed due to debonding and crushing are presented in Table 4-2.

Table 4-2 Composite Percentage Factor values used to model specimens in parametric study.

Percentage of Ultimate Load	CPF – Bond Failure	CPF – Crushing Failure
10%	88%	92%
20%	88%	90%
30%	88%	88%
40%	87%	86%
50%	87%	85%
60%	86%	84%
70%	86%	83%
80%	86%	82%
90%	86%	81%
100% (Failure Load)	86%	78%

To summarize the process of creating curves based on variable parameters: upper and lower bounds to each curve were created for both debonding and crushing failure, the deflection value at intervals of 10% of the ultimate load for each case was then interpolated based on the CPF for each failure type.

4.3.1 Effect of FRP Geometry

The key value affected by changing FRP geometry for a section is the moment of inertia as it used in calculating both ultimate load capacity (Equation (4-10)) and bending stiffness (Equation (4-6)). Four FRP geometries were considered (listed as height by width by wall thickness): 100x100x6 mm (base case), 150x100x6 mm, 100x150x6 mm, 150x150x6 mm. It should be noted that the concrete slab width increased with the base width of the FRP; if the FRP width was 150 mm, the concrete slab width was 150 mm too. A plot showing the effect of changing FRP geometry can be seen in Figure 4-5. The experimental results from tests SSA2-55-01 and SSA2-55-03 are included on this plot for reference. It should be noted that the darker and lighter curves represent predicted behaviour if debonding and crushing failures were to occur, respectively.

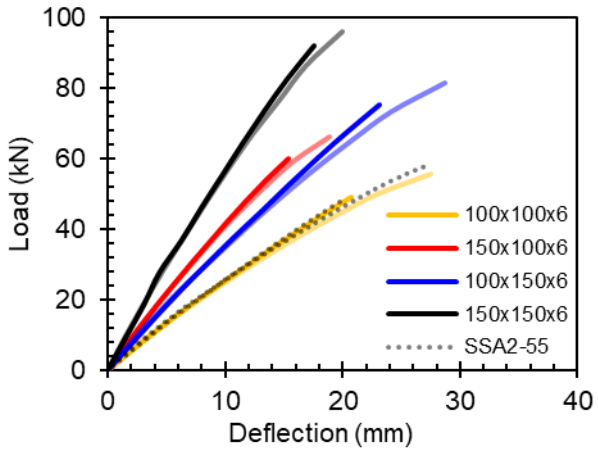

Figure 4-5 Variation of load-deflection plots based on changing FRP geometry

From Figure 4-5, increasing the FRP geometry both increased stiffness and ultimate load capacity. A stiffness increase came from increasing the height of the FRP, creating a strong axis for transverse bending moment to rotate about, load capacity in this specimen was also increased slightly. Conversely, a weak axis was created by increasing only the base width

of the FRP, however, this specimen had increased ultimate load capacity compared to the base case due to the increase in concrete area. Stiffness also slightly increased in this section. Increasing both width and height increased both the stiffness and ultimate load capacity of the sections, as expected. Peak deflections were reduced in sections with increased height.

4.3.2 Effect of Concrete Strength

Changing the concrete compressive strength affected the stress in each layer of the cross-section when modelling the upper bound at different initial strains. Changing the concrete strength also varied the concrete elastic modulus, which was used in transforming the FRP properties. Four concrete strengths were modelled: 35 MPa, 40 MPa (base case), 45MPa, and 50MPa. A plot showing the effect of changing concrete strength can be seen in Figure 4-6. Dark curves represent debonding failure, light curves represent crushing failure.

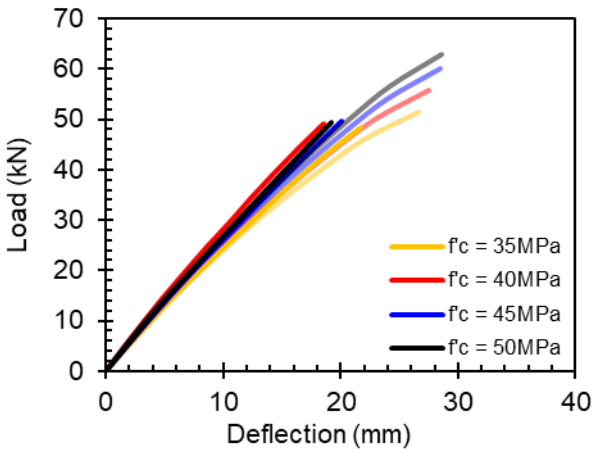

Figure 4-6 Variation of load-deflection plots based on changing concrete compressive strength

As can be seen in Figure 4-6, changing the concrete strength of the slabs did not have much of an impact on the section stiffness or ultimate capacity, compared to changing FRP

geometry. The predictions for specimens that fail due to bond were almost identical for different concrete strengths, as bond strength was not affected by concrete strength. The predictions for specimens that fail due to crushing had more variation, higher compressive strength gave higher ultimate load capacity.

4.3.3 Effect of Shear Span

Varying shear span of the specimens for four-point bending testing did not change the moment-curvature profile for the upper bound, only the load at each moment, calculated with Equation (4-12), differed. Deflections associated with each load also changed, based on Equation (2-3). Were the specimens in this parametric study hollow, pure bending failure may have needed to be considered as opposed to combined bending and shear failure at longer shear spans, but since the concrete always controls deflection in these sections, failure modes other than concrete debonding and crushing were not considered. Four shear spans were considered for modelling, in terms of percentage of total span: 20% (base case), 33.3%, 50%, and 66.7%. A plot showing the effect of changing the four-point bending test shear span can be seen in Figure 4-7. Dark curves represent debonding failure, light curves represent crushing failure.

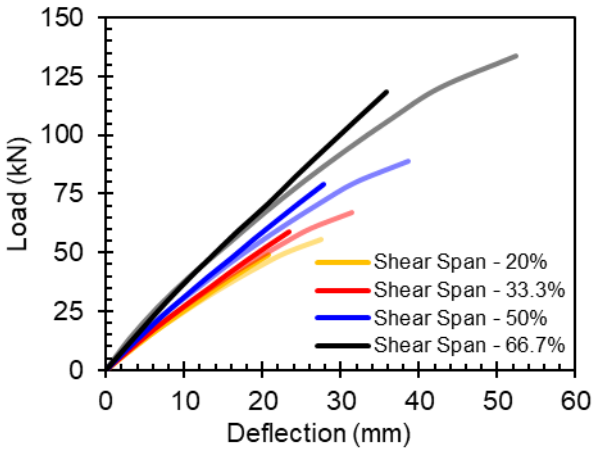

Figure 4-7 Variation of load-deflection plots based on changing shear span

As seen in Figure 4-7, increasing the shear span gave a slight increase in stiffness. The main difference between the varied shear spans and other parameters was the large increase peak deflection that corresponded to the increase in load capacity. Especially noticeable in the crushing failure specimens, it is unlikely that this large load and subsequent deflection would be reached before debonding occurred. At these loads, even with the increased shear span, it is probable that the concrete and FRP would fail simultaneously, like with the 1 m long bolted slab sections (SSB1-35-01 and SSB1-35-02)

4.3.4 Summary of Parametric Study

The parametric study showed the effects of changing three parameters on the load-deflection response of a 2 m long, epoxy and aggregate bonded slab specimen under four-point bending. The modelling methods were the same as those used to model the slab specimens in Section 4.2 with the addition of a Composite Percentage Factor so an actual load-deflection curve could be produced, rather than a range in which the curve would fall. The three varied parameters were: FRP geometry, concrete compressive strength, and shear

span. In regard to the criterion of increasing stiffness compared to the hollow specimens tested in the experimental program, changing the FRP geometry gave the most promising results. It was shown that increasing the height and width of the FRP sections (while proportionally changing the slab width) increased the stiffness of the specimens while also increasing ultimate load capacity and decreasing peak deflections for both cases of concrete failure observed during testing (debonding and crushing).

CHAPTER 5 CONCLUSION AND RECOMMENDATIONS

The purpose of the presented research was to understand the behaviour of commercially available GFRP square hollow structural sections under four-point bending and to assess the viability of a bridge decking system constructed from these sections. To achieve these goals an experimental program consisting of four main parts was carried out:

- Material testing to determine the properties of the FRP used in the research. Tensile, compressive, and shear properties were determined along with the fiber structure of the material.
- Preliminary testing of hollow sections. Hollow sections of three different lengths (1 m, 2 m, and 3 m) were tested under four-point bending.
- Preliminary testing of composite sections. A 2 m long specimen consisting of three hollow FRP beams adhered together and filled with concrete was tested under four-point bending. As well, multiple 1 m long specimens had different bonding mechanisms applied to their top faces and had a 35 mm concrete slab cast overtop.
- Main testing of composite sections. 18 specimens, 2 m long, consisting of a hollow FRP section with a concrete slab cast overtop were tested under four-point bending. Slab thickness of 35 mm, 55 mm and 75 mm were used with two different bonding methods: applying an epoxy paste and small aggregate to the top face of a specimen and applying bolts at 100 mm intervals along the top face of a specimen.

Two different models were used to help predict the experimental results. A linear-elastic model was used to compare with hollow specimens while a non-linear model was used to compare with slab specimens.

The following conclusions were gained from the experiment study and the analytical modelling:

- The hollow FRP sections were too flexible to be considered practical for use as bridge decking, concrete was needed to be used in composite with the FRP to increase stiffness.
- A built-up section filled with concrete slightly increased ultimate load capacity and stiffness when compared to the hollow sections, a violent failure mode was considered too great of a safety concern for further experimental testing.
- Of all bonding methods tested, using aggregate bonded to epoxy and drilling bolts into FRP specimens created the most effective bond, in terms of increasing stiffness.
- Full length specimens with epoxy and aggregate bond had reduced strength capacity when compared to hollow sections but had a stiffness gain between 62 and 78% depending on slab thickness.
- Full length specimens with bolted bond also had reduced strength compared to hollow sections, but like the epoxy and aggregate bonded specimens, stiffness was increased by between 54 and 79% depending on slab thickness.
- The bolted bond specimens had a tensile concrete failure that limited ultimate strength capacity more than the epoxy and aggregate specimens, which failed due to either concrete crushing or debonding from the FRP.
- Overall, epoxy and aggregate bonded specimens gave the most promising results in regard to creating a viable bridge decking system.
- The linear-elastic model used for hollow specimens generally predicted stiffness successfully, it also predicted ultimate load to within 24% of experimental test data

- The non-linear model used for slab specimens successfully predicted a range that the load-deflection curves fell into, the upper bound based on full composite action and the lower bound based on no composite action occurring.
- Results of a parametric study showed that increasing FRP height and width could increase stiffness and ultimate load capacity in epoxy and aggregate bonded slab sections.

In addition to the conclusions drawn from the experimental study and analytical modelling, the following recommendations are suggested to further expand on the research presented:

- Varying the shear span to length ratio to try to isolate pure bending and pure shear failure modes in hollow specimens should be considered.
- Tests should be conducted on epoxy and aggregate bonded specimens built up from multiple FRP beams with a large slab cast overtop.
- Tests should be conducted on individual epoxy and aggregate bonded specimens using hollow FRP sections with increased height and width compared the ones used in this study.
- The non-linear model should be refined to reflect partial composite action.
- The non-linear model should also be modified to more accurately predict ultimate load capacity.

BIBLIOGRAPHY

Acquah, C., Datskov, I., Mawardi, A., Zhang, F., Achenie, L. E. K., Pitchumani, R., and Santos, E. (2006). "Optimization under Uncertainty of a Composite Fabrication Process using a Deterministic One-Stage Approach." *Computers and Chemical Engineering*, 30(6–7), 947–960.

Alampalli, S., and Kunin, J. (2002). "Rehabilitation and Field Testing of an FRP Bridge Deck on a Truss Bridge." *Composite Structures*, 57, 373–375.

Andersons, J., and Korsgaard, J. (1999). "Residual Strength of GFRP at High-Cycle Fatigue." *Mechanics of Composite Materials*, 35(5), 395–402.

ASCE. (1985). *Structural Plastics Selection Manual*. *Structural Plastics Selection Manual*, American Society of Civil Engineers, New York, NY, USA.

ASCE. (2017). "2017 Infrastructure Report Card." *ASCE News*.

Ascione, L., Berardi, V. P., and D'Aponte, A. (2012). "Creep Phenomena in FRP Materials." *Mechanics Research Communications*, 43, 15–21.

Ascione, L., Berardi, V. P., Giordano, A., and Spadea, S. (2013). "Local Buckling Behavior of FRP Thin-Walled Beams: A Mechanical Model." *Composite Structures*, 98, 111–120.

Ascione, L., Caron, J.-F., Godonou, P., van IJselmuijden, K., Knippers, J., Mottram, T., Oppe, M., Sorensen, M. G., Taby, J., and Tromp, L. (2016). *Prospect for New Guidance in the Design of FRP*. (L. Acsione, E. Gutierrez, S. Dimova, A. Pinto, and S. Denton, eds.), European Commission Joint Research Centre.

ASTM. (2011). *D2344/D2344M - 16 - Standard Test Method for Short-Beam Strength of Polymer Matrix Composite Materials*. West Conshohocken, PA, USA.

ASTM. (2016). *D3410/D3410M - 16 - Standard Test Method for Compressive Properties of Polymer Matrix Composite Materials with Unsupported Gage Section by Shear*. West Conshohocken, PA, USA.

ASTM. (2017). *D3039/D3039M - 17 - Standard Test Method for Tensile Properties of Polymer Matrix Composite Materials*. West Conshohocken, PA, USA.

ASTM. (2018). *D2584 - 18 - Standard Test Method for Ignition Loss of Cured Reinforced Resins*. West Conshohocken, PA, USA.

Bakis, C. E., Bank, L. C., Brown, V. L., Cosenza, E., Davalos, J. F., Lesko, J. J., Machida, A., Rizkalla, S. H., and Triantafillou, T. C. (2002). "Fiber-Reinforced Polymer Composites for Construction - State-of-the-Art Review." *Journal of Composites for Construction*, 6(2), 73–87.

Bank, L. C. (1989). "Flexural and Shear Moduli of Full-Section Fiber Reinforced Plastic (FRP) Pultruded Beams." *Journal of Testing and Evaluation*, 17, 40–45.

Bank, L. C. (2006a). *Composites for Construction: Structural Design with FRP Materials*. *Composites for Construction: Structural Design with FRP Materials*, John Wiley & Sons Inc., New York, NY, USA.

Bank, L. C. (2006b). "Application of FRP Composites to Bridges in the USA." Japan Society of Civil Engineers, Tokyo, 9–16.

Benmokrane, B., Newhook, J., and Svecova, D. (2007). *Reinforcing Concrete Structures with Fiber Reinforced Polymers*. (A. A. Mufti and S. Rizkalla, eds.), ISIS Canada Corporation, Winnipeg, MB, Canada.

Boles, R., Nelson, M., and Fam, A. (2015). "Durability of Bridge Deck with FRP Stay-in-Place Structural Forms under Freeze-thaw Cycles." *Journal of Composites for Construction*, 19(4).

Borowicz, D. T., and Bank, L. C. (2011). "Behavior of Pultruded Fiber-Reinforced Polymer Beams Subjected to Concentrated Loads in the Plane of the Web." *Journal of Composites for Construction*, 15(2), 229–238.

Chen, A., and Davalos, J. F. (2014). "Design Equations and Example for FRP Deck-Steel Girder Bridge System." *Practice Periodical on Structural Design and Construction*, 19(2).

Cheng, L., and Karbhari, V. M. (2006). “Fatigue Behavior of a Steel-Free FRP-Concrete Modular Bridge Deck System.” *Journal of Bridge Engineering*, 11(4), 474–488.

CIRC. (2019). *Canada Infrastructure Report Card 2019*.

Composite Advantage. (2008). *FRP Bridges and Decks - A White Paper On The Long Term Savings With Immediate Benefits*. Dayton, Ohio, USA.

Cowper, G. R. (1966). “The Shear Coefficient in Timoshenko’s Beam Theory.” *Journal of Applied Mechanics*, 33(2), 335–340.

CSA Group. (2014). *A23.3-14 Design of Concrete Structures*. CSA Group, Toronto, ON, Canada.

CSA Group. (2019). *S6-19 Canadian Highway Bridge Design Code*. CSA Group, Toronto, ON, Canada.

Daniel, I. M., and Ishai, O. (2006). *Engineering Mechanics of Composite Materials*. Oxford University Press, New York, NY, USA.

Das, B., Sahu, S. K., and Ray, B. C. (2007). “Effects of Loading Speed on the Failure Behaviour of FRP Composites.” *Aircraft Engineering and Aerospace Technology*, 79(1), 45–52.

Davalos, J. F., Salim, H. A., Qiao, P., Lopez-Anido, R., and Barbero, E. J. (1996). “Analysis and Design of Pultruded FRP Shapes under Bending.” *Composites Part B*, 27, 295–305.

Dieter, D. (2002). “Experimental and Analytical Study of Concrete Bridge Decks Constructed with FRP Stay-in-Place Forms and FRP Grid Reinforcing.” University of Wisconsin - Madison.

Ehlen, M. A. (1999). “Life-Cycle Costs of Fiber-Reinforced Polymer Bridge Decks.” *Journal of Materials in Civil Engineering*, 11(3), 224–230.

Fiberline. (2017). “Values for Global Analyses, FBD600.” Fiberline, Middelfart, Denmark.

Gai, X., Darby, A., Ibell, T., and Evernden, M. (2013). “Experimental Investigation into a Ductile FRP Stay-in-Place Formwork System for Concrete Slabs.” *Construction and Building Materials*, 49, 1013–1023.

Gong, J., Zou, X., and Xia, P. (2019). “Experimental Investigation of the Natural Bonding Strength between Stay-In-Place Form and Concrete in FRP-Concrete Decks/Beams.” *Applied Sciences (Switzerland)*, 9.

Goyal, R., Mukherjee, A., and Goyal, S. (2016). “An Investigation on Bond between FRP Stay-in-Place Formwork and Concrete.” *Construction and Building Materials*, 113, 741–751.

Gunson, B., and Murphy, B. (2019). *Enhancing Ontario’s Rural Infrastructure Preparedness: Inter-Community Service Sharing in a Changing Climate*. Brantford, ON, Canada.

Hanus, J. P., Bank, L. C., and Oliva, M. G. (2009). “Combined Loading of a Bridge Deck Reinforced with a Structural FRP Stay-in-Place Form.” *Journal of Construction and Building Materials*, 23, 1605–1619.

Hayes, M. D., Ohanehi, D., Lesko, J. J., Cousins, T. E., and Witcher, D. (2000). “Performance of Tube and Plate Fiberglass Composite Bridge Decck.” *Journal of Composites for Construction*, 4(2), 48–55.

Honickman, H. N. (2008). “Pultruded GFRP Sections as Stay-in-Place Structural Open Formwork for Concrete Slabs and Girders.” Queen’s University.

Honickman, H., Nelson, M., and Fam, A. (2009). “Investigation into the Bond of Glass Fiber-Reinforced Polymer Stay-in-Place Structural Forms to Concrete for Decking Applications.” *Transportation Research Record*, 134–144.

Huo, R., Liu, W., Wan, L., Fang, Y., and Wang, L. (2015). “Experimental Study on Sandwich Bridge Decks with GFRP Face Sheets and a Foam-Web Core Loaded under Two-Way Bending.” *Advances in Materials Science and Engineering*.

Jiang, X., Kolstein, M. H., and Bijlaard, F. S. K. (2013). "Experimental and Numerical Study on Mechanical Behavior of an Adhesively-Bonded Joint of FRP-Steel Composite Bridge Under Shear Loading." *Composite Structures*, 108, 387–399.

Keller, T. (2002). "Overview of Fibre-Reinforced Polymers in Bridge Construction." *Structural Engineering International*, 2, 66–70.

Keller, T., Ph, D., Rothe, J., Castro, J. De, Ph, D., Osei-antwi, M., and Asce, S. M. (2014). "GFRP-Balsa Sandwich Bridge Deck: Concept, Design, and Experimental Validation." *Journal of Composites for Construction*, 18(2).

Kumar, P., Chandrashekhara, K., and Nanni, A. (2003). "Structural Performance of a FRP Bridge Deck." *Construction and Building Materials*, 18, 35–47.

Lau, D., Qiu, Q., Zhou, A., and Chow, C. L. (2016). "Long term performance and fire safety aspect of FRP composites used in building structures." *Construction and Building Materials*, 126, 573–585.

Liu, Z., and Cousins, T. E. (2007). "Testing and Analysis of a Fiber-Reinforced Polymer (FRP) Bridge Deck." Virginia Polytechnic Institute and State Univeristy.

Loff, A. (2015). "Rock's Village Bridge." *FRP International*, 3–5.

Lopez-Anido, R., and Xu, H. (2002). "Structural Characterization of Hybrid Fiber-Reinforced Polymer-Glulam Panels for Bridge Decks." *Journal of Composites for Construction*, 6(3), 194–203.

Lounis, Z. (2007). "Aging Highway Bridges." *Canadian Consulting Engineer*, Toronto, (48), 30–34.

Manalo, A., Aravinthan, T., Fam, A., and Benmokrane, B. (2017). "State-of-the-Art Review on FRP Sandwich Systems for Lightweight Civil Infrastructure." *Journal of Composites for Construction*, 21(1).

Mara, V., Haghani, R., and Harryson, P. (2013). "Bridge Decks of Fibre Reinforced Polymer (FRP): A Sustainable Solution." *Construction and Building Materials*, 50, 190–199.

Minghini, F., Tullini, N., and Laudiero, F. (2014). "Identification of the Short-Term Full-Section Moduli of Pultruded FRP Profiles Using Bending Tests." *Journal of Composites for Construction*, 18(1).

Mottram, J. T. (2004). "Shear Modulus of Standard Pultruded Fiber Reinforced Plastic Material." *Journal of Composites for Construction*, 8(2), 141–147.

Muttashar, M., Karunasena, W., Manalo, A., and Lokuge, W. (2016). "Behaviour of Hollow Pultruded GFRP Square Beams with Different Shear Span-to-Depth Ratios." *Journal of Composite Materials*, 50(21), 2925–2940.

Nelson, M., and Fam, A. (2014). "Modeling of Flexural Behavior and Punching Shear of Concrete Bridge Decks with FRP Stay-in-Place Forms Using the Theory of Plates." *ASCE Journal of Engineering Mechanics*, 140(12).

Nelson, M., Fam, A., Busel, J. P., Bakis, C. E., Nanni, A., Bank, L. C., Henderson, M., and Hanus, J. (2014). "FRP Stay-in-Place Structural Forms for Concrete Bridge Decks: A State-of-the- Art Review." *ACI Structural Journal*, (September).

Nelson, M. S. (2013). "Experimental and Analytical Investigations of Concrete Bridge Decks with Structural FRP Stay-In-Place Forms." Queen's University.

Nguyen, T. T., Chan, T. M., and Mottram, J. T. (2018). "Reliable In-Plane Shear Modulus for Pultruded-Fibre-Reinforced Polymer Sections." *Structures and Buildings*, 171(11), 818–829.

Nicoletta, B., Smith, M., and Gales, J. (2018). *Toward Fire Resilience in Canadian Bridge Infrastructure*. Toronto, ON, Canada.

Noël, M., and Fam, A. (2016). "Design Equations for Concrete Bridge Decks with FRP Stay-in-Place Structural Forms." *Journal of Composites for Construction*, 20(5).

Oliva, M., Bank, L., Bae, H.-U., Barker, J., and Yoo, S.-W. (2007). "FRP Stay-in-Place Formwork and Reinforcing for Concrete Highway Bridge Decks." *FRPRCS-8*, Patras, Greece.

Omidvar, B. (1998). “Shear Coefficient in Orthotrpoic Thin-Walled Composite Beams.” *Journal of Composites for Construction*, 2(1), 46–56.

Qi, Y., Fang, H., Shi, H., Liu, W., Qi, Y., and Bai, Y. (2017). “Bending Performance of GFRP-Wood Sandwich Beams with Lattice-Web Reinforcement in Flatwise and Sidewise Directions.” *Construction and Building Materials*, 156, 532–545.

Qiao, P., Davalos, J. F., and Barbero, E. J. (1998). “Design Optimization of Fiber Reinforced Plastic Composite Shapes.” *Journal of Composite Materials*, 32(2), 177–196.

Qiao, P., Davalos, J. F., and Brown, B. (2000). “A Systematic Analysis and Design Approach for Single-Span FRP Deck/Stringer Bridges.” *Composites Part B: Engineering*, 31, 593–609.

Rajak, D. K., Pagar, D. D., Kumar, R., and Pruncu, C. I. (2019). “Recent Progress of Reinforcement Materials: A Comprehensive Overview of Composite Materials.” *Journal of Materials Research and Technology*, 8(6), 6354–6374.

Roberts, T. M., and Al-Ubaidi, H. (2002). “Flexural and Torsional Properties of Pultruded Fiber Reinforced Plastic I-Profiles.” *Journal of Composites for Construction*, 6(1), 28–34.

Sadeghian, P., and Fam, A. (2010). “Bond-Slip Analytical Formulation toward Optimal Embedment of Concrete-Filled Circular FRP Tubes into Concrete Footings.” *Journal of Engineering Mechanics*, 136(4), 524–533.

Sadeghian, P., Hristozov, D., and Wroblewski, L. (2018). “Experimental and Analytical Behavior of Sandwich Composite Beams: Comparison of Natural and Synthetic Materials.” *Journal of Sandwich Structures and Materials*, 20(3), 287–307.

Salim, H. A., Davalos, J. F., Qiao, P., and Kiger, S. A. (1997). “Analysis and Design of Fiber Reinforced Plastic Composite Deck-and-Stringer Bridges.” *Composite Structures*, 38, 295–307.

Satasivam, S., Bai, Y., Yang, Y., Zhu, L., and Zhao, X. (2017). “Mechanical Performance of Two-Way Modular FRP Sandwich Slabs.” *Composite Structures*, 184, 904–916.

Schwab, K. (2019). *The Global Competitiveness Report*. World Economic Forum, Geneva, Switzerland.

Siwowski, T., Kaleta, D., and Rajchel, M. (2018a). "Structural Behaviour of an All-Composite Road Bridge." *Composite Structures*, 192, 555–567.

Siwowski, T., Rajchel, M., Sienko, R., and Bednarski, L. (2018b). "Smart Monitoring of the FRP Composite Bridge with Distributed Fibre Optic Sensors." *9th International Conference on Fibre-Reinforced Polymer (FRP) Composites in Civil Engineering*, Paris, France, 918–925.

Volz, J. S., Khayat, K. H., Hwang, S. D., Tuwair, H., Drury, J. T., and Crone, A. S. (2017). *Field Implementation of Fiber - Reinforced Polymer (FRP) Deck Panels*. Norman, OK, USA.

Wardeh, G., Mohamed, M. A. S., and Ghorbel, E. (2010). "Analysis of Concrete Internal Deterioration due to Frost Action." *Journal of Building Physics*, 35(1), 54–82.

Williams, B., Shehata, E., Church, K., Stewart, D., and Rizkalla, S. (2001). *GFRP Modular Bridge Decks*.

Wu, Z., Wang, X., Zhao, X., and Noori, M. (2014). "State-of-the-Art Review of FRP Composites for Major Construction with High performance and Longevity." *International Journal of Sustainable Materials and Structural Systems*, 1(3), 201.

Yanes-Armas, S., de Castro, J., and Keller, T. (2015). "System Transverse In-Plane Shear Stiffness of Pultruded GFRP Bridge Decks." *Engineering Structures*, 107, 34–46.

Yanes-Armas, S., de Castro, J., and Keller, T. (2016). "Energy Dissipation and Recovery in Web-Flange Junctions of Pultruded GFRP decks." *Composite Structures*, 148, 168–180.

Yuan, J. S., and Hadi, M. N. S. (2018). "Friction Coefficient between FRP Pultruded Profiles and Concrete." *Materials and Structures*, 51.

Zhou, A., Coleman, J. T., Temeles, A. B., Lesko, J. J., and Cousins, T. E. (2005). "Laboratory and Field Performance of Cellular Fiber-Reinforced Polymer Composite Bridge Deck Systems." *ASCE Journal of Composites for Construction*, 9, 458–467.